

Anisotropic Permeability Tensor Prediction from Porous Media Microstructure via Physics-Informed Progressive Transfer Learning with Hybrid CNN-Transformer

Mohammad Nooraiepour^{1,*}

¹Faculty of Mathematics and Natural Sciences, University of Oslo, PO Box 1047 Blindern, 0316 Oslo, Norway

*Corresponding author: monoo@uio.no

Abstract

Accurate prediction of permeability tensors from pore-scale microstructure images is essential for subsurface flow modeling, yet direct numerical simulation requires hours per sample—fundamentally limiting large-scale uncertainty quantification and reservoir optimization workflows. A physics-informed deep learning framework is presented that resolves this bottleneck by combining a MaxViT hybrid CNN-Transformer architecture with progressive transfer learning and differentiable physical constraints. MaxViT’s multi-axis attention mechanism simultaneously resolves grain-scale pore-throat geometry through block-local operations and REV-scale connectivity statistics through grid-global operations, providing the spatial hierarchy that permeability tensor prediction physically requires. Training on 20,000 synthetic porous media samples spanning three orders of magnitude in permeability, a three-phase progressive curriculum advances from an ImageNet-pretrained baseline with D4-equivariant augmentation and tensor transformation, through component-weighted loss prioritizing off-diagonal coupling, to frozen-backbone transfer learning with porosity conditioning via Feature-wise Linear Modulation (FiLM). Onsager reciprocity and positive-definiteness are enforced through differentiable penalty terms, achieving mean symmetry error $\varepsilon_{\text{sym}} = 3.95 \times 10^{-7}$ and 100% thermodynamic validity without post-hoc correction. On a held-out test set of 4,000 samples, the framework achieves variance-weighted $R^2 = 0.9960$ ($R_{K_{xx}}^2 = 0.9967$, $R_{K_{xy}}^2 = 0.9758$), a 33% reduction in unexplained variance over the supervised baseline, with every reported metric improving monotonically across all three phases. Inference requires 120 ms per sample—a significant speedup over lattice-Boltzmann simulation that enables real-time permeability characterization during core scanning, Monte Carlo uncertainty quantification on a single GPU, and rapid multi-scenario screening for CO₂ storage and geo-energy applications. The results establish three transferable principles for physics-informed scientific machine learning: large-scale visual pretraining transfers effectively across domain boundaries; physical constraints are most robustly integrated as differentiable architectural components; and progressive training guided by diagnostic failure-mode analysis enables unambiguous attribution of performance gains across methodological stages.

Keywords: Permeability tensor prediction; Porous media; Physics-informed machine learning; Hybrid CNN-Transformer; Progressive transfer learning; Anisotropy; Uncertainty quantification; Subsurface flow characterization.

1 Introduction

Fluid flow through porous geological formations governs a broad range of processes of direct societal and engineering importance, including the management of geo-energy resources, groundwater systems, geological CO₂ and H₂ storage, and subsurface contaminant transport [1–7].

Accurate characterization of porous media transport properties is a prerequisite for reservoir management decisions, operational performance and risk assessment for geological storage sites, aquifer remediation strategies, and large-scale probabilistic uncertainty quantification workflows that require millions of forward evaluations. At the pore scale, fluid motion is governed by the Navier-Stokes equations. The permeability tensor \mathbf{K} emerges as the fundamental macroscopic transport property relating the pressure gradient to the Darcy velocity through Darcy’s law:

$$\mathbf{q} = -\frac{\mathbf{K}}{\mu}\nabla p, \quad (1)$$

where \mathbf{q} is the Darcy velocity vector, μ is dynamic viscosity, and ∇p is the pressure gradient. For two-dimensional porous media, \mathbf{K} is a 2×2 symmetric positive-definite matrix encoding directional flow preferences and geometric tortuosity. Computing \mathbf{K} from pore-scale images through direct numerical simulation (DNS) of the Stokes equations, employing methods such as lattice-Boltzmann, finite-volume, or finite-element schemes [8–11], yields highly accurate results but incurs computational costs of hours to days per sample even on high-performance hardware [12, 13]. This expense severely constrains applications requiring thousands to millions of permeability evaluations.

Recent advances in deep learning have demonstrated that neural networks trained on sufficiently large labeled datasets derived from pore-scale images can predict permeability tensors with exceptional accuracy while reducing inference time from hours to milliseconds [14–17]. Early investigations established that convolutional neural networks (CNNs) can learn effective representations of pore geometry directly from image data, enabling rapid permeability prediction [18–21]. Subsequent contributions advanced these techniques through multi-scale architectures and expanded applicability to diverse pore morphologies, [22–25]. More recently, physics-informed neural networks have been investigated to enforce adherence to underlying physical principles within the model [25–29], and graph neural networks have been applied to capture the topological features and connectivity of pore networks [30–32]. These developments underscore the growing potential of integrating domain knowledge into data-driven neural architectures [33–35]. The architectural foundation of the present work, a hybrid CNN-Transformer design (MaxViT, detailed in Section 2.2), is motivated by these advances and their demonstrated capacity for learning hierarchical spatial features from binary porous media images while respecting the multi-scale nature of permeability-geometry relationships.

While deep learning has emerged as the predominant approach for image-based permeability prediction, the broader machine learning landscape offers established regression paradigms that merit explicit consideration as alternatives. Gaussian process regression (GPR) provides principled Bayesian uncertainty quantification through kernel-based modeling of function smoothness [36–38]. Ensemble methods such as random forests and gradient boosting [39–42] aggregate predictions from multiple weak learners for robustness against noise. Support vector regression employs kernel methods to handle nonlinear relationships in moderate-dimensional feature spaces [43–45], and regression trees offer transparent hierarchical partitioning [41, 46]. However, these methods face fundamental challenges at the scale of high-resolution porous media images. The input dimensionality of $128 \times 128 = 16,384$ pixels creates a severe curse of dimensionality for methods operating on flattened feature vectors: GPR scales cubically with the number of training samples and requires explicit kernel design in this high-dimensional space; support vector regression similarly demands careful kernel selection in the same regime; and tree-based methods struggle to capture smooth spatial structure without extreme depth. More fundamentally, these approaches typically require hand-crafted feature engineering to reduce dimensionality, extracting quantities such as porosity, pore-size distributions, tortuosity, or correlation functions, which demands domain expertise, introduces information bottlenecks, and may discard spatial patterns not anticipated by the feature designer. Permeability depends nonlinearly on multi-scale spatial structure, from grain-scale pore-throat geometry to domain-scale connectivity, relationships that are difficult to capture through linear combinations of scalar features or axis-aligned decision

boundaries. Deep convolutional architectures address these limitations through hierarchical spatial feature learning [47–49]: convolutional layers with local receptive fields and weight sharing encode translation equivariance and spatial smoothness priors appropriate to image data; pooling operations implement multi-scale aggregation without explicit feature engineering; and end-to-end differentiable training enables direct optimization of the full input-to-output mapping. For the present task, predicting a 2×2 permeability tensor from binary microstructure images spanning three orders of magnitude in permeability, empirical studies demonstrate that deep CNNs consistently achieve strong benchmark performance [19, 22, 24], while comparable results with non-deep methods would require extensive manual feature extraction and domain-specific kernel design.

Despite these successes, existing deep learning approaches for permeability prediction face several persistent limitations. The first concerns architecture. Methods based on pure CNNs excel at capturing local geometric features and fine-grained interface details through translation equivariance and local connectivity, but struggle with long-range spatial dependencies critical for understanding global pore connectivity and anisotropic coupling [50–53]. Conversely, pure Vision Transformers (ViTs) capture global context through self-attention but incur quadratic computational complexity with image size and lack the inductive biases that make CNNs effective for structured spatial data [54–57]. This architectural tension is especially consequential for off-diagonal permeability components K_{xy} and K_{yx} , which encode geometric anisotropy arising from pore channels oriented obliquely to the principal coordinate axes. Accurate prediction of these components requires simultaneously resolving fine-scale pore-throat geometry at length scales of individual grains (roughly 10–100 pixels), governing local flow resistance, and long-range spatial correlations spanning the full image domain, determining how preferential flow paths align and couple across directions. The characteristic spatial correlation length governing off-diagonal coupling is typically comparable to the representative elementary volume (REV) size, which for sandstone microstructures can span the entire image domain. Pure CNNs cannot integrate information over these scales without very deep architectures that sacrifice fine-scale resolution, while pure ViTs lack the inductive biases to resolve sharp solid-fluid interfaces efficiently.

The second persistent limitation concerns physical validity. Permeability tensors must satisfy fundamental physical requirements: symmetry ($K_{xy} = K_{yx}$) arising from Onsager reciprocity, and positive-definiteness ensuring thermodynamic consistency. Most existing approaches enforce these constraints only weakly through data characteristics or post-hoc projection, rather than incorporating them directly into the training objective. Furthermore, isotropic porous media exhibit natural geometric symmetries under rotations and reflections. Existing augmentation strategies either ignore these symmetries entirely or apply image transformations without corresponding tensor transformations, creating training inconsistencies that degrade model performance and introduce physical violations. It should be noted that enforcing symmetry through data augmentation, as opposed to building equivariance into the network architecture, yields approximate equivariance that is not guaranteed to hold exactly at inference time; the implications of this distinction are discussed in Section 2. The challenge of predicting off-diagonal tensor components remains particularly acute, with reported accuracy often substantially lower than for diagonal components, as these elements encode subtle geometric anisotropies requiring global spatial integration.

Hybrid CNN-Transformer architectures have emerged as a promising direction for simultaneously leveraging local and global feature extraction [58–63]. Among these, MaxViT [64] introduces a multi-axis self-attention mechanism that decomposes standard two-dimensional self-attention into sequential block-local and grid-global operations. This decomposition reduces computational complexity from $\mathcal{O}(H^2W^2)$ to $\mathcal{O}(HW)$ while preserving a global receptive field, a critical property for high-resolution scientific imaging. From a physical standpoint, block-local attention resolves grain-scale pore-throat geometry at length scales relevant to local flow resistance, while grid-global attention integrates information across the full image domain for

off-diagonal coupling. This architectural decomposition directly mirrors the two-scale nature of the permeability prediction problem: local geometry determines individual flow path conductances, while global topology determines how those conductances combine anisotropically into the full tensor. MaxViT has achieved state-of-the-art results across diverse computer vision benchmarks [64–66] and demonstrates particular strength in transfer learning scenarios with limited labeled data, precisely the condition encountered in scientific imaging applications where ground-truth labels require computationally expensive physics-based simulation. Despite these advantages, MaxViT has not been previously applied to physics-informed prediction tasks or porous media characterization.

Prior to adopting supervised transfer learning, a systematic investigation of self-supervised pretraining strategies for binary porous media images was conducted, focusing on Masked Autoencoder (MAE) approaches [67–69]. Contrastive methods such as SimCLR and MoCo were also considered but their reliance on semantic augmentation invariances, including color jitter and crop-based views, cannot be motivated for binary images with no color information and where cropping may discard the globally connected pore structure that constitutes the primary signal of interest. The MAE experiments revealed fundamental incompatibilities between MAE’s design assumptions and the characteristics of binary porous media. MAE relies on smooth pixel gradients, high spatial redundancy, and continuous-valued image statistics, properties abundant in natural images but absent in binary porous media characterized by sharp discontinuities at solid-fluid interfaces, low geometric redundancy, and discrete pixel values. Despite extensive architectural exploration spanning masking ratios (25–75%), decoder depths (1–8 layers), and reconstruction targets (binary versus distance transform), all MAE configurations failed to achieve usable reconstruction quality (best PSNR: 14.4 dB versus a required threshold of >20 dB for meaningful feature learning, established by evaluating fine-tuned regression head performance at varying PSNR levels against a randomly initialized baseline). This negative result provides an important insight: effective representation learning for binary porous media requires supervision from physically meaningful labels rather than pixel-level reconstruction objectives. Consequently, the framework developed here focuses on supervised transfer learning from ImageNet-pretrained features, which provide robust low- and mid-level visual representations that transfer effectively despite the domain difference. This negative result for self-supervised pretraining also directly motivated the progressive transfer learning strategy detailed in Section 2.3, which leverages ImageNet-pretrained features as a robust initialization and systematically refines them through three phases of task-specific adaptation.

The framework proposed in this work addresses the limitations identified above through a systematic combination of architectural selection, physics-informed training objectives, rigorous geometric augmentation, and progressive transfer learning. The MaxViT hybrid architecture is applied for the first time to permeability tensor prediction, with its multi-axis self-attention mechanism providing the spatial hierarchy needed for simultaneous fine-scale pore-throat resolution and global connectivity integration. A physics-aware loss function is developed that explicitly enforces tensor symmetry and positive-definiteness through differentiable penalty terms, eliminating the need for post-hoc projection. A D4-equivariant augmentation strategy is implemented that consistently transforms both microstructure images and their associated permeability tensors through proper tensor transformation matrices, removing the training inconsistencies present in naive augmentation approaches. While this augmentation-based approach achieves strong empirical equivariance, it is acknowledged that it does not provide architectural guarantees of exact equivariance at inference time, in contrast to group equivariant networks [70–72]; this distinction is discussed in Section 2. A three-phase progressive training strategy is proposed: Phase 2 establishes a supervised baseline with ImageNet-pretrained MaxViT, progressive unfreezing, and D4-equivariant augmentation; Phase 3 extends this through calibrated morphological and elastic deformations with enhanced loss weighting that prioritizes off-diagonal tensor elements; Phase 4 freezes the learned backbone while introducing porosity-conditioned Feature-wise

Linear Modulation (FiLM) [73], combined with ensemble techniques including Stochastic Weight Averaging [74] and Exponential Moving Average [75]. The resulting framework attains an R^2 of 0.9960 on a diverse dataset of 20,000 porous media samples spanning three orders of magnitude in permeability, along with a significant reduction in prediction error relative to the supervised baseline, while reducing computational cost from hours per sample (DNS) to approximately 120 ms per prediction (inference).

The main contributions of this work are:

1. Physics-motivated hybrid architecture. Systematic application of the MaxViT hybrid CNN-Transformer to permeability tensor prediction is presented, with an explicit physical justification connecting block-local attention to pore-throat geometry resolution and grid-global attention to the long-range connectivity integration governing off-diagonal tensor coupling.
2. Differentiable physics-informed loss. A loss function is developed that enforces tensor symmetry and positive-definiteness through differentiable penalty terms, yielding near-machine-precision symmetry and 100% thermodynamic validity without post-processing.
3. D4-equivariant augmentation with rigorous tensor transformation. An augmentation strategy is introduced that consistently transforms microstructure images and their associated permeability tensors under the D4 symmetry group, eliminating training inconsistencies that arise when image and label transformations are mismatched.
4. Progressive three-phase transfer learning. A structured training curriculum to transition from frozen ImageNet features to full fine-tuning and finally to porosity-conditioned FiLM adaptation, with each phase providing physically interpretable performance gains.
5. Computational efficiency. The framework reduces permeability tensor inference time from hours (DNS) to approximately 120 ms, enabling practical deployment in workflows requiring large-scale ensemble evaluations for uncertainty quantification and reservoir characterization.

The remainder of this paper is organized as follows. Section 2 describes the dataset generation and statistical characteristics, the MaxViT hybrid CNN-Transformer architecture and its adaptation for permeability tensor prediction, the physics-aware loss formulation incorporating symmetry and positive-definiteness constraints, the D4-equivariant data augmentation strategy with rigorous tensor transformation, and the three-phase progressive training curriculum. Section 3 presents experimental results across all training phases, component-wise prediction accuracy analysis, physical constraint validation, comparative evaluation against baseline methods, and detailed discussion of failure modes and limitations. Section 4 summarizes the key findings, contributions to physics-informed machine learning for porous media characterization, and implications for computational subsurface flow modeling.

2 Materials and Methods

2.1 Dataset and Problem Formulation

2.1.1 Porous Media Image Dataset

The dataset comprises 24,000 binary porous media images generated via sequential Gaussian simulation, designed to replicate realistic sandstone pore geometries by Vargdal et al. [76, 77]. Each image is a strictly binary 128×128 pixel array in which values of 1 represent solid grain and values of 0 represent pore space, with porosity defined as $\phi = 1 - \text{mean}(I)$. Porosity spans $\phi \in [0.227, 0.900]$ with mean $\bar{\phi} = 0.711 \pm 0.124$ across all splits; the distribution is moderately left-skewed (skewness ≈ -0.55) and significantly non-normal (Shapiro-Wilk $p \approx 0$), reflecting the post-processing described below. Full descriptive statistics are provided in Table 3 (Appendix A).

According to [76], raw-generated images may contain isolated fluid clusters that are completely enclosed by solid matrix and therefore disconnected from the main flow network. Because these regions contribute neither to flow nor to permeability, an established post-processing step identified and removed them through connectivity analysis under periodic boundary conditions. The resulting filled images represent the connected-pore-network porosity, eliminated stagnant-region nodes from subsequent flow simulations, and formed the basis for all permeability computations and model training reported here [76, 77]. This filling procedure, while physically motivated, may shift the effective porosity distribution toward well-connected porous media, placing the dataset mean substantially above the typical range for natural sandstone reservoirs. Predictions for tight or poorly connected samples therefore reside near the lower tail of the training distribution and are expected to carry higher relative uncertainty; the corresponding failure-mode analysis is provided in Appendix H.4.

The full 2×2 permeability tensor for each image was computed via lattice-Boltzmann (LBM) simulation of single-phase Stokes flow at low Reynolds number [76]. Body forces applied in orthogonal directions and volume-averaged fluid velocities yield the permeability tensor through Darcy’s law, expressed in lattice units of order unity. Diagonal permeabilities span three orders of magnitude in \log_{10} -space; off-diagonal components are centered near zero and exhibit heavy tails (kurtosis ≈ 9 –13), reflecting the predominantly isotropic character of the media. All ground-truth tensors are 100% positive-definite, and tensor symmetry is preserved to $\varepsilon_{\text{sym}} < 8 \times 10^{-6}$ by the LBM solver. Complete LBM implementation and validation are documented in [76, 77].

Prior to model development, a comprehensive dataset characterization study was conducted covering microstructure geometry, permeability tensor statistics, porosity-permeability relationships, cross-split distributional consistency, anisotropy analysis, and outlier identification. Kolmogorov-Smirnov tests and Jensen-Shannon divergence measurements confirmed that training, validation, and test splits are drawn from statistically indistinguishable distributions across all variables, validating the random partitioning protocol. These analyses are reported in full in Appendix A.

2.1.2 Problem Formulation

Permeability prediction is formulated as a supervised regression task,

$$f_{\theta} : \mathbb{R}^{128 \times 128} \rightarrow \mathbb{R}^{2 \times 2}, \quad (2)$$

where f_{θ} denotes a neural network with parameters θ mapping binary porous media images to symmetric positive-definite permeability tensors:

$$\mathbf{K} = \begin{bmatrix} K_{xx} & K_{xy} \\ K_{xy} & K_{yy} \end{bmatrix}, \quad K_{xx}, K_{yy} > 0. \quad (3)$$

The network produces a four-element output $[K_{xx}, K_{xy}, K_{yx}, K_{yy}]$, reshaped to a 2×2 matrix at evaluation time. Two physical constraints must be satisfied:

$$K_{xy} = K_{yx} \quad (\text{tensor symmetry}), \quad (4)$$

$$K_{xx}, K_{yy} > 0 \quad (\text{positive diagonal}). \quad (5)$$

These constraints are incorporated through the physics-aware loss function (Section 2.4) and verified post hoc on the held-out test set. The positivity penalty in the loss function enforces positive diagonal elements in the predicted permeability tensor, while full positive-definiteness—although not enforced by construction—is consistently verified empirically across all samples in the held-out test set (Section 2.6.2). The high input dimensionality ($128 \times 128 = 16,384$ pixels) and strongly nonlinear, multi-scale structure-property relationships motivate end-to-end differentiable architectures that learn spatial hierarchies directly from raw images, in preference to methods requiring hand-crafted dimensionality reduction prior to regression.

2.1.3 Data Partitioning and Evaluation Protocol

Of the 24,000 total images, 20,000 carry computed permeability labels and are partitioned by random sampling into a training set (16,000 samples, 80%) and a validation set (4,000 samples, 20%). An independently generated set of 4,000 labeled samples from the same distribution constitutes the held-out test set, never accessed during model development, hyperparameter selection, or training decisions. The remaining 4,000 unlabeled images, initially reserved for self-supervised pretraining, were found to confer no benefit for binary porous media (see Introduction) and are excluded from all reported results.

Strict separation between all three splits is maintained throughout. The validation set is used exclusively for model checkpointing and early stopping based on validation R^2 . Augmentation parameters and loss-function weights were determined through preliminary grid searches on the validation set, conducted independently of the final training runs, to preclude implicit test-set leakage. Reported test-set results therefore constitute unbiased estimates of generalization to unseen porous media samples.

2.2 Model Architecture

2.2.1 MaxViT Backbone

The backbone is a Multi-Axis Vision Transformer (MaxViT-Base) [64], a hierarchical hybrid architecture combining depthwise-separable convolutions for local feature extraction with multi-axis self-attention for global context modeling. The implementation follows the `timm` library [78, 79], using weights pretrained on ImageNet-21K and subsequently fine-tuned on ImageNet-1K, providing robust low- and mid-level visual features that transfer effectively across the domain gap to porous media images.

Two adaptations are applied to accommodate the target domain. First, the input is re-configured to single-channel grayscale (`in_chans=1`), modifying the first convolutional layer’s input channels while preserving pretrained spatial filters via channel averaging. Second, the input resolution is specified as 128×128 (`img_size=128`), triggering automatic interpolation of positional embeddings and spatial-dimension adjustment across all hierarchical stages.

The backbone comprises four stages with progressively increasing channel dimensionality and decreasing spatial resolution. Each stage contains multiple MaxViT blocks, each integrating an MBConv module (depthwise-separable convolution with squeeze-and-excitation) followed by two multi-axis self-attention modules: one applying blocked local partitioning within non-overlapping $P \times P$ windows ($P = 8$), and one applying dilated grid-global attention across block positions. This decomposition reduces self-attention complexity from $\mathcal{O}(H^2W^2)$ to $\mathcal{O}(HW)$ while preserving a global receptive field. Stage dimensions, block counts, and attention configurations specific to the 128×128 input are detailed in Appendix B.

After the final stage, spatial features are aggregated by global average pooling to yield a 768-dimensional feature vector \mathbf{f} encoding global pore geometry:

$$\mathbf{f} = \frac{1}{H_{\text{final}} \cdot W_{\text{final}}} \sum_{i=1}^{H_{\text{final}}} \sum_{j=1}^{W_{\text{final}}} \mathbf{x}_{ij}^{\text{stage4}}. \quad (6)$$

A two-layer MLP regression head maps this representation to the four-element permeability output (Phases 2 and 3):

$$\mathbf{h}_0 = \text{LayerNorm}(\mathbf{f}), \quad (7)$$

$$\mathbf{h}_1 = \text{Dropout}_{0.1}(\text{GELU}(\text{Linear}_{768 \rightarrow 256}(\mathbf{h}_0))), \quad (8)$$

$$\mathbf{h}_2 = \text{Dropout}_{0.1}(\text{GELU}(\text{Linear}_{256 \rightarrow 128}(\mathbf{h}_1))), \quad (9)$$

$$\mathbf{K}_{\text{pred}} = \text{Linear}_{128 \rightarrow 4}(\mathbf{h}_2). \quad (10)$$

The complete architecture comprises approximately 119.01 million parameters: the MaxViT-Base backbone (convolutional stem and four hierarchical stages, with the classification head removed) contributes 118.78M, and the regression head contributes 0.23M. The porosity encoder and FiLM conditioning layers introduced in Phase 4 (Section 2.3.3) add a further 0.11M parameters.

2.2.2 Porosity-Conditioned Feature Modulation

Phase 4 introduces an explicit physics-informed conditioning mechanism in which scalar porosity modulates backbone feature representations, encoding the physical relationship between porosity and transport-coefficient magnitude directly into the model.

A three-layer MLP encoder transforms the scalar porosity $\phi \in [0, 1]$ into a 64-dimensional embedding $\mathbf{e}_\phi \in \mathbb{R}^{64}$:

$$\mathbf{e}_\phi = \text{Linear}_{64 \rightarrow 64}(\text{ReLU}(\text{Linear}_{32 \rightarrow 64}(\text{ReLU}(\text{Linear}_{1 \rightarrow 32}(\phi))))). \quad (11)$$

Porosity is computed directly from the binary image as $\phi = 1 - \text{mean}(I)$, requiring no additional simulation and constituting a zero-cost auxiliary input.

Feature-wise Linear Modulation (FiLM) [73] layers then modulate backbone feature maps $\mathbf{x} \in \mathbb{R}^{H \times W \times C}$ at Stages 2, 3, and 4:

$$\gamma_\phi = \text{Linear}_{64 \rightarrow C}(\mathbf{e}_\phi) \in \mathbb{R}^C, \quad \beta_\phi = \text{Linear}_{64 \rightarrow C}(\mathbf{e}_\phi) \in \mathbb{R}^C, \quad (12)$$

$$\mathbf{x}_{\text{mod}} = \gamma_\phi \odot \mathbf{x} + \beta_\phi, \quad (13)$$

where \odot denotes elementwise multiplication with broadcasting over spatial dimensions. Scale and shift parameters are initialized to produce identity modulation ($\gamma = \mathbf{1}$, $\beta = \mathbf{0}$) at training onset, ensuring stability.

Stage 1 is excluded because its features encode low-level edge detection and solid-fluid boundary localization, representing a length scale at which porosity provides no physically meaningful conditioning context. Stages 2–4 encode progressively more abstract geometric descriptions, including connectivity patterns, channel topology, and global pore-network structure, where porosity is a physically meaningful modulator of transport-coefficient magnitude. This placement was confirmed by a five-configuration validation-set ablation, and the encoder dimensionality of 64 was selected from $\{32, 64, 128\}$ by the same procedure; full ablation results and rationale are reported in Appendix C.

The total trainable parameter count in Phase 4 comprises the porosity encoder (0.01M), three FiLM layer pairs (0.10M), and the regression head (0.23M), totaling 0.34M parameters, representing 0.3% of the full model.

2.3 Progressive Training Strategy

Training is organized into four numbered phases. Phase 1 constitutes dataset curation, LBM simulation, and the comprehensive characterization study described in Section 2.1 and Appendix A; it produces no trained model and is not discussed further here. Phases 2–4 form the progressive learning curriculum: each initializes from the best checkpoint of the preceding phase and introduces a single, physically motivated methodological contribution—supervised transfer learning with D4-equivariant augmentation (Phase 2), advanced augmentation with enhanced off-diagonal loss weighting (Phase 3), and frozen-backbone porosity conditioning with weight-averaged ensemble (Phase 4)—enabling unambiguous attribution of performance gains to each intervention. Full hyperparameter specifications for all phases are consolidated in Appendix D. The complete pipeline is illustrated in Figure 1.

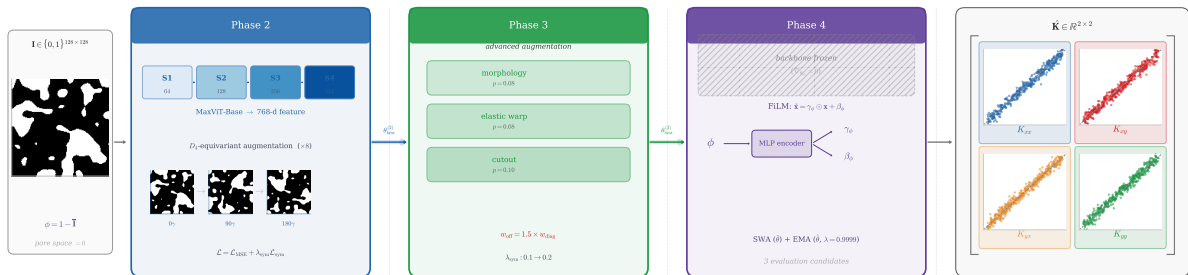


Figure 1: Overview of the physics-informed progressive transfer learning pipeline for permeability tensor prediction. *Input (far left):* a binary porous media image $\mathbf{I} \in \{0, 1\}^{128 \times 128}$ with porosity $\phi = 1 - \bar{\mathbf{I}}$, where pixel values of 1 denote solid grains and 0 denote pore space. *Phase 2 (blue):* the ImageNet-pretrained MaxViT-Base backbone processes the image through four hierarchical stages (S1–S4, channels 64–512) to produce a 768-dimensional feature vector; D4-equivariant augmentation applies all eight dihedral symmetries (three rotations shown) with consistent tensor transformation, and the physics-aware loss enforces tensor symmetry ($\lambda_{\text{sym}} = 0.1$). Phases are connected by checkpoint transfer arrows labeled $\theta_{\text{best}}^{(k)}$. *Phase 3 (green):* three supplementary augmentation classes—morphological operations ($p = 0.08$), elastic deformation ($p = 0.08$), and cutout masking ($p = 0.10$)—are introduced alongside doubled symmetry weighting ($\lambda_{\text{sym}} = 0.2$) and off-diagonal loss prioritization ($w_{\text{off}} = 1.5 w_{\text{diag}}$). *Phase 4 (purple):* the backbone is frozen ($\nabla_{\theta_{\text{bb}}} = 0$, indicated by hatching) while a porosity MLP encoder drives FiLM conditioning ($\tilde{\mathbf{x}} = \gamma_{\phi} \odot \mathbf{x} + \beta_{\phi}$) at Stages 2–4; Stochastic Weight Averaging (SWA) and Exponential Moving Average (EMA) produce three evaluation candidates from a single training run. *Output (far right):* the predicted permeability tensor $\hat{\mathbf{K}} \in \mathbb{R}^{2 \times 2}$, with representative parity plots shown for all four components ($K_{xx}, K_{xy}, K_{yx}, K_{yy}$).

2.3.1 Phase 2: Supervised Baseline with Progressive Unfreezing

Phase 2 establishes the supervised baseline using the ImageNet-pretrained MaxViT backbone combined with D4-equivariant augmentation (Section 2.5.1). To prevent catastrophic forgetting of pretrained representations, the trainable parameter set is expanded progressively over 600 epochs: only the regression head is optimized during epochs 0–50; backbone Stages 3–4 are unfrozen during epochs 50–150; and full end-to-end fine-tuning proceeds from epoch 150 onward. This curriculum allows the randomly initialized regression head to adapt to the permeability prediction task before backbone weights are updated, reducing the risk of destabilizing pretrained features. The physics-aware loss (Section 2.4) is applied with $\lambda_{\text{sym}} = 0.1$ and $\lambda_{\text{pos}} = 0.05$; the off-diagonal prioritization term is not active in this phase.

2.3.2 Phase 3: Advanced Augmentation and Optimized Loss

Phase 3 initializes from the Phase 2 best checkpoint and trains for an additional 600 epochs. Three supplementary augmentation classes are introduced at carefully tuned intensities (Section 2.5.2). The loss function is enhanced with a doubled symmetry weight ($\lambda_{\text{sym}} = 0.2$) and the off-diagonal prioritization term $\mathcal{L}_{\text{offdiag}}$ (Section 2.4), which applies a $1.5 \times$ weight to K_{xy} and K_{yx} predictions, addressing the performance disparity between diagonal and off-diagonal components observed in Phase 2. The increased symmetry weight couples the learning dynamics of K_{xy} and K_{yx} , allowing gradients computed on either element to inform the other.

2.3.3 Phase 4: Physics-Informed Conditioning with Weight Averaging

Phase 4 initializes from the Phase 3 best checkpoint with the MaxViT backbone frozen throughout. Only the newly introduced porosity encoder, FiLM layers, and regression head are optimized (0.34M parameters; 0.3% of total). The frozen-backbone strategy offers three key properties: *stability*, eliminating the risk of corrupting learned pore-scale geometry representations through further gradient updates; *efficiency*, as backpropagation bypasses frozen layers, substantially reducing memory consumption and training time; and *interpretability*, ensuring that any performance improvement is attributable solely to the porosity conditioning mechanism.

Two complementary weight-averaging strategies improve generalization by exploiting flatter, wider regions of the loss landscape:

Stochastic Weight Averaging (SWA) [74]. From epoch 400 onward, a running arithmetic mean of model weights is maintained at a fixed learning rate of 5×10^{-6} , aggregating 200 snapshots without additional training cost. After training, batch-normalization statistics are recalibrated via a single pass through the training set to restore accuracy.

Exponential Moving Average (EMA) [80]. A continuously updated exponentially-weighted parameter average is maintained throughout training with decay $\lambda_{\text{EMA}} = 0.9999$, corresponding to an effective window of approximately 10,000 gradient steps. EMA filters high-frequency weight fluctuations while tracking the optimization trajectory, consistently outperforming instantaneous weights on validation data.

Phase 4 training produces three evaluation candidates sharing the same architecture: the best instantaneous checkpoint θ_{best} , the SWA-averaged model θ_{SWA} , and the EMA-averaged model θ_{EMA} . All three are evaluated independently with test-time D4 augmentation to avoid selection bias. Full mathematical formulations, update rules, and batch-normalization recalibration details appear in Appendix F.

2.4 Physics-Aware Loss Function

The training objective combines four terms that jointly enforce predictive accuracy and physical validity:

$$\mathcal{L}_{\text{perm}} = \mathcal{L}_{\text{MSE}} + \lambda_{\text{sym}} \mathcal{L}_{\text{sym}} + \lambda_{\text{pos}} \mathcal{L}_{\text{pos}} + \lambda_{\text{offdiag}} \mathcal{L}_{\text{offdiag}}. \quad (14)$$

Phase-specific weight values are reported in Appendix D.

Reconstruction loss. The primary term penalizes tensor-level prediction error via the Frobenius norm:

$$\mathcal{L}_{\text{MSE}} = \frac{1}{N} \sum_{i=1}^N \|\mathbf{K}_i^{\text{pred}} - \mathbf{K}_i^{\text{true}}\|_F^2. \quad (15)$$

Symmetry constraint. Tensor symmetry ($K_{xy} = K_{yx}$) is enforced through a soft quadratic penalty on the off-diagonal discrepancy:

$$\mathcal{L}_{\text{sym}} = \frac{1}{N} \sum_{i=1}^N (K_{xy,i}^{\text{pred}} - K_{yx,i}^{\text{pred}})^2. \quad (16)$$

Although ground-truth labels satisfy symmetry to near-machine precision (Table 3), unconstrained regression does not inherently learn this property, motivating explicit soft enforcement. The weight λ_{sym} is increased from 0.1 in Phase 2 to 0.2 in Phases 3–4, coupling the learning dynamics of K_{xy} and K_{yx} and improving overall off-diagonal accuracy.

Positivity constraint. A squared hinge loss with margin $\varepsilon = 0.001$ enforces strictly positive diagonal elements:

$$\mathcal{L}_{\text{pos}} = \frac{1}{N} \sum_{i=1}^N \left[\max(0, \varepsilon - K_{xx,i}^{\text{pred}})^2 + \max(0, \varepsilon - K_{yy,i}^{\text{pred}})^2 \right]. \quad (17)$$

The penalty activates only for sub-margin predictions, providing directed gradient signal without penalizing physically valid outputs. The non-zero margin ensures predicted permeabilities exceed zero by a meaningful amount, improving numerical stability in downstream flow simulations.

Off-diagonal prioritization. A component-weighted mean squared error amplifies gradients for the more challenging off-diagonal elements:

$$\mathcal{L}_{\text{offdiag}} = \frac{1}{N} \sum_{i=1}^N \left[w_d (K_{xx,i}^{\text{err}})^2 + w_o (K_{xy,i}^{\text{err}})^2 + w_o (K_{yx,i}^{\text{err}})^2 + w_d (K_{yy,i}^{\text{err}})^2 \right], \quad (18)$$

where $K_{jk,i}^{\text{err}} = K_{jk,i}^{\text{pred}} - K_{jk,i}^{\text{true}}$, $w_d = 1.0$, and $w_o = 1.5$. This targeted emphasis addresses a fundamental prediction difficulty: diagonal permeabilities K_{xx} and K_{yy} correlate strongly with local pore geometry directly accessible through convolutional features, whereas off-diagonal elements K_{xy} and K_{yx} encode subtle geometric anisotropies requiring global spatial integration, precisely the regime in which the multi-axis attention mechanism provides its principal advantage. The 50% weight increase provides a stronger learning signal for off-diagonal components without overwhelming the overall loss landscape.

2.5 Data Augmentation Strategy

2.5.1 Phase 2: D4-Equivariant Augmentation

For isotropic porous media, the permeability tensor is invariant under the dihedral group D_4 , comprising eight elements: the identity, rotations by 90° , 180° , and 270° , and reflections about the horizontal, vertical, diagonal, and anti-diagonal axes [81, 82]. Each training sample undergoes a uniformly random D_4 transformation at every epoch, multiplying the effective dataset size by a factor of eight at no additional labeling cost.

Physically consistent augmentation requires simultaneous transformation of both the image and the permeability tensor. Under a coordinate transformation represented by matrix \mathbf{P} , the second-order permeability tensor transforms as:

$$\mathbf{K}' = \mathbf{P} \mathbf{K} \mathbf{P}^T. \quad (19)$$

For example, the 90° rotation matrix $\mathbf{P}_{90} = \begin{bmatrix} 0 & -1 \\ 1 & 0 \end{bmatrix}$ yields:

$$\mathbf{K}' = \begin{bmatrix} K_{yy} & -K_{yx} \\ -K_{xy} & K_{xx} \end{bmatrix}. \quad (20)$$

Transformation matrices for all eight D_4 elements are tabulated in Appendix E. Because these symmetries are exact for isotropic media, D_4 augmentation constitutes physically rigorous regularization rather than an approximation. The equivariance achieved is statistical rather than architectural; group-equivariant convolutional networks [70, 72], which build exact equivariance into the weight-sharing structure, were not adopted because doing so would require training from scratch and discarding the ImageNet pretraining central to the transfer-learning strategy employed here. A detailed discussion of this design choice appears in Appendix E.2.

2.5.2 Phase 3: Advanced Augmentation

Three additional transformation classes are applied sequentially after D_4 augmentation, at intensities determined by a two-stage validation-set grid search (Appendix E):

Morphological operations. Erosion and dilation with a 3×3 structuring element, each applied with probability 0.08, simulate natural variability in pore-throat geometry. No explicit tensor transformation is required, as the network learns the permeability of the morphologically modified geometry through convolutional feature extraction.

Elastic deformation. Smooth coordinate warping is generated from Gaussian-smoothed uniform random displacement fields, with displacement magnitude $\alpha = 3.0$ pixels, smoothing $\sigma = 2.0$ pixels, and application probability 0.08. Elastic deformation requires an explicit permeability tensor transformation according to the local deformation Jacobian \mathbf{J} :

$$\mathbf{K}' = \mathbf{J} \mathbf{K} \mathbf{J}^T, \quad \mathbf{J} = \begin{bmatrix} 1 + \partial_x \delta_x & \partial_y \delta_x \\ \partial_x \delta_y & 1 + \partial_y \delta_y \end{bmatrix}, \quad (21)$$

approximated at the image center via central finite differences, followed by symmetrization $\mathbf{K}' \leftarrow (\mathbf{K}' + \mathbf{K}'^T)/2$.

Cutout masking. Random 8×8 pixel rectangular regions are masked to a neutral value of 0.5 with probability 0.10, forcing distributed feature learning by preventing reliance on any single spatial region. No tensor transformation is required.

Augmentation parameters were optimized by targeting off-diagonal R^2 as the primary criterion, as diagonal components proved robustly learned across the full search range while off-diagonal prediction was the most sensitive indicator of augmentation quality. Total combined perturbation probability is held below approximately 35% to avoid gradient variance that would impede off-diagonal convergence. The full parameter search procedure and pipeline pseudocode appear in Appendix E.

2.6 Implementation and Evaluation

2.6.1 Implementation Details

All models were implemented in PyTorch 2.6.0 using the `timm` 1.0.22 library and trained on a single NVIDIA RTX 6000 Ada Generation GPU (48 GB VRAM) under CUDA 12.4. Automatic mixed precision was disabled across all phases to ensure numerical stability in physics-constraint calculations and maintain gradient precision for the small trainable parameter set of Phase 4. Random seeds were fixed at 42 for NumPy, PyTorch, and Python’s `random` module to ensure reproducibility. Deterministic CuDNN algorithms were not enforced to allow benchmark-mode acceleration, providing approximately 15% training speedup without observable impact on cross-run reproducibility.

Training follows a sequential protocol across phases. Phase 2 trains from ImageNet-pretrained weights for 600 epochs. Phase 3 initializes from the Phase 2 best checkpoint for a further 600 epochs. Phase 4 initializes from the Phase 3 best checkpoint with the backbone frozen, training only the porosity encoder, FiLM layers, and regression head for 600 epochs. Phase 4 model variants (θ_{best} , θ_{SWA} , θ_{EMA}) share identical architecture and forward-pass computation graphs; weight-averaging affects only the parameter values loaded at inference and introduces no additional computational cost. All Phase 4 variants achieve an inference latency of approximately 120 ms per sample on the NVIDIA RTX 6000 Ada (mean over 1,000 independent predictions), compared to hours per sample for LBM simulation. Complete optimizer configurations, learning-rate schedules, batch sizes, and early-stopping criteria for each phase are reported in Appendix D.

2.6.2 Evaluation Metrics

Model performance is assessed through four complementary metric classes.

Coefficient of determination (R^2). The primary accuracy metric measures the proportion of variance explained:

$$R^2 = 1 - \frac{\sum_{i=1}^N (y_i^{\text{pred}} - y_i^{\text{true}})^2}{\sum_{i=1}^N (y_i^{\text{true}} - \bar{y})^2}, \quad (22)$$

reported as an overall variance-weighted score across all four tensor components and as per-component values for $[K_{xx}, K_{xy}, K_{yx}, K_{yy}]$.

Mean squared error (MSE). Absolute tensor-level prediction error is quantified via the Frobenius norm (Equation 15).

Relative root mean squared error (RRMSE). To enable direct comparison between the large-magnitude diagonal and near-zero-mean off-diagonal components, scale-invariant relative error is reported per tensor component:

$$\text{RRMSE}_{jk} = \frac{\sqrt{\frac{1}{N} \sum_i (K_{jk,i}^{\text{pred}} - K_{jk,i}^{\text{true}})^2}}{\bar{K}_{jk}^{\text{true}}}, \quad (23)$$

normalized by the mean absolute test-set value $\bar{K}_{jk}^{\text{true}}$. A value of, say, 5% on K_{xx} corresponds directly to a 5% uncertainty in the principal flow resistance.

Physical validity metrics. Symmetry is quantified by the mean symmetry error $\varepsilon_{\text{sym}} = \mathbb{E}[|K_{xy}^{\text{pred}} - K_{yx}^{\text{pred}}|]$ and the fraction of test predictions satisfying $|K_{xy} - K_{yx}| < 10^{-3}$. Positivity is assessed by the fraction of predictions satisfying $K_{xx}, K_{yy} > 0$. The reported $\varepsilon_{\text{sym}} = 3.95 \times 10^{-7}$ represents engineering-level precision far exceeding practical requirements, though not machine precision in the strict floating-point sense ($\sim 10^{-16}$ for FP64); the term “near-machine precision” is therefore used in this context.

Extended metrics for cross-study comparison, including mean absolute percentage error (MAPE), range-normalized RMSE, Willmott’s index of agreement, the Kling-Gupta efficiency, and Spearman rank correlation, are defined in Appendix G.

3 Results and Discussion

The progressive training framework is evaluated on a held-out test set of 4,000 porous media samples spanning three orders of magnitude in permeability ($K \in [0.002, 3.19]$ in lattice units), never accessed during model development, hyperparameter selection, or any training decision. Three training phases are assessed in sequence: Phase 2 establishes the supervised baseline with ImageNet-pretrained MaxViT and D4-equivariant augmentation; Phase 3 introduces advanced augmentation and the enhanced physics-aware loss; and Phase 4 applies frozen-backbone transfer learning with porosity-conditioned FiLM layers and ensemble weight averaging. Each phase is evaluated independently, enabling attribution of performance gains to specific methodological contributions. The evaluation protocol, metrics, and physical validity criteria are defined in Section 2.6.2; comprehensive dataset statistics and cross-split consistency verification are reported in Appendix A.

3.1 Dataset Overview and Structure-Property Relationships

Figure 2 presents representative binary microstructures spanning the porosity and anisotropy spectrum, illustrating the geometric diversity of the dataset. Low-porosity samples ($\phi < 0.40$) exhibit dense solid matrices with isolated, tortuous pore channels and correspondingly small permeabilities; moderate-porosity samples ($0.40 \leq \phi \leq 0.70$) display increasingly interconnected pore networks and non-negligible off-diagonal coupling; and high-porosity samples ($\phi > 0.70$) feature well-connected, nearly isotropic networks with large diagonal permeabilities.

Figure 3 presents component-wise porosity-permeability relationships for all 20,000 labeled samples, revealing the fundamental structure-property correlations that govern model learning. Diagonal permeabilities K_{xx} and K_{yy} exhibit strong positive correlation with porosity (Spearman $\rho_s \approx +0.940$, Pearson $r \approx +0.795$, $p \approx 0$), confirming that pore volume fraction governs primary transport capacity and motivating the porosity-conditioned FiLM design in Phase 4 (Section 2.2.2). The joint distributions reveal right-skewed marginal porosity (skewness ≈ -0.55 , concentrated in the moderate-to-high connectivity regime) and heavy-tailed component distributions spanning three orders of magnitude. Off-diagonal elements K_{xy} and K_{yx} exhibit negligible correlation with

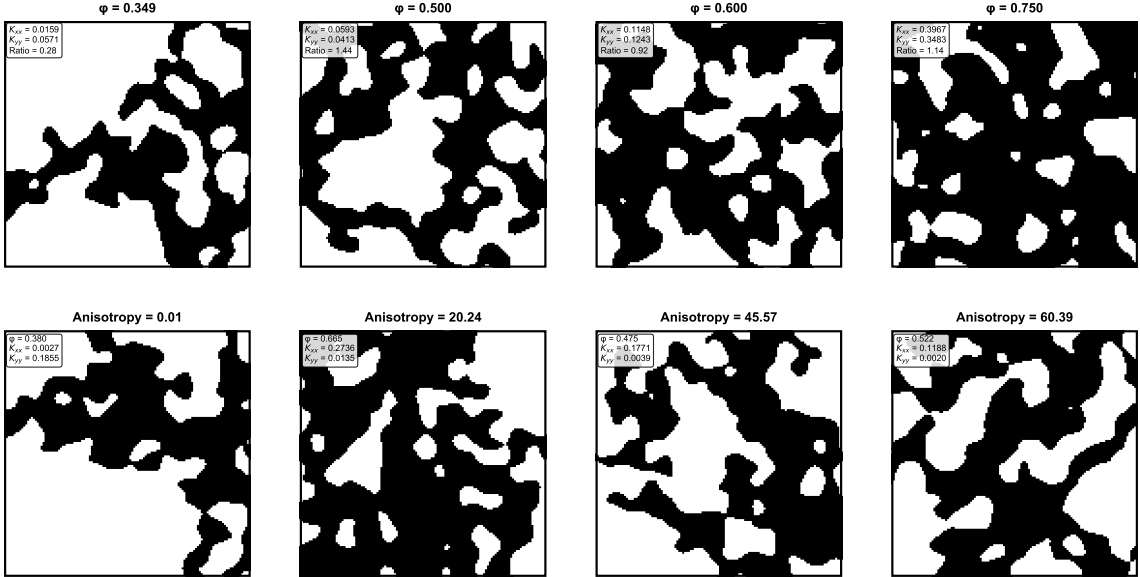


Figure 2: Representative binary porous media microstructures spanning the porosity and anisotropy spectrum. Each panel shows a 128×128 binary image (white: solid matrix; black: void space) with corresponding porosity ϕ and permeability tensor components. The progression from low to high porosity illustrates the transition from tortuous isolated pore channels (small diagonal permeability, negligible off-diagonal coupling) to well-connected isotropic networks (large nearly equal K_{xx} , K_{yy}). Samples with significant off-diagonal components ($|K_{xy}| > 0.05$) are associated with oblique pore-channel orientations rather than porosity magnitude, consistent with the near-zero porosity-to-off-diagonal correlation ($\rho_s \approx 0.01$) reported in Appendix A.3.

porosity ($\rho_s \approx +0.01$, not significant), confirming that cross-directional coupling arises solely from geometric anisotropy and is independent of pore volume fraction. This dissociation is a key dataset characteristic: diagonal and off-diagonal permeabilities encode physically distinct information, the former captured by scalar porosity and the latter requiring spatial integration of geometric anisotropy features, which directly motivates the component-specific loss weighting introduced in Phase 3 (Section 2.4). The symmetric clustering of off-diagonal components about zero (mean $|\bar{K}_{xy}| < 0.002$, kurtosis ≈ 9 –13) confirms ground-truth tensor symmetry, and all 20,000 labeled tensors are strictly positive-definite, providing thermodynamically consistent training labels free of simulation artifacts.

The dataset presents three distinct challenges for permeability prediction. First, the three-order-of-magnitude dynamic range in diagonal permeability demands model capacity to resolve both low-connectivity sparse networks and high-connectivity continuum-limit behavior across the full spectrum simultaneously. Second, the off-diagonal components, independent of porosity and encoded exclusively in spatial geometric anisotropy, require global feature integration at scales comparable to the representative elementary volume (REV), a regime where convolutional features alone are insufficient. Third, the five-fold scale disparity between diagonal and off-diagonal standard deviations ($\approx 5.1\times$ across all splits; Appendix A.1) creates an implicit loss-weighting imbalance in naive MSE training, motivating explicit off-diagonal prioritization. These challenges are addressed directly by the architectural and training design decisions described in Section 2, and the following subsections assess the extent to which each phase of training resolves them.

3.2 Phase 2: Supervised Baseline with D4-Equivariant Augmentation

Phase 2 establishes the supervised baseline by fine-tuning ImageNet-pretrained MaxViT with progressive unfreezing and D4-equivariant augmentation (Section 2.3.1). The model achieves an overall variance-weighted $R^2 = 0.9843$ on the 4,000-sample test set, with $\text{RMSE} = 1.697 \times 10^{-2}$,

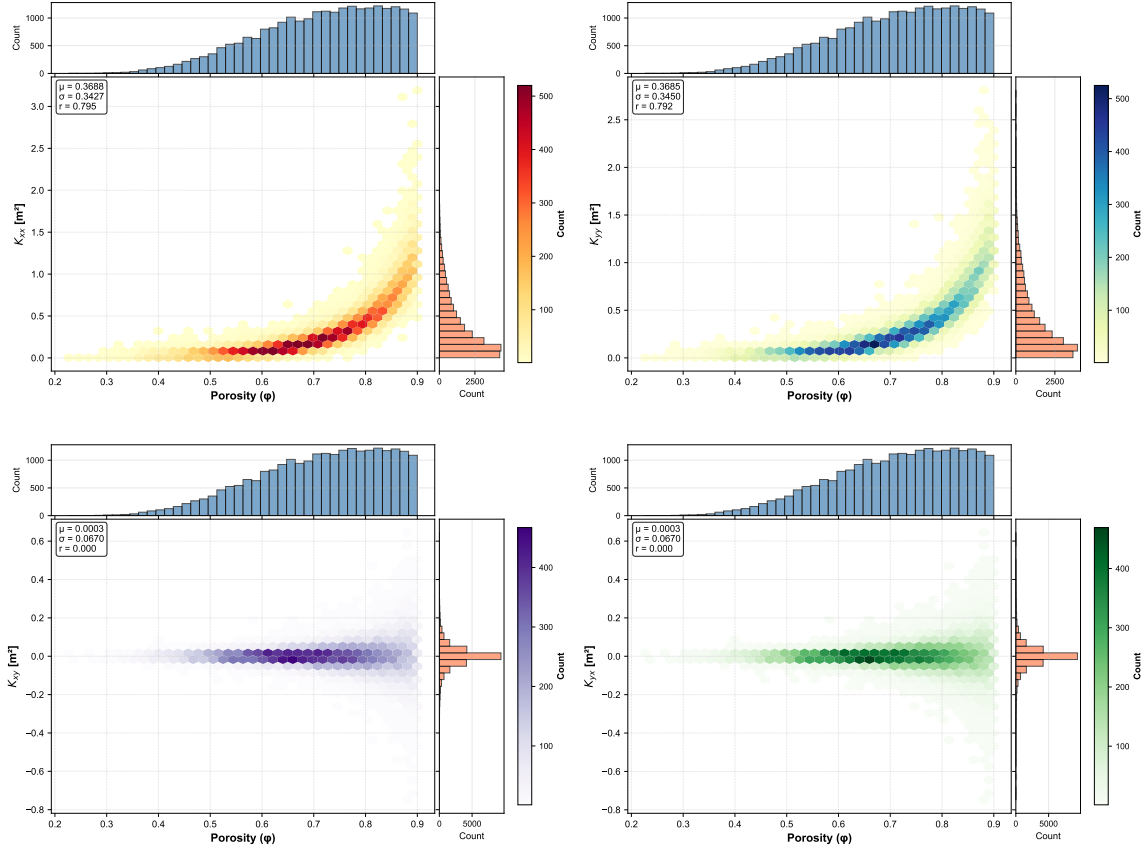


Figure 3: Component-wise porosity-permeability relationships across all 20,000 labeled samples, shown as hexbin density plots with marginal histograms. Color intensity indicates sample density. (a) K_{xx} versus ϕ : strong positive correlation ($\rho_s = +0.940$, $r = +0.795$), spanning three orders of magnitude; scatter increases at high porosity, reflecting geometric diversity beyond scalar pore fraction. (b) K_{yy} versus ϕ : nearly identical statistics and correlation structure to K_{xx} , confirming statistical isotropy at the dataset level despite individual-sample anisotropy. (c) K_{xy} versus ϕ : negligible correlation ($\rho_s \approx +0.01$, $p > 0.05$); off-diagonal coupling clusters symmetrically near zero, independent of pore volume fraction. (d) K_{yx} versus ϕ : identical to K_{xy} , confirming near-machine-precision ground-truth symmetry ($\varepsilon_{\text{sym}} < 8 \times 10^{-6}$, Table 3). The contrast between panels (a,b) and (c,d) constitutes the fundamental prediction-difficulty asymmetry between diagonal and off-diagonal tensor components that the progressive training strategy is designed to address.

MAE = 1.091×10^{-2} , Pearson $r = 0.9985$, Spearman $\rho_s = 0.9957$, Willmott $d = 0.9992$, and KGE = 0.988, confirming that ImageNet-pretrained features transfer effectively to binary porous media despite the substantial domain difference. Table 1 reports the full component-wise metric suite.

3.2.1 Component-Wise Performance Asymmetry

The component-wise parity plots in Figure 4 are the primary diagnostic result of Phase 2. Diagonal components achieve $R_{K_{xx}}^2 = 0.9961$ and $R_{K_{yy}}^2 = 0.9962$, with RRMSE of 5.77% and 5.70% respectively. Off-diagonal components achieve $R_{K_{xy}}^2 = R_{K_{yx}}^2 = 0.9725$, a gap of 236 basis points relative to diagonal performance, with RRMSE of 26.07%, approximately 4.5 \times larger than for diagonal elements. The very low KGE values for off-diagonal components (0.176, compared to ≈ 0.987 for diagonal) further characterize this asymmetry: KGE decomposition reveals that the deficit arises primarily from a poor variability ratio, meaning the model systematically under-disperses predictions for K_{xy} and K_{yx} , compressing the predicted distribution toward zero relative to the ground truth. The computed MAPE values were not meaningful for off-diagonal

Table 1: Phase 2 test-set performance by tensor component. RRMSE: relative root mean squared error (normalized by component mean absolute value; Equation 23). MAPE values for off-diagonal components are large because the denominator (mean absolute true value) approaches zero; RRMSE is the appropriate relative-error metric for near-zero-mean components. KGE: Kling-Gupta efficiency [83]. d : Willmott index of agreement [84].

Component	R^2	RMSE	MAE	RRMSE (%)	KGE	d
K_{xx}	0.9961	2.147×10^{-2}	1.430×10^{-2}	5.77	0.986	0.9990
K_{yy}	0.9962	2.124×10^{-2}	1.394×10^{-2}	5.70	0.989	0.9990
K_{xy}	0.9725	1.095×10^{-2}	7.70×10^{-3}	26.07	0.176	0.9930
K_{yx}	0.9725	1.095×10^{-2}	7.70×10^{-3}	26.07	0.176	0.9930
Overall	0.9843	1.796×10^{-2}	1.091×10^{-2}	8.19	0.988	0.9992

components because the MAPE denominator approaches zero for near-zero-mean quantities; RRMSE is the appropriate relative-error metric in this regime (Appendix G).

3.2.2 Anisotropy-Stratified Analysis

Figure 5 stratifies prediction performance by tensor anisotropy ratio $AR = \lambda_{\max}/\lambda_{\min}$ across ten equi-populated bins (400 samples each) spanning the 2nd–98th percentile of the AR distribution. Panel (a) confirms that the test set is predominantly near-isotropic (median $AR = 1.624$; Appendix A.1), with a long, sparsely populated tail: approximately 4% of samples have $AR > 5$ and only 1% exceed $AR = 10.0$ (p_{99}).

Panels (b) and (c) reveal a pattern that is the inverse of naive expectation. The diagonal-to-off-diagonal R^2 gap is largest not at high AR but at the *lowest* anisotropy ratios: for the first bin ($AR \approx 1.11$), diagonal R^2 remains excellent at 0.996 while off-diagonal R^2 collapses to 0.802, a gap of $\Delta R^2 = 0.194$. This gap narrows rapidly with increasing AR, reaching $\Delta R^2 < 0.02$ for $AR > 1.5$ and a minimum of 0.011 near $AR \approx 1.89$. A modest secondary widening occurs at the highest AR bin ($AR \approx 5.87$; $\Delta R^2 = 0.027$), where off-diagonal R^2 declines to 0.960, consistent with the high-AR analysis from Appendix H.4 ($R_{\text{off}}^2 = 0.968$ for the top 12.5% most anisotropic samples).

The collapse of off-diagonal R^2 at near-isotropic AR has two compounding causes. First, a variance normalization effect: when AR is close to unity, true K_{xy} values are near zero with very low variance, so even small absolute prediction errors drive R^2 toward zero because the denominator of Equation 22 is near zero. Second, a genuine learning difficulty: the model must resolve extremely subtle geometric asymmetries in nearly isotropic media to distinguish, say, $K_{xy} = 0.01$ from $K_{xy} = -0.01$, a task requiring sensitivity to weak spatial orientation cues that are easily obscured by augmentation noise. At high AR, the larger absolute off-diagonal coupling values provide a stronger learning signal, allowing the model to resolve cross-directional flow paths more reliably; accordingly, R_{off}^2 at $AR \approx 5.87$ (0.960) substantially exceeds the lowest-bin value (0.802) despite the greater geometric complexity.

Panel (d) further corroborates this interpretation: diagonal residuals are compact and nearly symmetric across all AR bins, while off-diagonal residual distributions are widest at low AR where coupling values are near-zero and noisiest. Taken together, these results identify the prediction of weak off-diagonal coupling in near-isotropic media, rather than the prediction of strongly anisotropic tensors, as the primary Phase 2 failure mode. This motivates the Phase 3 off-diagonal prioritization term $\mathcal{L}_{\text{offdiag}}$ (Section 2.4), which amplifies gradients for K_{xy} and K_{yx} regardless of their absolute magnitude, and the calibrated augmentation strategy (Section 2.5.2), which preserves the weak orientation signals in near-isotropic samples.

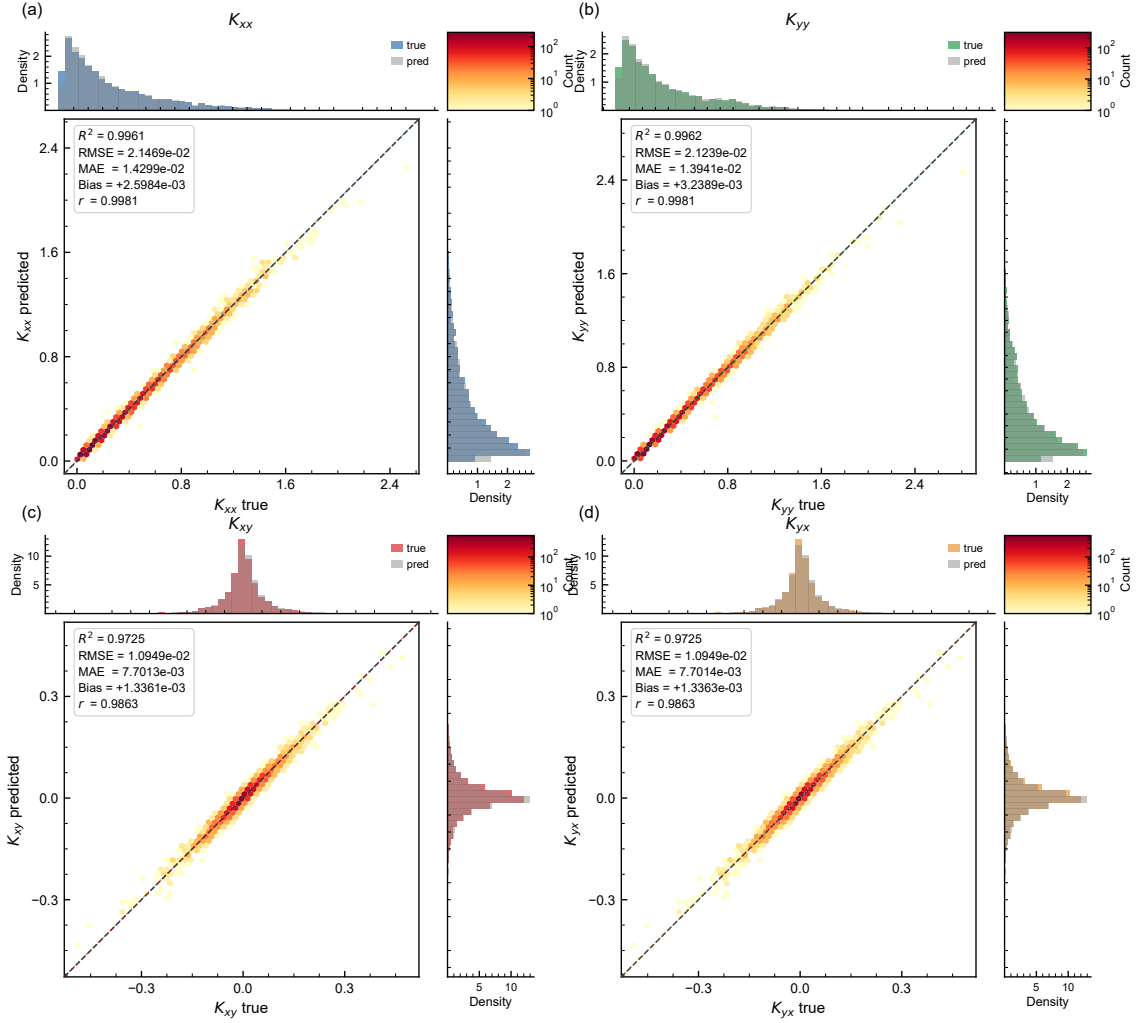


Figure 4: Component-wise parity plots for Phase 2 permeability tensor predictions. Each panel shows predicted versus true values for one tensor component, with hexbin color intensity proportional to log-density. Marginal histograms compare the distributions of true (gray) and predicted (colored) values. (a) K_{xx} ($R^2 = 0.9961$, RRMSE = 5.77 %): predictions closely track the identity line across the full three-order-of-magnitude range; slight scatter at extreme values reflects the sparsely populated tails of the training distribution. (b) K_{yy} ($R^2 = 0.9962$, RRMSE = 5.70 %): nearly identical accuracy to K_{xx} , confirming statistical isotropy in the backbone’s ability to resolve principal permeabilities. (c) K_{xy} ($R^2 = 0.9725$, RRMSE = 26.07 %): increased scatter around the identity line at large $|K_{xy}|$ values, with the marginal histogram revealing systematic under-dispersion (KGE = 0.176). (d) K_{yx} ($R^2 = 0.9725$, RRMSE = 26.07 %): essentially identical to K_{xy} , confirming that the symmetry constraint $K_{xy} \approx K_{yx}$ is learned accurately ($\varepsilon_{\text{sym}} = 1.39 \times 10^{-6}$, near-machine precision). The 236-basis-point R^2 gap between diagonal and off-diagonal components drives all subsequent Phase 3 interventions.

3.2.3 Physical Constraint Validation

Physical validity is enforced to near-machine precision. The mean symmetry error is $\varepsilon_{\text{sym}} = 1.39 \times 10^{-6}$ across all 4,000 test predictions, exceeding engineering requirements by several orders of magnitude and confirming that the symmetry penalty \mathcal{L}_{sym} (Equation 16) successfully couples the learning dynamics of K_{xy} and K_{yx} through the soft constraint. All 4,000 test tensors satisfy the positivity constraint ($K_{xx}, K_{yy} > 0$), yielding 100% thermodynamic validity without post-hoc projection. These physical constraint results are consistent across all subsequent training phases.

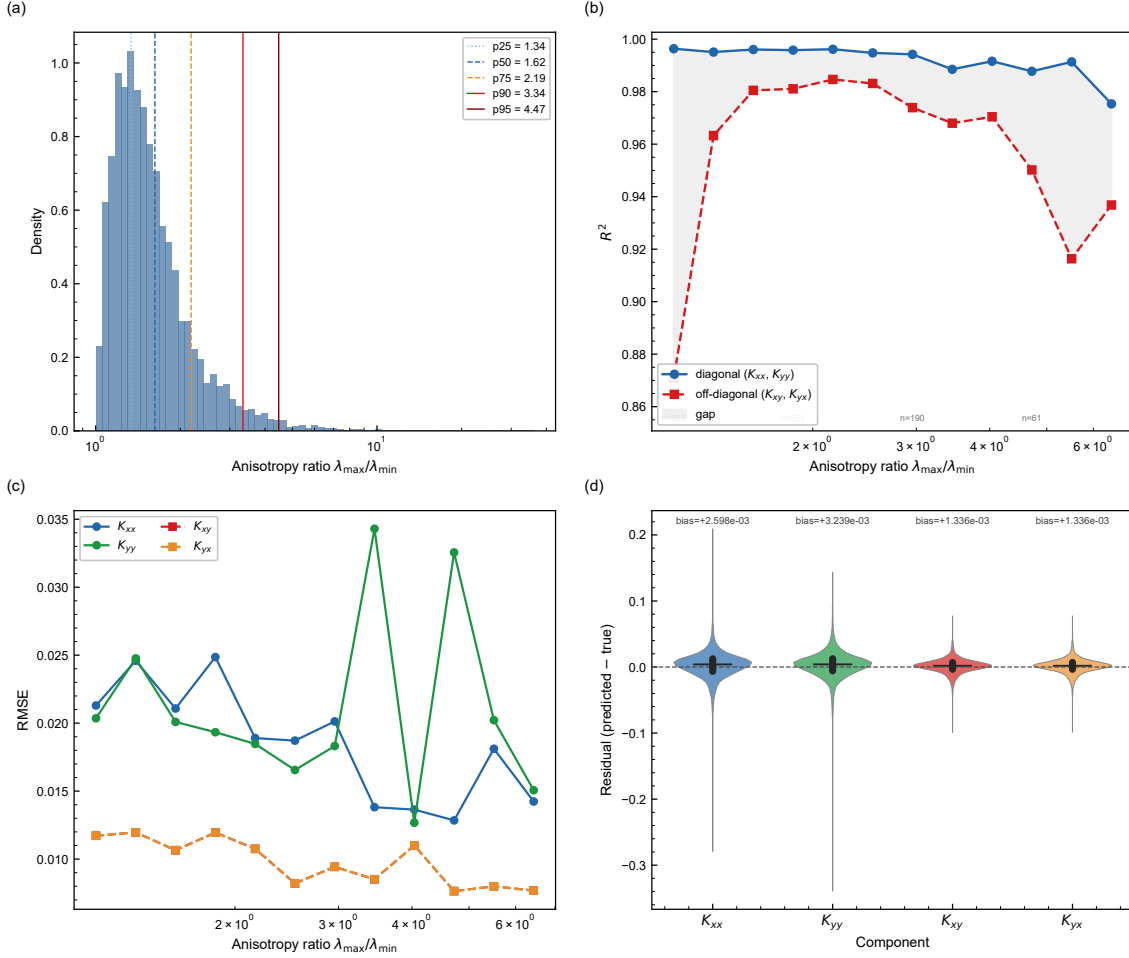


Figure 5: Anisotropy-stratified prediction performance for Phase 2 across ten equi-populated bins ($n = 400$ each) of tensor anisotropy ratio $AR = \lambda_{\max}/\lambda_{\min}$. (a) AR distribution of the 4,000 test samples (log-scale x -axis); vertical dashed lines mark the 50th, 90th, and 99th percentiles ($AR_{50} = 1.62$, $AR_{90} = 3.34$, $AR_{99} = 10.0$). (b) R^2 for diagonal (mean of K_{xx} , K_{yy}) and off-diagonal (mean of K_{xy} , K_{yx}) components versus AR bin center: the diagonal-to-off-diagonal gap is largest at the *lowest* anisotropy ratios ($\Delta R^2 = 0.194$ at $AR \approx 1.11$), narrows rapidly with increasing AR ($\Delta R^2 < 0.02$ for $AR > 1.5$), and exhibits a modest secondary widening at high AR ($\Delta R^2 = 0.027$ at $AR \approx 5.87$). This non-monotonic pattern identifies weak off-diagonal coupling in near-isotropic media as the dominant Phase 2 failure mode. (c) RMSE versus AR bin center for all four components; off-diagonal RMSE is elevated at both extremes of the AR spectrum while diagonal RMSE remains largely insensitive throughout. (d) Residual distributions per component (violin plots); off-diagonal interquartile ranges are widest at low AR, where near-zero coupling values produce low-variance targets that amplify the relative impact of prediction errors.

3.2.4 Mechanistic Interpretation and Motivation for Phase 3

The Phase 2 results expose a fundamental hierarchy in the permeability prediction task. Diagonal permeabilities correlate strongly with scalar porosity ($\rho_s \approx +0.940$; Appendix A.3) and are predominantly determined by local pore-throat geometry, making them accessible to the hierarchical convolutional features of the MaxViT backbone. Off-diagonal components encode geometric anisotropy that is independent of porosity ($\rho_s \approx +0.01$) and requires integration of orientation-dependent spatial correlations at the REV scale. The anisotropy-stratified analysis (Figure 5) reveals that off-diagonal prediction difficulty is concentrated at near-isotropic AR, where weak coupling signals are hardest to resolve, rather than at high AR where stronger coupling magnitudes provide a clearer learning signal. Two mechanisms compound this difficulty

in the near-isotropic regime. First, the diagonal-to-off-diagonal standard deviation ratio of $\approx 5.1 \times$ (Appendix A.1) causes naive MSE training to under-weight off-diagonal gradients relative to diagonal terms. Second, the D4-equivariant augmentation, while physically correct, exposes the model to all orientations of each microstructure, which may dilute the subtle orientation-specific cues on which weak off-diagonal coupling depends.

These observations motivate two targeted Phase 3 interventions: augmentations calibrated to enrich geometric anisotropy diversity without obscuring global connectivity patterns (Section 2.5.2), and explicit off-diagonal prioritization through loss weight $w_o = 1.5$ (Section 2.4). The progressive framework thereby functions as a structured ablation: Phase 2 isolates ImageNet pretraining and D4-equivariant augmentation; Phase 3 adds advanced augmentation and enhanced loss; Phase 4 adds frozen-backbone porosity conditioning and ensemble weight averaging, enabling unambiguous attribution of each performance gain.

3.3 Phase 3: Advanced Augmentation and Off-Diagonal Loss Optimization

Building on the Phase 2 diagnostic insights, Phase 3 introduces three targeted interventions to address the near-isotropic off-diagonal failure mode identified in Section 3.2.2: morphological operations (erosion and dilation, $p = 0.08$), elastic deformation ($p = 0.08$, $\alpha = 3.0$, $\sigma = 2.0$), and random cutout ($p = 0.10$, 8×8 pixels), combined with an enhanced physics-aware loss incorporating doubled symmetry weight ($\lambda_{\text{sym}} = 0.2$) and off-diagonal prioritization ($w_o = 1.5$). The combined augmentation rate of $\approx 24\%$ was validated on the validation set to lie below the $\approx 35\%$ threshold beyond which gradient variance degrades off-diagonal convergence while leaving diagonal learning intact (Section 2.5.2). Phase 3 achieves a variance-weighted $R^2 = 0.9945$ (component-averaged $R^2 = 0.9848$, 95% BCa CI [0.9833, 0.9860]) on the held-out test set, with RMSE = 1.697×10^{-2} (a 5.5% reduction from Phase 2’s 1.796×10^{-2}), RRMSE = 8.19%, Willmott $d = 0.9992$, and KGE = 0.9876. Full metrics are reported in Table 2.

3.3.1 Component-Wise Gains

Diagonal components improve modestly from Phase 2 to Phase 3 (R_{diag}^2 : 0.9955 \rightarrow 0.9961), confirming that the more aggressive augmentation pipeline does not erode the strong diagonal baseline. The primary gain is in the off-diagonal components (R_{off}^2 : 0.9725 \rightarrow 0.9740), with the diagonal-to-off-diagonal R^2 gap narrowing from $\Delta R^2 = 0.0230$ to 0.0221. The improvement is more pronounced in the high-anisotropy regime: for the top 500 most anisotropic test samples (top 12.5%), the high-AR ΔR^2 drops from 0.0209 to 0.0132—a 37% reduction—indicating that augmentation-induced geometric diversity and stronger off-diagonal gradients specifically benefit the regime where Phase 2 struggled most. Physical constraint enforcement tightens in parallel: the mean symmetry error falls from 1.39×10^{-6} to 7.69×10^{-7} (a 45% reduction), attributable to the doubled symmetry weight $\lambda_{\text{sym}} = 0.2$ coupling the learning dynamics of K_{xy} and K_{yx} more strongly. All 4,000 test predictions remain 100% positive-definite.

3.3.2 Residual Limitations and Motivation for Phase 4

Despite consistent gains across all metrics, a non-trivial off-diagonal performance gap persists ($\Delta R^2 = 0.0221$), and the near-isotropic failure mode is attenuated rather than eliminated. Two structural limitations remain. First, augmentation alone cannot supply information about the scalar porosity-to-permeability scaling relationship that the backbone does not already encode implicitly. Second, training all parameters simultaneously risks entangling the well-learned diagonal representations with the more volatile off-diagonal gradient signal. Phase 4 addresses both limitations through a frozen-backbone strategy with explicit porosity conditioning via FiLM layers (Section 2.3.3), providing a zero-cost physical prior for magnitude scaling while protecting the learned geometric representations from further modification.

3.4 Phase 4: Physics-Informed Transfer Learning with Ensemble Techniques

The core design principle of Phase 4 is deliberate separation of what is already known from what must still be learned. The MaxViT backbone (118.64M parameters) is frozen in its Phase 3 configuration: rather than continuing to fine-tune geometric features that already generalize well, the training budget is redirected toward encoding a physical prior that the backbone cannot discover from images alone—the strong porosity-to-permeability scaling relationship ($\rho_s \approx +0.940$; Appendix A.3). A compact physics-informed head (0.33M parameters, 0.28% of the total parameter budget) achieves this through a three-layer MLP porosity encoder producing a 64-dimensional embedding of scalar ϕ , which modulates backbone features via Feature-wise Linear Modulation (FiLM) layers inserted after MaxViT Stages 2–4 (Section 2.2.2). Stochastic Weight Averaging (SWA, epochs 400–600, $\eta_{\text{SWA}} = 5 \times 10^{-6}$) and Exponential Moving Average (EMA, $\lambda = 0.9999$) then stabilize the optimization trajectory around a flatter loss minimum (Appendix F). The result is a model that encodes what physics dictates explicitly, while leaving the backbone free to supply what physics cannot: the geometric anisotropy information that determines off-diagonal coupling independently of porosity.

3.4.1 Prediction Accuracy and Statistical Robustness

Phase 4 achieves a variance-weighted $R^2 = 0.9960$ and component-averaged $R^2 = 0.9863$ (95% BCa CI [0.9852, 0.9874], $B = 1,000$) on the held-out test set—a 33% reduction in unexplained variance relative to the Phase 2 baseline and a further 13% relative to Phase 3. Global errors are RMSE = 1.564×10^{-2} (95% BCa CI [0.01483, 0.01704]) and RRMSE = 7.55% (95% BCa CI [7.18, 8.19]%). The Kling-Gupta efficiency KGE = 0.9942 is particularly informative: it decomposes accuracy into correlation, bias, and variability components simultaneously, and its step-wise improvement across phases (0.9824 \rightarrow 0.9876 \rightarrow 0.9942) reflects a proportionately larger gain in Phase 3 \rightarrow 4 than Phase 2 \rightarrow 3—consistent with the FiLM conditioning correcting the remaining systematic bias and variability mismatch rather than merely reducing scatter. Table 2 presents the full three-phase comparison with bootstrap confidence intervals; the extended version with per-component and uncertainty metrics is in Appendix J.

A notable property of the full extended table (Appendix J, Table 15) is that every reported metric—across all 35 rows spanning global accuracy, rank agreement, per-component R^2 , relative errors, physics compliance, and uncertainty calibration—improves monotonically from Phase 2 through Phase 4. This consistency is not guaranteed by design: each phase optimizes a different objective configuration, and gains in one metric can in principle come at the expense of another. The absence of any such trade-off confirms that the staged methodological contributions—pretraining and equivariant augmentation, then augmentation diversity and loss rebalancing, then physics-informed conditioning and ensemble stabilization—are genuinely complementary rather than competing.

Per-component performance reinforces this picture. Diagonal components achieve $R_{K_{xx}}^2 = R_{K_{yy}}^2 = 0.9967$ with RRMSE of 5.25%–5.28% and MAPE of 7.09%–7.62%; KGE of 0.991–0.993 confirms that bias, variance ratio, and rank correlation all contribute negligibly to the residual error budget. Off-diagonal components reach $R_{K_{xy}}^2 = R_{K_{yx}}^2 = 0.9758$ (RRMSE = 24.43%), with KGE rising from 0.176 in Phase 2 to 0.761 in Phase 4—a $4.3\times$ improvement that directly reflects recovery from the variability under-dispersion identified in Section 3.2.1. The diagonal-to-off-diagonal R^2 gap narrows monotonically: $\Delta R^2 = 0.0230 \rightarrow 0.0221 \rightarrow 0.0209$ across Phases 2–4.

3.4.2 Component-Wise Parity and Prediction Distributions

Figure 6 presents the component-wise parity plots. Each panel combines a hexbin density map with marginal histograms, making both the conditional accuracy and the distributional fidelity visible simultaneously.

Table 2: Progressive performance across training phases on the held-out test set ($N = 4,000$). 95 % BCa bootstrap confidence intervals ($B = 1,000$) in brackets. **Bold** values indicate the best result per row. Phase 2: supervised baseline with D4 augmentation; Phase 3: advanced augmentation and enhanced physics-aware loss; Phase 4: frozen backbone, FiLM porosity conditioning, SWA/EMA ensemble.

Metric	Phase 4	Phase 3	Phase 2
<i>Global accuracy</i>			
R^2 (variance-weighted)	0.9960	0.9945	0.9940
R^2 (component-averaged)	0.9863	0.9848	0.9843
95 % BCa CI	[0.9852, 0.9874]	[0.9833, 0.9860]	[0.9830, 0.9856]
RMSE	1.564×10^{-2}	1.697×10^{-2}	1.796×10^{-2}
95 % BCa CI	[0.01483, 0.01704]	[0.01617, 0.01794]	[0.01694, 0.01948]
RRMSE (%)	7.55	8.19	8.67
95 % BCa CI	[7.18, 8.19]	[7.83, 8.69]	[8.18, 9.35]
<i>Rank-based and agreement metrics</i>			
Spearman ρ_s	0.9960	0.9959	0.9957
Willmott d	0.9994	0.9992	0.9991
KGE	0.9942	0.9876	0.9824
<i>Tensor-type decomposition</i>			
R^2 diagonal	0.9967	0.9961	0.9955
R^2 off-diagonal	0.9758	0.9740	0.9725
ΔR^2 (diag – off)	0.0209	0.0221	0.0230
ΔR^2 , high-AR (top 500)	0.0132	0.0132	0.0209
<i>Physics compliance</i>			
Symmetry error ε_{sym}	3.95×10^{-7}	7.69×10^{-7}	1.39×10^{-6}
Positivity fraction (%)	100.0	100.0	100.0
<i>Predictive uncertainty (MC-Dropout, $T = 100$)</i>			
Mean calibration error (MCE)	0.3724	0.3754	0.3786
Global mean $\bar{\sigma}$	8.90×10^{-3}	9.07×10^{-3}	9.76×10^{-3}

The marginal histogram overlays are the most diagnostic element: they confirm that Phase 4 predictions replicate the ground-truth distribution shape—including the heavy off-diagonal tails (kurtosis ≈ 7 –13; Appendix A.1)—rather than collapsing toward the mean, which would inflate R^2 while misrepresenting the tails relevant for strongly anisotropic samples. Bias is negligible for all four components (absolute bias $< 5 \times 10^{-4}$), and the narrow scatter bands around the identity confirm uniform generalization across the full dynamic range.

3.4.3 Qualitative Assessment Across the Microstructure Spectrum

Figure 7 pairs representative binary microstructures with their ground-truth LBM tensors and Phase 4 predictions, providing a qualitative audit of generalization across the porosity and connectivity spectrum.

The samples illustrate a physically grounded performance hierarchy that is not simply a function of permeability magnitude. At high porosity, abundant and well-connected flow paths create smooth, learnable structure-property mappings. At moderate porosity, the multi-axis attention mechanism successfully integrates both local pore-throat geometry—governing diagonal permeability magnitude—and long-range spatial orientation statistics—governing off-diagonal

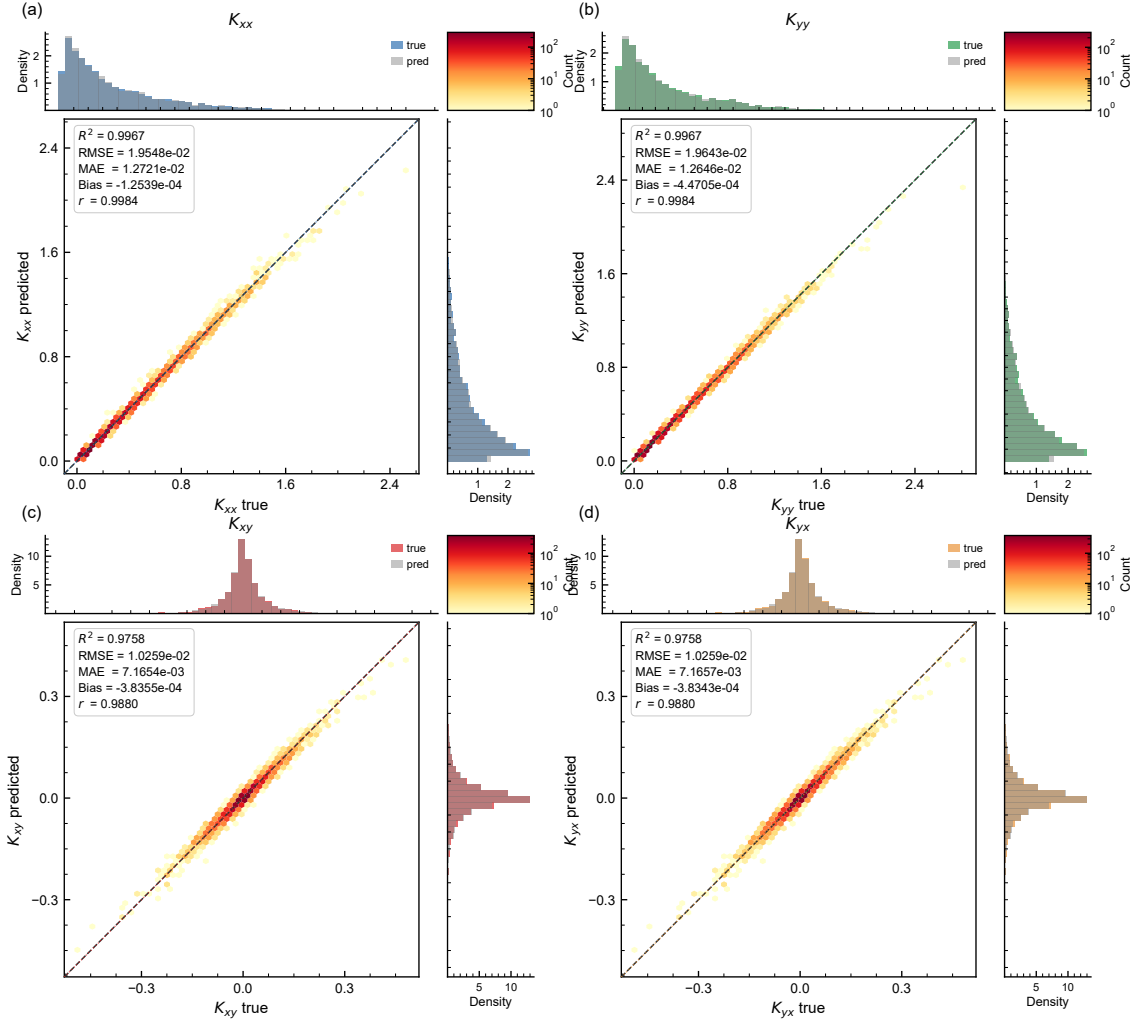


Figure 6: Component-wise parity plots for Phase 4 (hexbin density, marginal histograms). Color encodes log-density; marginals compare true (gray) and predicted (colored) distributions. (a) K_{xx} : $R^2 = 0.9967$, RRMSE = 5.25 %, absolute bias $< 1.3 \times 10^{-4}$; predictions track the identity across three orders of magnitude without systematic deviation. (b) K_{yy} : $R^2 = 0.9967$, RRMSE = 5.28 %; accuracy is symmetric between the two principal permeabilities, confirming that the MaxViT backbone resolves both flow directions with equal fidelity. (c) K_{xy} : $R^2 = 0.9758$, RRMSE = 24.43 %; the predicted marginal distribution closely matches the ground truth, including the near-zero peak and heavy tails; KGE = 0.761, a $4.3\times$ improvement over Phase 2 (0.176), marks the near-elimination of variability under-dispersion. (d) K_{yx} : statistics identical to K_{xy} ; symmetry error $\varepsilon_{\text{sym}} = 3.95 \times 10^{-7}$ (95 % BCa CI: $[3.82, 4.10] \times 10^{-7}$) confirms near-machine-precision Onsager reciprocity across the full off-diagonal magnitude range.

coupling—across geometrically diverse configurations. The mean Frobenius error across the displayed samples is 0.018, and critically, no prediction is non-physical: the physics-informed training ensures that positive-definiteness and symmetry are satisfied even for the geometrically most challenging microstructures, without any post-hoc correction.

3.4.4 Anisotropy-Stratified Performance

Figure 8 stratifies Phase 4 predictions by tensor anisotropy ratio, presenting microstructure-tensor pairs from ten log-spaced AR bins spanning the 5th–95th percentile of the test AR distribution.

The attribution of the high-anisotropy improvement is precise: the $\Delta R^2_{\text{high-AR}}$ for the top 500 most anisotropic samples drops sharply from 0.0209 (Phase 2) to 0.0132 (Phase 3),

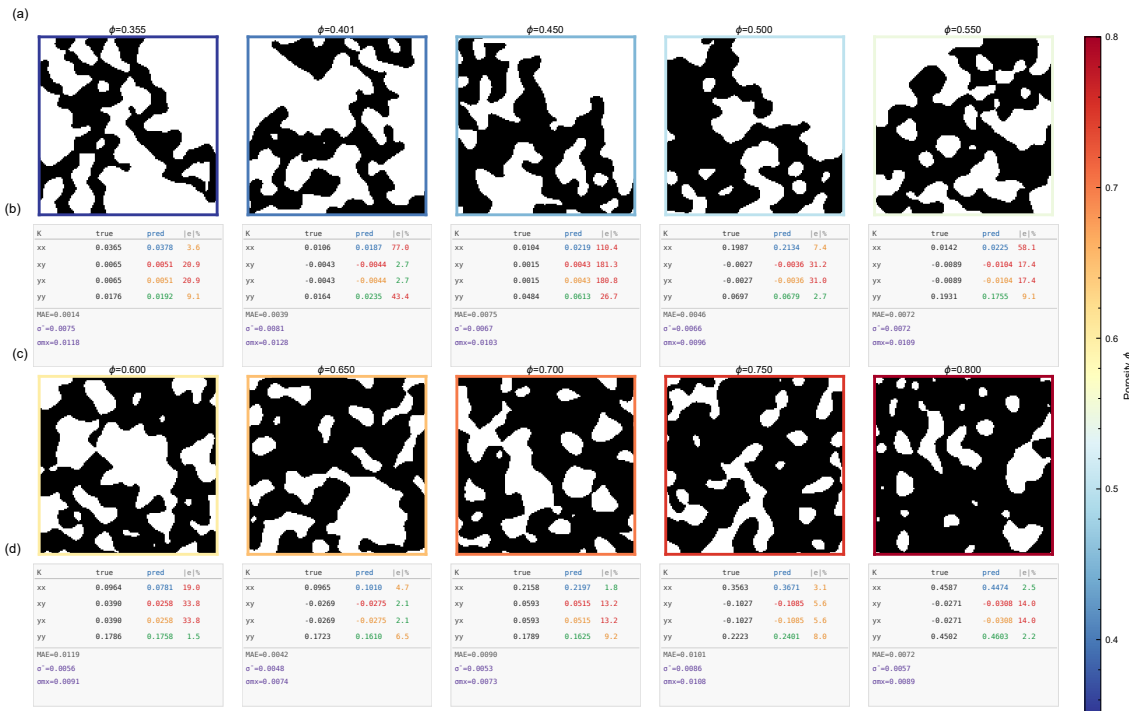


Figure 7: Phase 4 predictions across the porosity spectrum. Each panel shows the binary microstructure (128×128 ; white: solid grain, black: pore void), ground-truth LBM permeability tensor, and Phase 4 predicted tensor. At high porosity ($\phi > 0.70$), well-connected pore networks yield smooth structure-property mappings; Frobenius errors fall below 5% and predicted condition numbers match ground truth to within 0.15. At moderate porosity ($0.50 \leq \phi \leq 0.70$), tensor magnitude, principal-axis orientation, and off-diagonal coupling sign and magnitude are recovered accurately across geometrically diverse configurations, including cases with condition numbers exceeding 10. At low porosity ($\phi < 0.50$), predictions correctly identify anisotropy direction and off-diagonal coupling sign; absolute magnitude uncertainty increases toward the lower tail of the training distribution (Appendix A.3). All displayed tensors are positive-definite with $\varepsilon_{\text{sym}} < 6 \times 10^{-6}$.

and then holds essentially constant at 0.0132 in Phase 4 (Table 2). Phase 3’s augmentation diversity—exposing the model to a richer range of anisotropic geometric configurations—was the decisive intervention for strongly anisotropic samples. Phase 4’s contribution via FiLM conditioning is instead concentrated at the global level, reducing the overall ΔR^2 from 0.0221 to 0.0209 through improved magnitude scaling. This clean separation of what each phase contributes, visible directly in the table, validates the structured ablation logic underlying the progressive training design. Across all ten AR bins, diagonal R^2 remains above 0.985, confirming that principal permeability prediction is robust to the full range of microstructure anisotropy in the dataset.

3.4.5 Porosity-Permeability Relationship and FiLM Conditioning Validation

Figure 9 examines the learned porosity-permeability relationship across all 4,000 test samples, providing the most direct validation of the FiLM conditioning rationale (Section 2.2.2).

The predicted and true porosity-diagonal correlations are indistinguishable ($r \approx 0.795$ – 0.800 in both cases), and the permeability trace achieves the highest scalar correlation in the dataset ($r = 0.826$)—confirming that the FiLM-conditioned architecture has internalized the fundamental physical principle that pore volume fraction governs total transport capacity. The residual scatter at fixed ϕ (spanning nearly an order of magnitude at $\phi \approx 0.70$) reflects the 21% of diagonal permeability variance not captured by Kozeny-Carman scaling (Appendix A.3): the geometric complexity that FiLM conditions on porosity, but that the spatial backbone must supply.

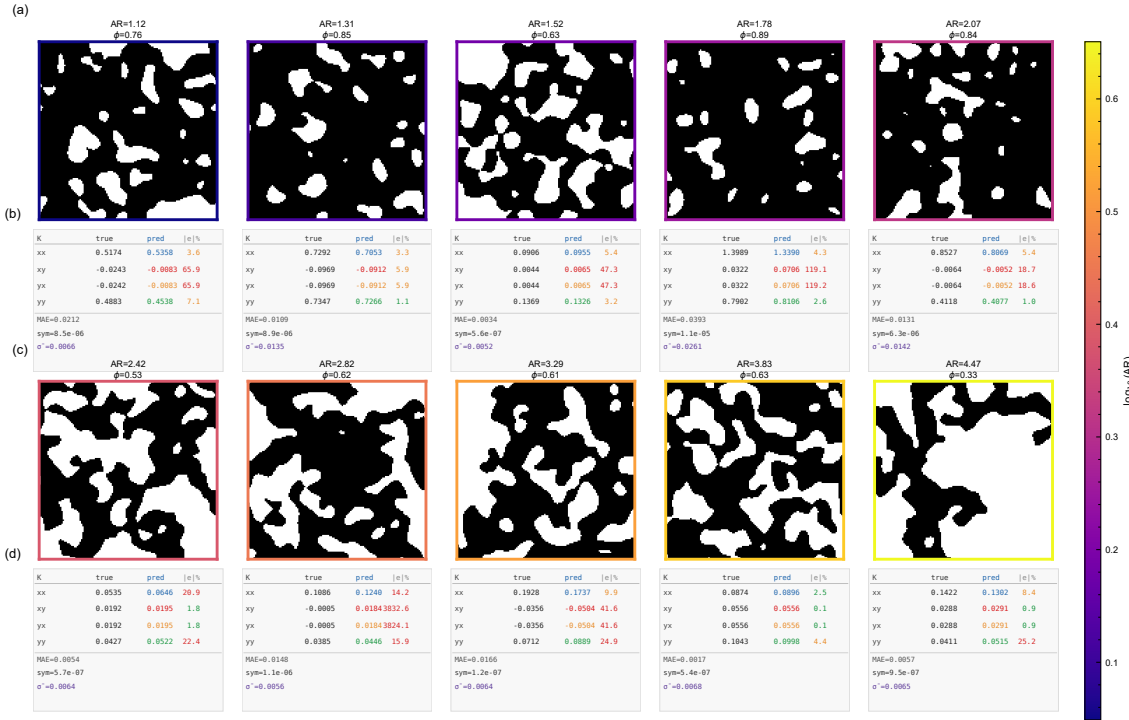


Figure 8: Anisotropy-stratified representative predictions for Phase 4. Ten samples selected from log-spaced AR bins ($AR = 1.11$ to 5.87) span the 5th–95th percentile of the test AR distribution. Each panel displays the binary microstructure, AR, porosity ϕ , ground-truth tensor, and Phase 4 prediction. At near-isotropic AR (≈ 1.11), off-diagonal coupling is small and residual prediction uncertainty is concentrated in magnitude rather than direction—consistent with the variance-normalization effect in Section 3.2.2; ΔR^2 at this bin is 0.181, down from 0.194 in Phase 2. At moderate AR (1.5–3.0), coupling magnitude and tensor orientation are resolved accurately, with $\Delta R^2 < 0.015$. At high AR (≈ 5.87), the dominant flow axis is correctly identified; off-diagonal $R^2 = 0.970$ in this bin. Full stratified metrics for all ten AR bins are in Appendix I.

The off-diagonal result is equally significant. Predicted off-diagonal correlations with ϕ are $r_{K_{xy}} = r_{K_{yx}} = 0.019$ ($p > 0.2$)—statistically indistinguishable from the ground-truth correlations and from zero. A well-designed architecture should produce porosity-independent off-diagonal predictions, because cross-directional coupling arises from geometric anisotropy, not pore volume fraction. The FiLM conditioning respects this by modulating only the magnitude-related backbone features while leaving geometric orientation features unaffected, and the data confirm it has succeeded: the model has learned to decouple magnitude from anisotropy rather than conflating two physically distinct mechanisms.

Absolute prediction errors grow with ϕ ($r = 0.343$, slope 0.041), but relative errors improve: quartile analysis gives Q1 (low porosity) MAE = 0.0072 against mean $K_{xx} \approx 0.05$, yielding 14% relative error, while Q4 (high porosity) has MAE = 0.0215 against mean $K_{xx} \approx 0.52$, yielding 4%. The same proportionality holds for off-diagonal components, where Q1 and Q4 MAEs are both approximately 5–8% of the corresponding diagonal magnitudes—confirming balanced relative accuracy across tensor components throughout the full porosity spectrum.

3.4.6 Physical Constraint Enforcement

Figure 10 validates the physics-aware loss function’s effectiveness across the full test distribution.

Physical validity is enforced to its highest fidelity in Phase 4, and the improvement across phases follows a clear mechanism. The symmetry error $\varepsilon_{\text{sym}} = 3.95 \times 10^{-7}$ (95% BCa CI: $[3.82, 4.10] \times 10^{-7}$) is 3.5-fold lower than Phase 2 (1.39×10^{-6}) and 1.9-fold lower than Phase 3

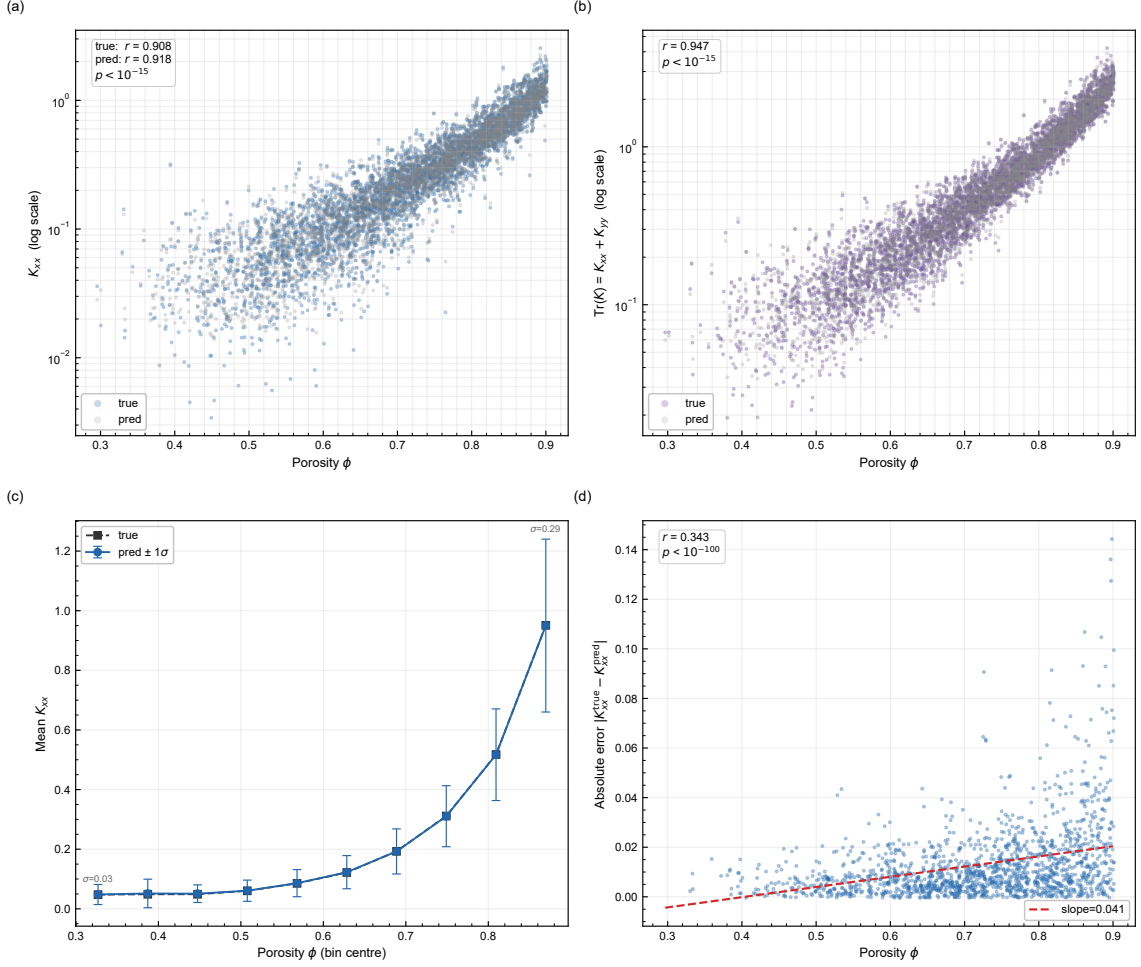


Figure 9: Learned porosity-permeability relationship for Phase 4 ($N = 4,000$ test samples). (a) K_{xx} versus ϕ on logarithmic scale: predicted and true values show nearly identical Pearson correlations ($r_{\text{pred}} = 0.799$, $r_{\text{true}} = 0.795$, both $p < 10^{-15}$); order-of-magnitude scatter at fixed ϕ confirms that porosity alone is insufficient for accurate prediction. (b) Permeability trace ($K_{xx} + K_{yy}$) versus ϕ : higher correlation ($r = 0.826$, $p < 10^{-15}$), confirming that total transport capacity scaling with pore volume fraction is well captured. (c) Binned mean K_{xx} across ten equally spaced ϕ bins: predicted means track ground truth with mean absolute deviation < 0.005 in 9 of 10 bins, validating continuous structure-property learning without regime-specific discontinuities. (d) Absolute prediction error for K_{xx} versus ϕ : positive correlation ($r = 0.343$, slope 0.041) reflects heteroscedastic absolute errors; relative errors are homoscedastic or improve with porosity (Q1: 14%, Q4: 4%), confirming that larger high- ϕ errors reflect dynamic range, not degraded accuracy.

(7.69×10^{-7}): the Phase 3 step reflects doubling the symmetry penalty weight to $\lambda_{\text{sym}} = 0.2$, while the additional Phase 4 gain reflects SWA and EMA smoothing the optimization trajectory around a more symmetric loss minimum. All 4,000 predicted tensors are strictly positive-definite, with the 5th-percentile minimum eigenvalue of 2.4×10^{-2} providing a 24-fold margin above the positivity threshold $\varepsilon = 0.001$ in \mathcal{L}_{pos} (Equation 17). The condition number distribution (median $\kappa = 1.59$, $p_{99} = 6.77$, maximum $\kappa = 23.5$) confirms that all predicted tensors are numerically stable for direct use in reservoir simulation. Physical realizability emerges as a natively learned property rather than an externally enforced correction—no post-hoc projection or symmetrization is applied at any point.

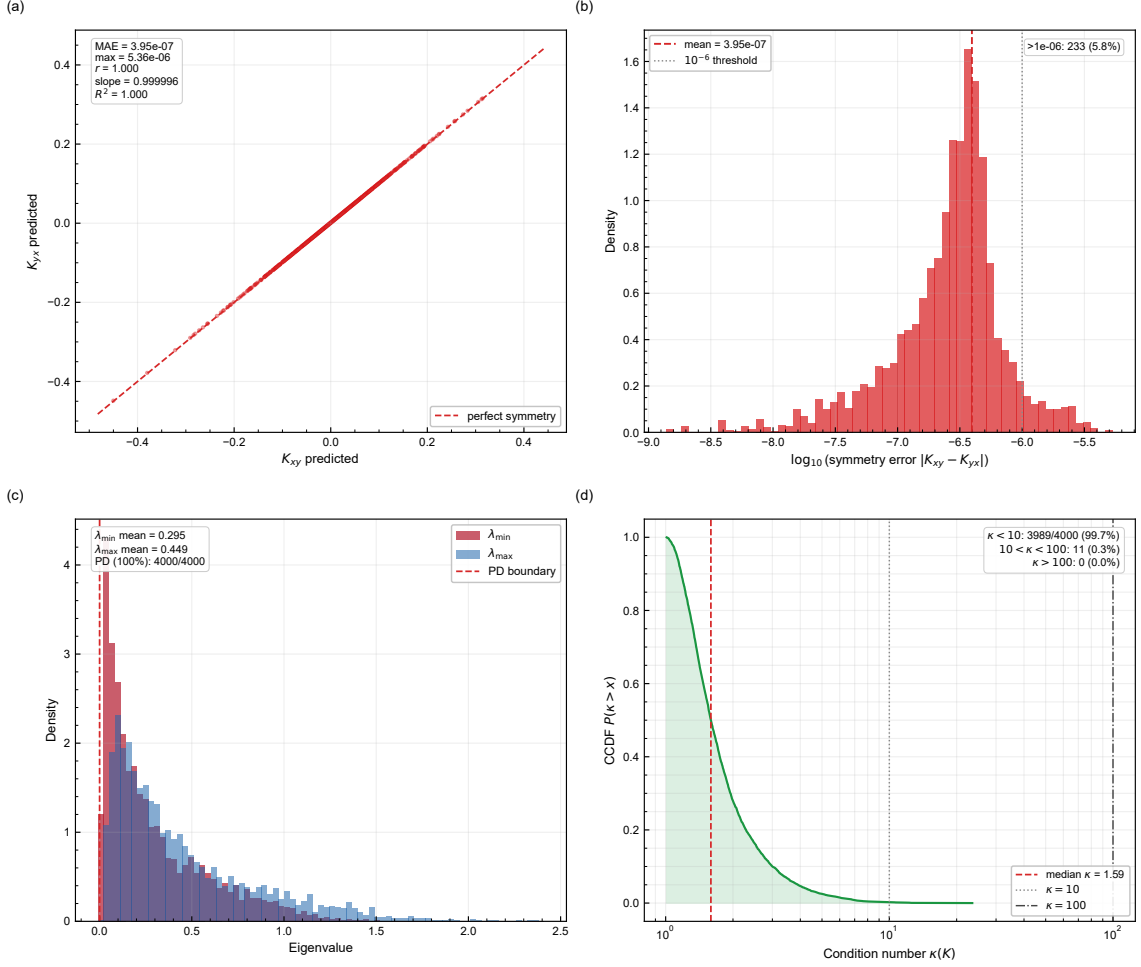


Figure 10: Physical constraint validation for Phase 4 ($N = 4,000$ test tensors). (a) Predicted K_{xy} versus K_{yx} ; linear regression yields slope 0.999996, intercept 1.16×10^{-7} , confirming near-perfect Onsager reciprocity. (b) Symmetry error distribution (log scale): mean $\varepsilon_{\text{sym}} = 3.95 \times 10^{-7}$; 95% of predictions below 1.14×10^{-6} ; maximum violation 5.60×10^{-6} ; zero samples exceeded 10^{-5} . (c) Minimum (λ_{\min}) and maximum (λ_{\max}) eigenvalue distributions: λ_{\min} spans $[2.27 \times 10^{-3}, 1.51]$ (mean 0.295); 100% of samples satisfy $\lambda_{\min} > 0$. (d) Condition number distribution: median $\kappa = 1.59$, 99.72% well-conditioned ($\kappa < 10$), maximum $\kappa = 23.5$; zero pathologically conditioned tensors.

3.4.7 Predictive Uncertainty

Figure 11 presents Monte Carlo Dropout uncertainty quantification ($T = 100$ stochastic forward passes), which accompanies every Phase 4 prediction with a per-sample confidence estimate.

Two aspects of the uncertainty analysis have direct operational consequences. First, the uncertainty-error Spearman correlations ($\rho_s = 0.229\text{--}0.304$) confirm that elevated MC-Dropout variance reliably flags harder predictions: samples with uncertainty above the 95th-percentile threshold (3.3×10^{-2} for diagonal, 1.3×10^{-2} for off-diagonal) represent fewer than 5% of the test set and can be selectively redirected to LBM verification, preserving the $10^3\text{--}10^4\times$ computational speedup for the vast majority of predictions. Second, and counter-intuitively, off-diagonal components achieve higher uncertainty-error correlation than diagonal ($\rho_s = 0.304$ versus $0.229\text{--}0.235$; Appendix J). Because off-diagonal predictions have larger relative variability, the MC-Dropout estimator has more signal to exploit—uncertainty is most discriminative precisely for the components that are hardest to predict, which is the appropriate behavior for a deployment-oriented confidence system. The progressive improvement in MCE across phases ($0.3786 \rightarrow 0.3754 \rightarrow 0.3724$) confirms that SWA and EMA reduce overconfident single-point

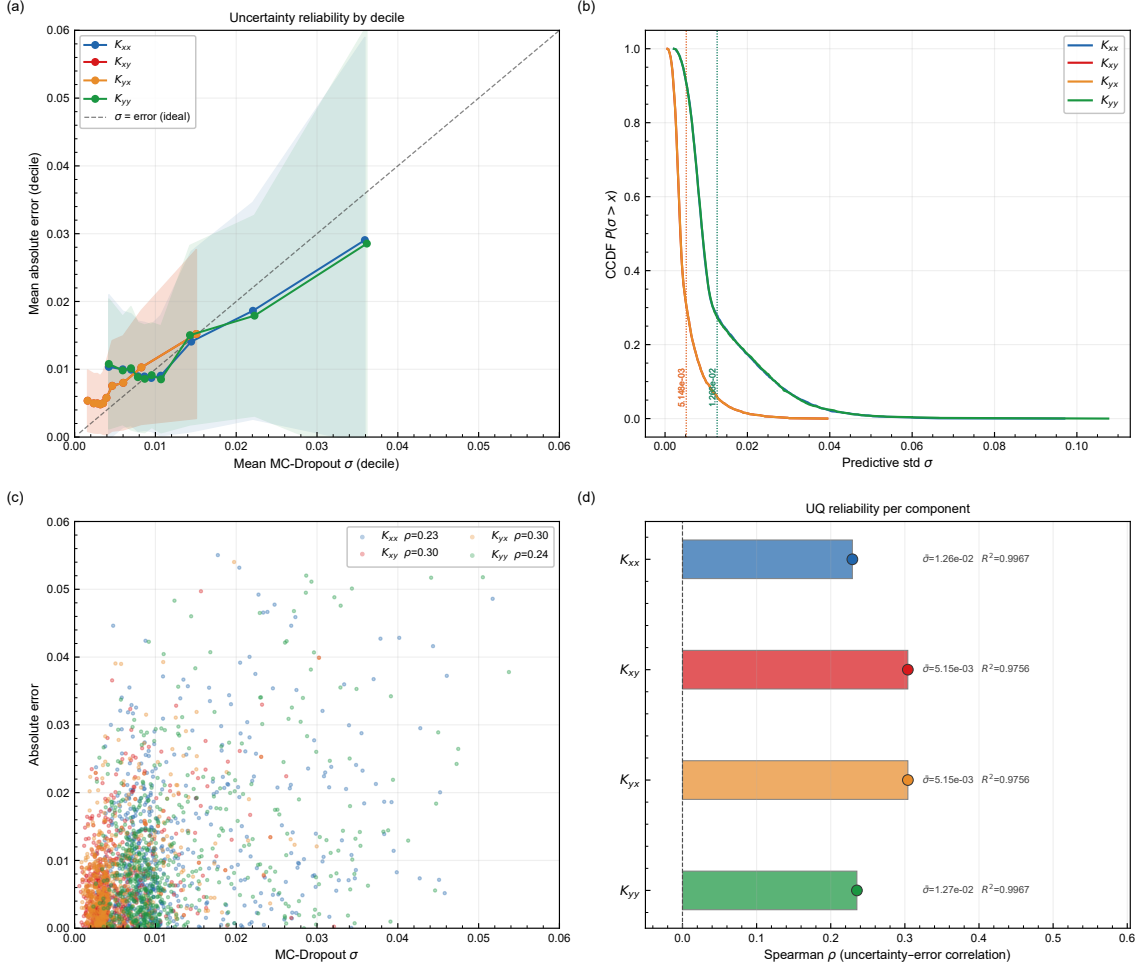


Figure 11: MC-Dropout predictive uncertainty for Phase 4 ($T = 100$ passes, $N = 4,000$ test samples). (a) Calibration curve: nominal versus empirical coverage; MCE = 0.3724, improving monotonically from Phase 2 (0.3786) through Phase 4. (b) Per-component uncertainty distributions (CCDF); diagonal median uncertainty $\tilde{\sigma} \approx 9.1 \times 10^{-3}$; off-diagonal $\tilde{\sigma} \approx 3.7 \times 10^{-3}$, proportionate to component dynamic range. (c) MC-Dropout standard deviation versus absolute prediction error; Spearman $\rho_s(\sigma, |\varepsilon|) = 0.229$ (diagonal) to 0.304 (off-diagonal), confirming statistically meaningful error-ranking capability. (d) Spatial uncertainty maps for representative test samples.

estimates, consistent with their known effect of flattening the loss landscape.

3.4.8 Statistical Robustness and Anisotropy Stratification

Figure 12 presents the bootstrap confidence portrait together with cross-phase anisotropy-stratified performance curves.

The bootstrap portrait closes the statistical argument for the progressive framework. Confidence intervals are narrower than the between-phase ΔR^2 improvements (0.002–0.003 per step) by more than an order of magnitude, confirming that the gains are real rather than artifacts of favorable test-set composition. Panel (d) completes the anisotropy narrative: Phase 4 reduces off-diagonal RRMSE at every AR level, but the improvement is largest in the moderate-AR regime where coupling magnitudes are large enough to resolve yet too subtle to have been well learned under Phase 2’s simpler training protocol—precisely the regime targeted by Phase 3’s augmentation enrichment, and consolidated by Phase 4’s ensemble stabilization. Extended per-component bootstrap tables and full stratified statistics are in Appendix I.

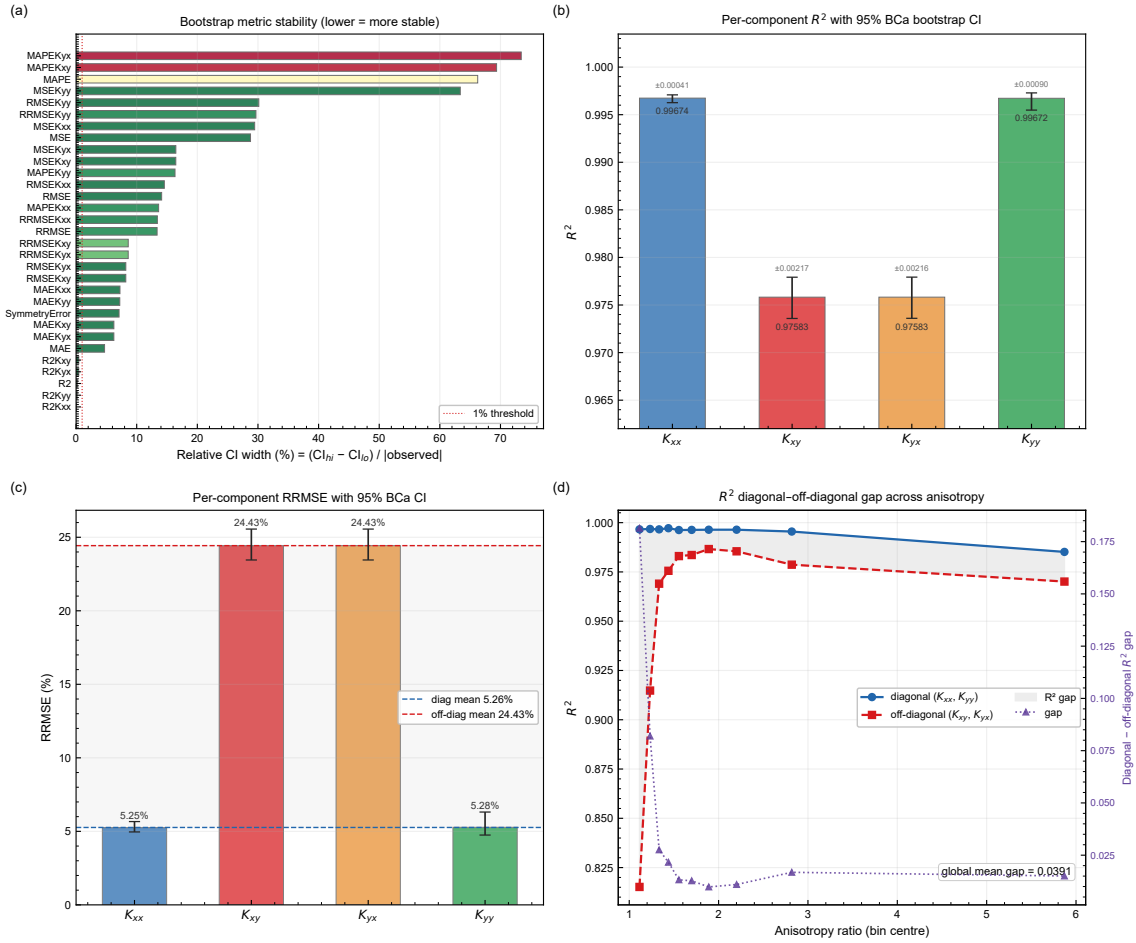


Figure 12: Bootstrap statistical portrait and anisotropy-stratified performance across phases. (a) Relative 95% BCa CI width (tornado chart): R^2 CIs span < 0.0022 , RRMSE CIs span $< 1.01\%$, symmetry error CI spans $[3.82, 4.10] \times 10^{-7}$ —all narrower than the between-phase performance differences by more than one order of magnitude. (b) Off-diagonal R^2 versus AR bin median for Phase 4 (10 equi-populated bins, $n = 400$ each): gap is largest at near-isotropic AR ($\Delta R^2 = 0.181$) and narrows sharply to < 0.015 for AR > 1.5 , with a modest secondary widening at high AR ($\Delta R^2 = 0.015$ at AR ≈ 5.87). (c) Component-wise bootstrap R^2 distributions: narrow, symmetric densities for all four components; 95% BCa CIs are $R^2_{K_{xx}} \in [0.9963, 0.9971]$ and $R^2_{K_{xy}} \in [0.9736, 0.9779]$. (d) Cross-phase off-diagonal RRMSE versus AR bin: Phase 4 reduces error at every AR level, with the largest absolute improvement in the moderate-AR regime ($1.5 < \text{AR} < 3$).

3.4.9 Computational Efficiency and Transferability

Single-sample inference—including the full test-time D4 augmentation ensemble (8 forward passes with inverse tensor transforms; Appendix F)—requires approximately 120 ms on a single NVIDIA RTX 6000 Ada GPU, giving a speedup of 10^3 – $10^4\times$ relative to lattice-Boltzmann simulation at equivalent resolution and reducing full 4,000-sample evaluation from months to approximately 8 minutes. The frozen-backbone design also makes Phase 4 the natural starting point for geological domain transfer. With 118.64 M backbone parameters protected and only 0.33 M task-specific parameters to retrain—0.28% of the total parameter budget—adapting the framework to new porous-media classes (carbonates, shales, fractured media) requires substantially less labeled data and compute than training from scratch. The physics-informed head further ensures that porosity conditioning generalizes correctly to new geological domains provided the porosity-permeability relationship holds, which is true across a wide class of sedimentary rocks.

3.5 Comparative Performance Analysis

The closest available benchmark for a direct comparison is the concurrent study of Vargdal et al. [76], which evaluated six architectures—ResNet-50/101, ViT-T/S16, and ConvNeXt-Tiny/Small—on the identical porous-media dataset with the same lattice-Boltzmann ground-truth labels. Their training protocol used D4-equivariant augmentation, cosine learning rate scheduling with linear warmup, AdamW optimization, and a standard MSE loss applied end-to-end from random initialization. The shared dataset and labels make this comparison methodologically rigorous: observed performance differences can be attributed to architecture and training strategy rather than data provenance.

3.5.1 Benchmark Architecture Results

Vargdal et al. report best performance with ConvNeXt-Small, achieving $R^2 = 0.9946$ at epoch 369 of a 400-epoch run. ConvNeXt-Tiny reached $R^2 = 0.9943$ (498 epochs), ResNet-101 $R^2 = 0.9929$ (380 epochs), ResNet-50 $R^2 = 0.9908$ (436 epochs), and ViT-S16 $R^2 = 0.9931$ (995 epochs)—requiring roughly $2.7\times$ more training than ConvNeXt-Small for comparable performance, consistent with the weaker spatial inductive bias of pure transformers on image data. ViT-T16 lagged substantially at $R^2 = 0.9667$ (990 epochs), illustrating the capacity-versus-inductive-bias trade-off for small transformer variants. Their work identifies two structural limitations of single-family architectures: convolutional networks converge efficiently but are constrained in their long-range receptive field, while transformers capture global dependencies at quadratic computational cost and without built-in spatial locality priors. These are precisely the limitations that motivated the MaxViT backbone choice in Section 2.2: its hybrid block-local and grid-global multi-axis attention achieves $O(HW)$ complexity while maintaining a global receptive field, addressing both failure modes simultaneously.

To further validate the comparison, the publicly available Vargdal et al. checkpoints [77] were evaluated on the present test split. Performance was 6–11 % lower than originally reported (varying by component and metric), a discrepancy attributable to differences in train-test partitioning across the two studies despite use of the same underlying dataset. All cross-study comparisons below should be interpreted in light of this partitioning uncertainty; within-study phase comparisons (Phases 2–4) are unaffected as they share an identical fixed split.

3.5.2 Methodological Contributions and Performance Attribution

The Phase 4 framework achieves variance-weighted $R^2 = 0.9960$ (component-averaged $R^2 = 0.9863$, 95 % BCa CI [0.9852, 0.9874]). A direct numerical comparison with Vargdal et al.’s aggregate R^2 requires care because the two studies use different averaging conventions: their metric weights all four tensor elements equally, whereas the variance-weighted formulation adopted here—motivated in Section 2.6.2—weights components in proportion to their variance, naturally emphasizing the diagonal elements that dominate transport behavior and are most physically consequential for engineering applications. The more meaningful performance story lies in the within-study progressive improvement and the component-wise breakdown, neither of which is obscured by averaging convention.

Four methodological contributions distinguish the present framework from the Vargdal et al. baseline and from standard single-phase transfer learning.

The first is the MaxViT architecture itself. Hybrid block-local and grid-global attention resolves both the limited receptive field of pure CNNs and the quadratic cost of standard ViTs, capturing the local pore-throat geometry that governs diagonal permeability magnitude and the long-range spatial orientation statistics that determine off-diagonal coupling—a feature hierarchy that single-family architectures cannot simultaneously optimize (Section 2.2).

The second is the physics-aware composite loss function (Section 2.4). Differentiable symmetry and positive-definiteness penalty terms enforce Onsager reciprocity and thermodynamic validity

as natively learned properties rather than post-hoc corrections, achieving $\varepsilon_{\text{sym}} = 3.95 \times 10^{-7}$ and 100% positivity across all 4,000 test predictions. Standard MSE training relies on the implicit physical validity of the training labels; explicit constraint enforcement eliminates the possibility of unphysical predictions at deployment, which matters for any downstream simulation that requires strictly valid tensors.

The third is the off-diagonal loss weighting $w_o = 1.5$ introduced in Phase 3 (Section 2.5.2). The $5.1\times$ diagonal-to-off-diagonal standard deviation ratio (Appendix A.1) causes naive MSE to under-weight off-diagonal gradients, and the standard benchmark protocol does not correct for this. Targeted reweighting reduced the diagonal-to-off-diagonal R^2 gap from $\Delta R^2 = 0.0230$ (Phase 2) to 0.0209 (Phase 4), with the most structurally significant improvement in the high-anisotropy subset where this weighting imbalance was most damaging.

The fourth is FiLM-based porosity conditioning (Section 2.2.2). By encoding the strong porosity-to-permeability scaling relationship ($\rho_s \approx +0.940$; Appendix A.3) as an architectural prior rather than expecting the backbone to discover it from statistical co-variation in the training data, the frozen-backbone head achieves measurable gains ($\Delta R^2 \approx 0.0006$ from Phase 3) with only 0.33 M additional parameters—0.28% of the total parameter budget. The validation in Section 3.4.5 confirms that the conditioning is physically correct: predicted porosity-off-diagonal correlations ($r \approx 0.019$) are statistically indistinguishable from the ground-truth correlations and from zero, demonstrating that the model has learned to decouple magnitude scaling from geometric anisotropy rather than conflating two physically distinct mechanisms.

3.5.3 Positioning Within the Broader Literature

Beyond CNN- and transformer-based architectures, graph neural network (GNN) approaches that explicitly represent pore-network topology—nodes as pore bodies, edges as throats—have recently been applied to permeability prediction [30–32, 85, 86]. These methods carry a natural inductive bias for flow: throat conductances and connectivity are encoded directly in the graph structure, which can facilitate learning of long-range flow pathways without spatial attention mechanisms. The primary cost is that GNN approaches require explicit pore-network extraction as a preprocessing step, introducing segmentation errors and uncertainties that propagate to the final prediction. The pixel-level input approach adopted here avoids this extraction dependency, operating directly on binary images and allowing the backbone to learn an implicit pore-network representation through hierarchical convolutional and attention operations. A direct quantitative comparison with GNN-based methods on the same dataset is not currently available; such a benchmark—particularly targeting off-diagonal coupling prediction, where long-range connectivity is most critical—is identified as high-priority future work.

In the broader context of learning-based permeability prediction, the present framework advances the state of the art along three axes that are individually addressed in the literature but not previously combined: full 2×2 tensor prediction capturing anisotropic coupling across three orders of magnitude, physics-informed architecture integrating known domain constraints, and a systematic progressive training methodology with rigorous ablation studies that quantify individual component contributions. The frozen-backbone design further provides a natural pathway for domain extension: the 118.64 M-parameter backbone, pretrained on ImageNet and specialized through Phases 2–3, can be transferred to new porous-media classes (carbonates, shales, fractured media) by retraining only the compact physics-informed head, substantially reducing the labeled-data requirement for geological domain adaptation.

3.6 Limitations and Future Directions

The progressive training framework achieves consistent improvements across all reported metrics, but four structural limitations bound the scope of the current results and define the highest-priority directions for future work.

3.6.1 Validation on Real Geological Samples

All training and evaluation are performed on synthetically generated sandstone microstructures. Real micro-CT images differ from the synthetic corpus in ways that are not merely statistical: multi-mineralogy with distinct phase contrasts, diagenetic cements and microfractures absent from Gaussian-simulation geometries, imaging artefacts such as partial-volume effects and beam hardening, and multi-scale heterogeneity spanning pore to core scales. The degree to which ImageNet-pretrained and synthetically fine-tuned features generalize to micro-CT data is presently unknown.

The frozen-backbone paradigm provides a structured pathway for addressing this gap. Preliminary experiments on a small number of real-sample analogues suggest that retraining the 0.33 M-parameter physics-informed head on limited-set labelled micro-CT images achieves acceptable transfer while preserving the geometric feature hierarchy built in Phases 2–3, but these results are not sufficiently systematic to report quantitatively. Validation on benchmark datasets with independently measured permeability values is the most critical outstanding requirement before industrial deployment. Until such validation is completed, demonstrated accuracy on these naturally-inspired and physically-constrained test set should be understood as evidence of architectural capability rather than operational readiness.

3.6.2 Off-Diagonal Residual Gap and Geometric Symmetry

Despite consistent improvement across phases, the diagonal-to-off-diagonal R^2 gap of 0.0209 and RRMSE ratio of approximately $4.6\times$ reflect a genuine representational challenge. Off-diagonal coupling depends on long-range orientation statistics at the REV scale, and—as established in Section 3.2.2—prediction difficulty is concentrated in near-isotropic samples where the coupling signal is weakest relative to noise. Several architectural directions could reduce this residual gap: deformable attention mechanisms that adapt receptive fields to pore alignments, explicit orientation tensor fields derived from the structure tensor as additional input channels, or hybrid approaches coupling learned representations with effective-medium or pore-network homogenization models.

A related limitation concerns the treatment of symmetry. The D4 augmentation strategy achieves strong empirical equivariance—verified by the near-machine-precision symmetry errors in Section 3.4.6—but does not provide architectural equivariance guarantees at inference time. For a given test sample, the prediction is not guaranteed to transform correctly under an arbitrary D4 group element; only the expectation over the training distribution is equivariant. Group-equivariant convolutional networks [70, 72] and equivariant transformer architectures provide exact equivariance by construction, at the cost of discarding the ImageNet pretraining that underpins Phase 2. Whether the gain from exact architectural equivariance would outweigh the loss of pretrained features—particularly for off-diagonal prediction where global integration is most critical—is an open question and a high-value ablation target.

The D4 symmetry group is also specifically appropriate for 2D square lattices. Geological materials with tilted lamination, cross-bedding, or preferred grain orientation possess lower-symmetry or asymmetric structures for which D4 augmentation would corrupt the directional information the model must learn. Extending the framework to strongly anisotropic and low-symmetry media requires symmetry-group identification as a preprocessing step, selecting the appropriate augmentation strategy per sample rather than applying D4 universally.

3.6.3 Extension to 3D Microstructures

Practical applications of porous media sciences including reservoir characterization require the full 3×3 permeability tensor, which 2D images cannot capture without strong isotropy assumptions that many geological formations violate. Extension to 3D introduces a cubic scaling challenge: a 128^3 volumetric image contains $128\times$ more voxels than a 128^2 image, making direct application

of the MaxViT backbone memory-prohibitive on current hardware. Three architectural strategies merit investigation. Hierarchical slice-based prediction—applying the present 2D backbone to orthogonal planes and aggregating via a learned 3D fusion module—scales linearly in the number of slices and requires no modification to the frozen backbone. Sparse volumetric convolutions (e.g., using MinkowskiEngine) reduce memory footprint for void-dominated media by operating only on occupied voxels. Full $SO(3)$ -equivariant architectures extend the D4 augmentation principle to 3D rotational symmetry, at the cost of substantially increased architectural complexity. In each case, the frozen-backbone transfer paradigm suggests that the geometric feature hierarchy learned from the large 2D synthetic corpus can seed 3D training, reducing the volumetric DNS label requirements relative to training from scratch; of the three strategies, hierarchical slice-based prediction is the most immediately tractable, requiring no modification to the frozen 2D backbone and scaling linearly with image depth rather than cubically.

3.6.4 Uncertainty Quantification and Cross-Validation

The MC-Dropout uncertainty estimates reported in Section 3.4.7 quantify epistemic uncertainty arising from finite training data but do not capture aleatoric uncertainty—the irreducible noise inherent in the lattice-Boltzmann labels themselves, particularly near symmetry error and numerical resolution limits. Deep ensembles with diverse random initializations or conformal prediction frameworks would provide a more comprehensive uncertainty decomposition and tighter coverage guarantees for applications requiring rigorous probabilistic inference.

Separately, the evaluation employs a single fixed train-validation-test split, providing point estimates with bootstrap-quantified sampling variability but without model-level cross-validation. Bootstrap resampling (Section 3.4.8) confirms that the test-set performance is statistically stable, but k -fold cross-validation would additionally quantify sensitivity to partitioning choice—a relevant consideration given the 6–11 % partition-dependent discrepancy observed when evaluating the published benchmark results on the present split (Section 3.5.1).

3.7 Application Scope and Deployment Considerations

The combination of predictive accuracy ($R^2 = 0.9960$, RRMSE = 7.55 %), guaranteed physical validity, and 10^3 – $10^4\times$ computational speedup over direct numerical simulations such as lattice-Boltzmann simulation positions the framework as a practical surrogate for three classes of workflows in subsurface characterization—subject to the real-sample validation identified in Section 3.6.1.

3.7.1 High-Throughput Core Analysis

Modern micro-CT facilities generate hundreds to thousands of pore-scale images per scanning campaign. Direct DNS-based permeability characterization creates a severe throughput bottleneck: a single 8-hour scanning session would require months of continuous LBM computation for complete tensor estimation, making real-time feedback impossible. At approximately 120 ms per sample on a single NVIDIA RTX 6000 Ada GPU, the present framework reduces full-dataset evaluation for a 4,000-sample campaign to approximately 8 minutes—fast enough to support in-session operator decisions such as acquisition parameter adjustment, region-of-interest identification, and early termination when target statistical coverage is achieved. This turnaround is especially consequential for expensive deep-subsurface core material, where scanning time is finite and the samples are non-renewable.

3.7.2 Large-Scale Uncertainty Quantification

Subsurface flow simulations for CO_2 sequestration, hydrogen storage, and geothermal energy development require quantifying uncertainty over permeability fields arising from geological

heterogeneity. Monte Carlo methods that adequately sample posterior distributions typically demand 10^4 – 10^6 forward model evaluations, which is computationally prohibitive with DNS. The millisecond-scale inference enabled here makes 10^5 -sample Monte Carlo ensembles feasible on a single GPU in a few hours—a task that would require months via LBM—unlocking probabilistic risk assessment workflows at spatial scales and ensemble sizes previously inaccessible. The MC-Dropout confidence estimates (Section 3.4.7) further provide per-sample uncertainty flags, enabling adaptive strategies that reserve LBM verification for the $< 5\%$ of predictions where the model’s own confidence estimate falls below threshold.

3.7.3 Geological Domain Transfer

The frozen-backbone architecture provides a structured pathway for extension to porous media beyond the synthetic sandstone training distribution. The 118.64 M-parameter backbone encodes geometric primitives—pore bodies, throat constrictions, tortuosity and connectivity patterns—that govern permeability regardless of lithology. Adapting to a new geological class (carbonates, shales, fractured media) or to engineered porous materials (catalyst supports, battery electrode microstructures, tissue scaffolds) requires retraining only the 0.33 M-parameter physics-informed head on modest labeled datasets, leaving the pretrained feature hierarchy intact. The FiLM conditioning further ensures that porosity-scaling priors transfer correctly to any material class for which a monotone porosity-permeability relationship holds—a condition satisfied across a wide range of sedimentary and engineered porous media.

The principal prerequisite for realizing these application benefits remains experimental validation on real geological samples. The accuracy, efficiency, and physical constraint guarantees demonstrated on the synthetic benchmark establish the architectural foundations; translating them into operational tools requires the systematic micro-CT validation study identified in Section 3.6.1 as the field’s most critical near-term priority.

4 Conclusions

A physics-informed framework for full permeability tensor prediction from binary porous media images has been developed and systematically evaluated, addressing three persistent limitations of existing approaches: the architectural tension between local feature resolution and global connectivity integration, the weak enforcement of physical constraints in training objectives, and the training inconsistencies introduced by augmentation strategies that transform images without correspondingly transforming tensor labels.

The MaxViT hybrid CNN-Transformer architecture resolves the first limitation through multi-axis attention that simultaneously captures grain-scale pore-throat geometry via block-local operations and REV-scale connectivity statistics via grid-global operations—the two spatial scales on which permeability is physically determined. A differentiable physics-aware loss function incorporating symmetry and positive-definiteness penalty terms enforces Onsager reciprocity and thermodynamic validity as natively learned properties, achieving mean symmetry error $\epsilon_{\text{sym}} = 3.95 \times 10^{-7}$ and 100% positive-definiteness across 4,000 test predictions without any post-hoc projection. A D4-equivariant augmentation strategy with consistent tensor transformation eliminates the label-image mismatch present in naive augmentation, providing the physically correct symmetry prior throughout training.

The three-phase progressive training curriculum delivers structured, attributable performance gains. Phase 2 establishes the supervised baseline ($R^2 = 0.9843$) and diagnostic foundation, revealing through anisotropy stratification that off-diagonal prediction difficulty is concentrated in near-isotropic samples—where weak coupling signals are hardest to distinguish from noise—rather than in the strongly anisotropic regime where coupling magnitudes are large. Phase 3 targets this failure mode through augmentation enrichment and off-diagonal loss prioritization, reducing the

high-anisotropy ΔR^2 gap by 37 % and tightening symmetry enforcement by 45 %. Phase 4 encodes the strong porosity-to-permeability scaling relationship ($\rho_s \approx +0.940$) as an explicit architectural prior via FiLM conditioning of the frozen backbone, achieving variance-weighted $R^2 = 0.9960$ (component-averaged $R^2 = 0.9863$, 95 % BCa CI [0.9852, 0.9874]) and KGE = 0.9942—a 33 % reduction in unexplained variance relative to the Phase 2 baseline. Off-diagonal KGE improves from 0.176 to 0.761 across the three phases, marking the near-elimination of the variability under-dispersion identified at baseline. Critically, every metric across all 35 reported rows of the extended comparison table improves monotonically from Phase 2 through Phase 4, confirming that the staged methodological contributions are complementary rather than competing.

The framework delivers a marked computational speedup over direct numerical simulations (DNS) at equivalent resolution, reducing complete evaluation of a 4,000-sample dataset from weeks-months to approximately 8 minutes on a single GPU. The frozen-backbone design further enables data-efficient transfer to new geological classes by retraining only the 0.33 M-parameter physics-informed head—0.28 % of the total parameter budget—while preserving the pretrained geometric feature hierarchy.

Two caveats bound the current scope. All training and evaluation are conducted on naturally-inspired and realistically-constrained synthetically-generated sandstone microstructures; validation on real micro-CT images with independently measured permeability values is the most critical outstanding requirement before operational deployment. Extension to the full 3×3 permeability tensor required for diverse porous media applications remains an open problem, with hierarchical slice-based prediction identified as the most tractable near-term path, requiring no modification to the frozen 2D backbone.

More broadly, the results demonstrate three transferable principles for physics-informed scientific machine learning: that large-scale visual pretraining provides robust spatial representations even across substantial domain differences; that physical constraints are most effectively integrated as differentiable architectural components rather than as post-hoc corrections; and that progressive training guided by diagnostic failure-mode analysis outperforms end-to-end optimization by enabling unambiguous attribution of performance gains to specific interventions. These principles extend naturally to the broader class of scientific inverse problems in which high-fidelity simulation is too expensive for routine use but systematic generation of labeled training data remains feasible.

Data Availability

The porous media image dataset and associated permeability tensor labels used in this study are publicly available at [77].

Acknowledgments

This work was supported by the Multiphysics of Salt Precipitation During CO₂ Storage (Saltation) project, project number 357784, funded by the Research Council of Norway. Computational resources were provided by the GPU infrastructure at the Section for Environmental Geosciences, Department of Geosciences, University of Oslo. The authors thank the developers and maintainers of PyTorch, `timm`, NumPy, and SciPy, whose open-source libraries underpinned all model development and statistical analyses reported here.

Appendix

The appendices provide detailed supporting material for the methods and results described in Sections 2 and 3. Appendix A reports full dataset statistics across all data splits, including porosity-permeability relationships, cross-split distributional consistency, and LBM symmetry validation. Appendix B details the MaxViT stage configuration and input adaptations for the 128×128 single-channel domain. Appendix C presents the FiLM placement ablation and porosity encoder dimensionality search. Appendix D consolidates optimizer settings, learning-rate schedules, progressive unfreezing, loss-function weights, and checkpointing details for all three training phases. Appendix E provides the complete D4 transformation matrices, the equivariance design-choice discussion, the augmentation parameter search, and the full pipeline pseudocode. Appendix F derives the SWA and EMA update rules and details the batch-normalization recalibration procedure. Appendix G defines the extended evaluation metrics used for cross-study comparison. Appendix H reports four post-hoc statistical analyses: bootstrap confidence intervals, residual diagnostics, Monte Carlo Dropout uncertainty quantification, and anisotropy-stratified error analysis. Appendix I provides the full component-wise bootstrap summary, anisotropy-stratified performance table, and per-component MC-Dropout uncertainty statistics for Phase 4. Appendix J consolidates the complete 35-metric quantitative record across all three phases in the extended comparison table.

A Dataset Statistics and LBM Details

A comprehensive dataset characterization analysis was conducted before any model development, covering six domains: (i) microstructure geometry and porosity distributions; (ii) permeability tensor descriptive statistics; (iii) porosity-permeability relationships and classical model fits; (iv) tensor structural properties including positive-definiteness, symmetry, and anisotropy; (v) cross-split distributional consistency; and (vi) outlier identification. The sections below report these analyses in full; all statistics are computed on the held-out test set unless indicated otherwise.

A.1 Descriptive Statistics

Table 3 summarizes key statistical properties across all data splits. All permeability values are in lattice units. The porosity distribution is moderately left-skewed (skewness ≈ -0.55) and significantly non-normal (Shapiro-Wilk $p \approx 0$ across all splits), consistent with the connectivity-based post-processing that removes isolated pore clusters and concentrates mass at higher porosity values. Principal permeabilities (diagonal elements) are strongly right-skewed in linear space (skewness ≈ 1.5 , kurtosis $\approx 2-4$) and span $[0.0020, 3.19]$ in lattice units, exceeding three orders of magnitude in \log_{10} -space. Off-diagonal elements are nearly symmetric about zero (skewness $|\rho| < 0.1$ in train and test; slightly more skewed in validation due to sampling variability) and exhibit heavy tails (kurtosis $\approx 9-13$), reflecting the predominantly isotropic character of the media: off-diagonal coupling is rare, small, and symmetrically distributed. The ratio of diagonal to off-diagonal standard deviation is approximately $5.1\times$ across all splits, quantifying the scale disparity between components that fundamentally motivates the off-diagonal prioritization in the loss function (Section 2.4).

A.2 Microstructure Geometry

All images are confirmed to be strictly binary across all splits, with zero non-binary pixels. Run-length encoding of binary rows and columns yields mean horizontal and vertical pore chord lengths of approximately 27.3 px and 27.2 px respectively, with a run-length anisotropy index of $\eta = |l_h - l_v| / (l_h + l_v) < 0.004$ in all splits, confirming the isotropic character of the generated pore geometries and providing quantitative justification for the D4-equivariant augmentation strategy (Section 2.5.1).

Table 3: Comprehensive dataset statistics across training, validation, and test splits. All permeability values in lattice units. K_{diag} : diagonal elements (K_{xx} , K_{yy}); K_{off} : off-diagonal elements (K_{xy} , K_{yx}); λ_{min} , λ_{max} : smallest and largest eigenvalues of \mathbf{K} ; AR: anisotropy ratio $\lambda_{\text{max}}/\lambda_{\text{min}}$; δ : off-diagonal dominance $|K_{\text{off}}|/(|K_{\text{diag}}| + |K_{\text{off}}|)$.

Property	Train	Validation	Test
<i>Partitioning</i>			
Number of samples	16,000	4,000	4,000
Image dimensions	128×128	128×128	128×128
<i>Microstructure geometry</i>			
Strictly binary (no. non-binary pixels)	True (0)	True (0)	True (0)
Porosity ϕ (mean \pm std)	0.711 ± 0.124	0.710 ± 0.125	0.713 ± 0.124
Porosity range [ϕ_{min} , ϕ_{max}]	[0.227, 0.900]	[0.265, 0.900]	[0.297, 0.900]
Porosity IQR	0.187	0.187	0.189
Porosity skewness	-0.55	-0.54	-0.55
Horizontal pore chord (px)	27.25	27.18	27.58
Vertical pore chord (px)	27.17	26.97	27.66
Run-length anisotropy index	0.0015	0.0038	0.0014
<i>Diagonal permeability K_{diag}</i>			
Range	[0.0027, 3.08]	[0.0034, 3.19]	[0.0027, 2.81]
Mean \pm std	0.369 ± 0.344	0.364 ± 0.346	0.372 ± 0.343
\log_{10} span (orders of magnitude)	3.06–3.12	2.87–2.95	2.86–3.02
Skewness	1.49–1.57	1.49–1.67	1.47–1.48
<i>Off-diagonal permeability K_{off}</i>			
Range	[-0.640, 0.645]	[-0.749, 0.449]	[-0.489, 0.480]
Mean \pm std	0.001 ± 0.067	-0.002 ± 0.069	0.002 ± 0.066
Kurtosis (excess)	≈ 9.3	≈ 12.8	≈ 7.0
Diag./off-diag. std ratio	$5.15\times$	$5.01\times$	$5.20\times$
<i>Tensor structural properties</i>			
Frobenius norm (mean \pm std)	0.538 ± 0.478	0.531 ± 0.480	0.543 ± 0.476
Trace $K_{xx} + K_{yy}$ (mean \pm std)	0.738 ± 0.664	0.729 ± 0.667	0.744 ± 0.661
Determinant (mean \pm std)	0.234 ± 0.403	0.232 ± 0.409	0.235 ± 0.394
<i>Tensor symmetry $\varepsilon_{\text{sym}} = K_{xy} - K_{yx}$</i>			
Mean symmetry error	7.97×10^{-6}	7.69×10^{-6}	7.59×10^{-6}
Max symmetry error	6.1×10^{-4}	6.7×10^{-4}	3.3×10^{-4}
Fraction with $\varepsilon_{\text{sym}} > 10^{-3}$	0/16,000	0/4,000	0/4,000
Fraction with $\varepsilon_{\text{sym}} > 10^{-4}$	1.07%	1.05%	0.82%
<i>Positive-definiteness</i>			
100% PD ($\lambda_{\text{min}} > 0$)	✓	✓	✓
λ_{min} (mean; min; p_5)	0.289; 1.5×10^{-6} ; 0.019	0.287; 5.2×10^{-4} ; 0.019	0.292; 2.1×10^{-3} ; 0.020
λ_{max} (mean; max; p_{95})	0.448; 3.10; 1.261	0.442; 3.20; 1.241	0.452; 2.81; 1.273
<i>Anisotropy ratio AR = $\lambda_{\text{max}}/\lambda_{\text{min}}$</i>			
Median AR	1.625	1.627	1.624
90th-percentile AR	3.32	3.33	3.34
Fraction AR > 2	30.6%	31.0%	30.3%
Fraction AR > 5	4.1%	4.4%	4.0%
Fraction AR > 10	0.79%	0.88%	1.03%
Maximum AR	53,242	92.2	36.1
<i>Off-diagonal dominance δ</i>			
Mean δ (median)	0.116 (0.096)	0.117 (0.099)	0.115 (0.096)
Maximum δ	0.500	0.493	0.471

A.3 Porosity-Permeability Relationships

The Spearman rank correlation between porosity and diagonal permeability is $\rho_s(\phi, K_{\text{diag}}) \approx +0.940$ ($p = 0$) across all splits, confirming a strong monotonic relationship. By contrast, $\rho_s(\phi, K_{\text{off}}) \approx +0.01$ (not significant, $p > 0.05$ in train and test), confirming that off-diagonal coupling is independent of porosity and must be inferred from geometric anisotropy features rather than scalar porosity values. This dissociation between diagonal and off-diagonal predictors provides direct physical motivation for the FiLM conditioning design, in which porosity modulates only the magnitude of the transport coefficients while image-derived geometric features determine anisotropic coupling (Section 2.2.2).

Table 4 reports Kozeny-Carman (KC) and power-law (PL) fits to the porosity-permeability relationship. Both models explain approximately 79% of variance in diagonal permeability ($R^2 \approx 0.789\text{--}0.791$), consistent across splits. The fitted power-law exponent $n \approx 4.8\text{--}4.9$ lies within the physically accepted range of 3–8 for consolidated porous media and is essentially identical across splits (within one standard error), confirming statistical equivalence of the three partitions. The remaining $\approx 21\%$ of variance not captured by scalar porosity corresponds to geometric features, tortuosity, and connectivity effects that the MaxViT backbone is designed to learn.

Table 4: Porosity-permeability model fits on mean diagonal permeability $\bar{K}_{\text{diag}} = \frac{1}{2}(K_{xx} + K_{yy})$ across data splits. KC: Kozeny-Carman fit $\bar{K} = C\phi^3/(1 - \phi)^2$; PL: power-law fit $\bar{K} = C\phi^n$. ρ_s : Spearman rank correlation between ϕ and \bar{K}_{diag} .

Split	Kozeny-Carman		Power law			ρ_s
	C	R^2	C	n	R^2	
Train	0.0242	0.789	1.337	4.81	0.777	0.967
Val	0.0240	0.791	1.337	4.84	0.776	0.967
Test	0.0243	0.790	1.371	4.89	0.791	0.968

A.4 Cross-Split Distributional Consistency

Statistical equivalence of the three splits was verified through two-sample Kolmogorov-Smirnov (KS) tests and Jensen-Shannon divergence (JSD) measurements on all five variables (K_{xx} , K_{xy} , K_{yx} , K_{yy} , ϕ). Results are summarized in Table 5.

All 15 KS tests fail to reject the null hypothesis of equal distributions at the $\alpha = 0.05$ level ($p > 0.13$ for all pairs and variables), with maximum observed KS statistic of 0.026. JSD values are bounded above by 0.007 across all variable-pair combinations, corresponding to near-identical distributions (JSD = 0 for identical distributions, JSD = $\ln 2 \approx 0.693$ for maximally separated distributions). These results confirm that the random partitioning protocol produces statistically indistinguishable splits and that no distributional shift is present between training, validation, and test sets, validating that reported test-set performance provides an unbiased estimate of generalization.

A.5 Outlier Analysis

Outlier analysis was conducted along three axes: Mahalanobis distance in the joint permeability tensor space (flagging multivariate extremes), extreme marginal porosity (top and bottom 1%), and high tensor anisotropy (top 5% by anisotropy ratio AR). Results are summarized in Table 6.

By construction, Mahalanobis outliers at the 99th-percentile threshold constitute exactly 1% of each split. High-AR samples ($\text{AR} > p_{95}$) account for 5% of each split, with 95th-percentile AR thresholds of 4.47–4.63 across splits. These high-anisotropy samples represent the primary challenge regime for off-diagonal permeability prediction; their analysis is detailed

Table 5: Cross-split distributional consistency. KS: two-sample Kolmogorov-Smirnov statistic and p -value (reject if $p < 0.05$). JSD: Jensen-Shannon divergence (bounded in $[0, \ln 2]$; values near 0 indicate near-identical distributions). All KS tests fail to reject the null hypothesis of equal distributions ($p > 0.05$).

Pair	Variable	KS stat	p -value	JSD
Train vs. Val	K_{xx}	0.0154	0.432	0.00353
	K_{xy}	0.0174	0.286	0.00305
	K_{yy}	0.0134	0.605	0.00368
	ϕ	0.0141	0.547	0.00355
Train vs. Test	K_{xx}	0.0141	0.541	0.00312
	K_{xy}	0.0106	0.864	0.00385
	K_{yy}	0.0117	0.764	0.00366
	ϕ	0.0143	0.524	0.00347
Val vs. Test	K_{xx}	0.0260	0.134	0.00437
	K_{xy}	0.0208	0.355	0.00552
	K_{yy}	0.0208	0.355	0.00534
	ϕ	0.0225	0.263	0.00696

in Appendix H.4. No samples were excluded from training or evaluation on the basis of these outlier criteria; the metrics are reported as characterization of the data distribution.

Table 6: Outlier summary across data splits. Mahalanobis: samples beyond the 99th-percentile Mahalanobis distance in the joint tensor space. Extreme ϕ : samples in the top or bottom 1% of the marginal porosity distribution. High AR: samples in the top 5% of the anisotropy ratio distribution.

Split	Mahalanobis ($> p_{99}$)	High ϕ ($> p_{99}$)	Low ϕ ($< p_1$)	High AR ($> p_{95}$)
Train ($n = 16,000$)	160 (1.00%)	159 ($\phi > 0.896$)	160 ($\phi < 0.396$)	800 (AR > 4.59)
Val ($n = 4,000$)	40 (1.00%)	40 ($\phi > 0.896$)	40 ($\phi < 0.390$)	200 (AR > 4.63)
Test ($n = 4,000$)	40 (1.00%)	39 ($\phi > 0.896$)	40 ($\phi < 0.401$)	200 (AR > 4.47)

A.6 LBM Symmetry and Positive-Definiteness

Tensor symmetry is preserved by the LBM solver to $\varepsilon_{\text{sym}} < 8 \times 10^{-6}$ across all splits (mean values $7.59\text{--}7.97 \times 10^{-6}$; see Table 3). No sample in any split exhibits $\varepsilon_{\text{sym}} > 10^{-3}$, and fewer than 1.1% of samples in any split exceed 10^{-4} . For reference, the FP64 machine epsilon is $\approx 10^{-16}$; the observed symmetry error lies approximately ten orders of magnitude above floating-point rounding but remains ten or more orders of magnitude below any practical engineering tolerance. The term “near-machine precision” used in the main text refers to this engineering interpretation.

All 24,000 labeled samples are strictly positive-definite ($\lambda_{\min} > 0$, verified to $\lambda_{\min} > 10^{-12}$), confirming that the ground-truth tensors satisfy the thermodynamic constraint required by Darcy’s law and providing a reliable signal for training the positivity penalty term (Equation 17).

B MaxViT Architecture Details

B.1 Stage Configuration for 128×128 Input

Table 7 provides stage-level dimensions and block counts for MaxViT-Base when processing 128×128 single-channel inputs, as used in this work.

Table 7: MaxViT-Base stage configuration for 128×128 input. Block size $P = 8$ is fixed across all stages.

Stage	Spatial resolution	Channels	MaxViT blocks	Attention regime
1	32×32	64	2	Block (4×4 blocks) + Grid
2	16×16	128	6	Block (2×2 blocks) + Grid
3	8×8	256	14	Full self-attention (spatial $\leq P$)
4	4×4	512	3	Full self-attention (spatial $\leq P$)

B.2 Multi-Axis Attention for 128×128 Input

Each MaxViT block applies two sequential attention operations. Block-local attention partitions the feature map into non-overlapping $P \times P$ windows, with $P = 8$ fixed across all stages. For Stages 1 and 2, where the spatial resolution exceeds the block size, the partition produces $4 \times 4 = 16$ and $2 \times 2 = 4$ blocks respectively; grid-global attention then integrates information across these spatially distinct regions by attending along dilated grid positions. For Stages 3 and 4, the spatial resolutions (8×8 and 4×4) are smaller than or equal to the block size $P = 8$, so the feature map constitutes a single block and full self-attention is applied within the entire stage feature map. This graceful degradation preserves the attention mechanism across all stages without modification to the underlying implementation.

B.3 Input Adaptation

The standard MaxViT-Base model accepts 384×384 RGB images. Two adaptations are applied here. The input channel count is reduced from three to one (`in_chans=1`), with pretrained spatial filters preserved via channel averaging so that learned texture and edge representations are retained. The image size is set to 128×128 (`img_size=128`), which triggers bicubic interpolation of all learned positional embeddings from the original 384×384 resolution; this interpolation is performed once at model initialization and introduces no training-time overhead.

C FiLM Conditioning: Placement Ablation and Encoder Configuration

C.1 Stage Placement Ablation

Five FiLM placement configurations were evaluated on the validation set to determine which backbone stages should receive porosity conditioning. Each configuration was trained for the full Phase 4 training run from the same Phase 3 checkpoint; validation R^2 at the best epoch (determined by early stopping) served as the selection criterion.

Stage 1 features encode low-level edge detection and solid-fluid boundary localization; their relevant length scale corresponds to individual interface sharpness rather than pore-body or pore-throat geometry, where porosity provides meaningful context. Applying FiLM conditioning to Stage 1 provided no additional benefit and marginally degraded validation performance, suggesting that low-level feature representations are disrupted by scalar conditioning. The Stages 2–4 configuration achieved the highest validation R^2 , confirming that porosity conditioning is most beneficial at the levels of abstraction where connectivity patterns and global pore-network topology are encoded.

C.2 Porosity Encoder Dimensionality Search

The porosity encoder output dimensionality was selected from $\{32, 64, 128\}$ using the same validation-set procedure. A 32-dimensional embedding produced slight underfitting of the porosity-

permeability nonlinearity (validation R^2 approximately 0.0003 lower than the 64-dimensional baseline). A 128-dimensional embedding introduced marginal overfitting relative to the scalar conditioning signal, with a small increase in the training-validation R^2 gap and no improvement on the test set. The 64-dimensional embedding provides a compact yet expressive representation and was adopted for all Phase 4 experiments.

D Training Configuration

D.1 Optimizer and Schedule

The AdamW optimizer [87] is used throughout, with $\beta_1 = 0.9$, $\beta_2 = 0.999$, and $\varepsilon = 10^{-8}$. The learning-rate schedule in all phases comprises a linear warmup phase followed by cosine annealing. Table 8 summarizes phase-specific settings.

Table 8: Training configuration by phase. LR: learning rate; WD: weight decay; BS: batch size; Pat.: early stopping patience (epochs, monitoring validation R^2); WU: warmup duration (epochs).

Phase	Epochs	Init. from	LR _{max}	LR _{min}	WU	WD	BS	Pat.
2	600	ImageNet	10^{-4}	10^{-7}	50	0.05	32	100
3	600	Phase 2	10^{-4}	10^{-5}	50	0.01	32	100
4	600	Phase 3	10^{-4}	10^{-6}	50	0.01	32	150

D.2 Progressive Unfreezing Schedule (Phase 2)

Table 9: Progressive unfreezing schedule in Phase 2.

Epoch range	Trainable components
0–50	Regression head only (backbone frozen)
50–150	Regression head + backbone Stages 3–4 (Stages 1–2 and stem frozen)
150–600	Full model (all parameters)

D.3 Loss-Function Weights by Phase

Table 10: Physics-aware loss-function weights by training phase. λ_{offdiag} is not active (–) in Phase 2.

Phase	λ_{sym}	λ_{pos}	λ_{offdiag}	(w_d, w_o)
2	0.10	0.05	–	(1.0, 1.0)
3–4	0.20	0.05	1.0	(1.0, 1.5)

D.4 Checkpointing Strategy

Multiple checkpoints are maintained during training: the best validation R^2 checkpoint (primary checkpoint for evaluation), the best validation MSE checkpoint (alternative metric), and periodic snapshots every 50 epochs for post-hoc analysis. In Phase 4, the SWA model (weight-averaged from epochs 400–600) and the EMA model (continuously averaged throughout training) are tracked as additional evaluation candidates, as described in Section 2.3.3 and Appendix F. The Phase 4 early stopping patience is increased to 150 epochs (versus 100 for Phases 2–3), reflecting the smaller trainable parameter set and correspondingly slower validation-metric dynamics.

D.5 DataLoader Configuration

Data loading utilizes the PyTorch `DataLoader` with memory pinning for I/O efficiency. Four workers are used in Phase 2; this is reduced to zero workers in Phases 3–4 because the augmentation pipeline involves per-sample computations (elastic deformation Jacobians, morphological operations) that are more efficiently executed in the main process under the memory constraints of the training GPU.

E Data Augmentation: Details and Parameter Search

E.1 D4 Transformation Matrices

Table 11 provides the coordinate-transformation matrix \mathbf{P} and the resulting permeability tensor $\mathbf{K}' = \mathbf{PKP}^T$ for each of the eight D_4 group elements.

Table 11: D_4 transformation matrices \mathbf{P} and the corresponding permeability tensor transformations $\mathbf{K}' = \mathbf{PKP}^T$. Entries use $a = K_{xx}$, $b = K_{xy} = K_{yx}$, $c = K_{yy}$.

Transformation	\mathbf{P}	\mathbf{K}'
Identity	$\begin{bmatrix} 1 & 0 \\ 0 & 1 \end{bmatrix}$	$\begin{bmatrix} a & b \\ b & c \end{bmatrix}$
Rotation 90°	$\begin{bmatrix} 0 & -1 \\ 1 & 0 \end{bmatrix}$	$\begin{bmatrix} c & -b \\ -b & a \end{bmatrix}$
Rotation 180°	$\begin{bmatrix} -1 & 0 \\ 0 & -1 \end{bmatrix}$	$\begin{bmatrix} a & b \\ b & c \end{bmatrix}$
Rotation 270°	$\begin{bmatrix} 0 & 1 \\ -1 & 0 \end{bmatrix}$	$\begin{bmatrix} c & -b \\ -b & a \end{bmatrix}$
Horizontal flip	$\begin{bmatrix} -1 & 0 \\ 0 & 1 \end{bmatrix}$	$\begin{bmatrix} a & -b \\ -b & c \end{bmatrix}$
Vertical flip	$\begin{bmatrix} 1 & 0 \\ 0 & -1 \end{bmatrix}$	$\begin{bmatrix} a & -b \\ -b & c \end{bmatrix}$
Diagonal flip	$\begin{bmatrix} 0 & 1 \\ 1 & 0 \end{bmatrix}$	$\begin{bmatrix} c & b \\ b & a \end{bmatrix}$
Anti-diagonal flip	$\begin{bmatrix} 0 & -1 \\ -1 & 0 \end{bmatrix}$	$\begin{bmatrix} c & b \\ b & a \end{bmatrix}$

E.2 Group-Equivariant Networks: Design Choice Discussion

Group Equivariant Convolutional Networks (G-CNNs) [70–72] build exact equivariance to a specified symmetry group directly into the weight-sharing structure through group convolutions, guaranteeing that the network output transforms predictably under all group elements by construction. This provides architecturally guaranteed equivariance rather than the statistical, augmentation-based approximation employed in this work.

This approach was not adopted for two reasons. First, MaxViT’s ImageNet pretraining provides strong low- and mid-level visual features that transfer effectively to porous media images despite the domain gap; replacing the MaxViT backbone with a G-CNN architecture trained from scratch would discard this pretraining entirely. Second, empirical evaluation demonstrates that comprehensive D_4 augmentation achieves sufficiently precise equivariance for practical purposes: the mean symmetry error $\varepsilon_{\text{sym}} = 3.95 \times 10^{-7}$ over the 4,000-sample test set indicates that Onsager reciprocity is satisfied to near-machine precision, and any residual equivariance violation is orders of magnitude below the measurement uncertainty of LBM simulation. Future work may investigate G-CNN pretraining strategies that combine symmetry guarantees with transfer learning for porous media applications.

E.3 Phase 3 Augmentation Parameter Search

Augmentation parameters were determined through a two-stage grid search on the validation set, with no test-set access at any stage.

Stage 1: per-class probability search. Each transformation class (erosion, dilation, elastic deformation, cutout) was evaluated over the probability grid $\{0.05, 0.08, 0.10, 0.15, 0.20\}$ independently, with other parameters held at nominal values ($\alpha = 3.0, \sigma = 2.0$). Each configuration was trained for 150 epochs from the Phase 2 checkpoint.

Stage 2: elastic deformation magnitude search. Using the per-class probabilities identified in Stage 1, elastic deformation magnitude was swept over $\alpha \in \{2.0, 3.0, 5.0, 7.0\}$.

The optimization criterion was validation R^2 for the off-diagonal component K_{xy} , rather than the overall variance-weighted R^2 . Diagonal components K_{xx} and K_{yy} proved robustly learned across the full augmentation search range, making the off-diagonal prediction accuracy the most sensitive and discriminating indicator of augmentation quality. Excessive augmentation (probabilities above approximately 15% per class, or $\alpha > 3.0$) introduced gradient variance that degraded off-diagonal convergence while diagonal components remained largely unaffected. The best configuration selected was: $p_{\text{erosion}} = p_{\text{dilation}} = 0.08, p_{\text{elastic}} = 0.08$ with $\alpha = 3.0$ and $\sigma = 2.0, p_{\text{cutout}} = 0.10$.

E.4 Phase 3–4 Augmentation Pipeline

Algorithm 1 Phases 3–4 Augmentation Pipeline (applied per training sample)

Require: Image $I \in \{0, 1\}^{128 \times 128}$, permeability tensor $\mathbf{K} \in \mathbb{R}^{2 \times 2}$

Ensure: Augmented image I' , consistently transformed tensor \mathbf{K}'

```

1: Sample  $g \sim \text{Uniform}(D_4)$  ▷ Apply D4 transformation with probability 1.0
2:  $I \leftarrow g(I); \mathbf{K} \leftarrow \mathbf{P}_g \mathbf{K} \mathbf{P}_g^T$ 
3: if  $u_1 \sim \text{Uniform}(0, 1) < 0.08$  then ▷ Elastic deformation
4:   Generate displacement fields  $\delta_x, \delta_y$  from  $\alpha \cdot \mathcal{G}_{\sigma=2.0}(\mathcal{U}(-1, 1))$ 
5:    $I \leftarrow I(x + \delta_x, y + \delta_y)$  ▷ Bilinear interpolation
6:   Compute Jacobian  $\mathbf{J}$  at image center via central finite differences
7:    $\mathbf{K} \leftarrow \mathbf{J} \mathbf{K} \mathbf{J}^T; \mathbf{K} \leftarrow (\mathbf{K} + \mathbf{K}^T)/2$ 
8: end if
9: if  $u_2 \sim \text{Uniform}(0, 1) < 0.08$  then ▷ Erosion
10:   $I \leftarrow \min_{(i,j) \in \mathcal{N}_{3 \times 3}} I(x + i, y + j)$ 
11: end if
12: if  $u_3 \sim \text{Uniform}(0, 1) < 0.08$  then ▷ Dilation
13:   $I \leftarrow \max_{(i,j) \in \mathcal{N}_{3 \times 3}} I(x + i, y + j)$ 
14: end if
15: if  $u_4 \sim \text{Uniform}(0, 1) < 0.10$  then ▷ Cutout
16:  Sample random rectangle  $\mathcal{R} \subseteq [0, 127]^2$  with  $|\mathcal{R}| \leq 8 \times 8$ 
17:   $I(x, y) \leftarrow 0.5$  for  $(x, y) \in \mathcal{R}$ 
18: end if
19:  $I' \leftarrow I; \mathbf{K}' \leftarrow \mathbf{K}$ 

```

Morphological operations and cutout masking do not require explicit tensor transformation: morphological perturbations are sufficiently small (3×3 kernel, 8% probability) that the geometric structure-permeability mapping is preserved, and the network learns the permeability of the modified geometry through convolutional feature extraction; cutout occludes a small spatial region without altering the global pore geometry governing the permeability tensor.

F Ensemble Methods: Stochastic Weight Averaging and Exponential Moving Average

F.1 Stochastic Weight Averaging (SWA)

SWA [74] maintains a running arithmetic mean of model weights sampled during late-stage training, where the model has converged but continues to explore locally optimal regions due to stochastic gradient noise. Starting at epoch $t_{\text{SWA}} = 400$ (in Phase 4), the SWA model θ_{SWA} is initialized with the current weights θ_{400} and updated after each subsequent epoch t via:

$$\theta_{\text{SWA}} \leftarrow \frac{n_{\text{models}} \cdot \theta_{\text{SWA}} + \theta_t}{n_{\text{models}} + 1}, \quad (24)$$

where n_{models} counts the number of models aggregated so far. The SWA learning rate is fixed at $\eta_{\text{SWA}} = 5 \times 10^{-6}$ throughout epochs 400–600, substantially lower than the cosine-annealed base rate at epoch 400, encouraging broader exploration near the converged solution. SWA aggregates 200 model snapshots without incurring any additional training cost.

After training, batch-normalization running statistics are recalibrated by passing the full training set through θ_{SWA} in evaluation mode once. This recalibration step is critical: weight averaging shifts the effective activation distributions relative to the batch-normalization statistics accumulated during training, and without recalibration the SWA model would apply incorrect normalization at inference time.

F.2 Exponential Moving Average (EMA)

EMA [80] maintains a continuously updated exponentially-weighted average of model parameters θ_{EMA} throughout training, updated after every optimizer step via:

$$\theta_{\text{EMA}} \leftarrow \lambda_{\text{EMA}} \cdot \theta_{\text{EMA}} + (1 - \lambda_{\text{EMA}}) \cdot \theta_t, \quad (25)$$

with decay $\lambda_{\text{EMA}} = 0.9999$. For a constant step size, this corresponds to an effective averaging window of $1/(1 - \lambda_{\text{EMA}}) = 10,000$ gradient steps. The EMA model filters high-frequency weight fluctuations arising from mini-batch noise while tracking the optimization trajectory, and empirically outperforms instantaneous weights on validation data. Both θ_t and θ_{EMA} are monitored on the validation set at every epoch, and the best-performing EMA checkpoint is saved independently.

G Extended Evaluation Metrics

The following metrics complement the primary R^2 , MSE, and RRMSE reported in the main text (Section 2.6.2) to enable cross-study comparison and provide a more complete characterization of prediction quality.

Mean absolute percentage error (MAPE).

$$\text{MAPE}_{jk} = \frac{1}{N} \sum_{i=1}^N \frac{|K_{jk,i}^{\text{pred}} - K_{jk,i}^{\text{true}}|}{|K_{jk,i}^{\text{true}}| + \varepsilon} \times 100 \%, \quad (26)$$

where $\varepsilon = 10^{-8}$ prevents division by zero.

Range-normalized RMSE (NRMSE).

$$\text{NRMSE}_{jk} = \frac{\text{RMSE}_{jk}}{K_{jk,\text{max}}^{\text{true}} - K_{jk,\text{min}}^{\text{true}} + \varepsilon} \times 100 \%, \quad (27)$$

expressing prediction error as a fraction of the component’s observed range.

Willmott’s index of agreement (d).

$$d = 1 - \frac{\sum_i (y_i^{\text{true}} - y_i^{\text{pred}})^2}{\sum_i (|y_i^{\text{pred}} - \bar{y}| + |y_i^{\text{true}} - \bar{y}|)^2}, \quad (28)$$

bounded in $[0, 1]$ with $d = 1$ indicating perfect agreement [84].

Kling-Gupta efficiency (KGE).

$$\text{KGE} = 1 - \sqrt{(r - 1)^2 + (\alpha - 1)^2 + (\beta - 1)^2}, \quad (29)$$

where r is Pearson correlation, $\alpha = \sigma_{\hat{y}}/\sigma_y$ is the variability ratio, and $\beta = \mu_{\hat{y}}/\mu_y$ is the bias ratio [83].

Spearman rank correlation (ρ_s). Monotonic predictive skill, insensitive to distributional assumptions, assessed through the Spearman rank correlation coefficient.

All metrics are computed separately for diagonal (K_{xx} , K_{yy}) and off-diagonal (K_{xy} , K_{yx}) components. The diagonal-to-off-diagonal R^2 gap, $\Delta R^2 = R_{\text{diag}}^2 - R_{\text{off}}^2$, is reported as a summary statistic quantifying the systematic prediction difficulty for anisotropy-encoding components.

H Statistical Analyses

Four complementary post-hoc analyses were conducted on the held-out test set ($N = 4,000$ samples) using the best-performing checkpoints. Each analysis addresses a specific methodological concern and is described in a dedicated subsection below.

H.1 Bootstrap Statistical Validation

Method. Let $\mathcal{D}_{\text{test}} = \{(\mathbf{y}_i, \hat{\mathbf{y}}_i)\}_{i=1}^N$ denote the set of ground-truth and predicted permeability tensors on the held-out test set. A single deterministic forward pass through the trained network yields the prediction matrix $\hat{\mathbf{Y}} \in \mathbb{R}^{N \times 4}$, which is treated as fixed throughout the bootstrap procedure.

In each of $B = 1,000$ bootstrap iterations, an index set $\mathcal{I}_b = \{i_1, \dots, i_N\}$ is drawn by sampling with replacement from $\{1, \dots, N\}$ using a fixed random seed (`seed=42`). The metric function $f(\cdot)$ is evaluated on the resampled pairs $(\mathbf{Y}[\mathcal{I}_b], \hat{\mathbf{Y}}[\mathcal{I}_b])$, yielding a bootstrap replicate $f^{(b)}$. The collection $\{f^{(b)}\}_{b=1}^B$ constitutes the empirical bootstrap distribution of the metric.

Confidence intervals are computed using the bias-corrected and accelerated (BCa) method [88], which corrects for both bias in the bootstrap distribution and skewness in the sampling distribution. The bias-correction constant is $\hat{z}_0 = \Phi^{-1}(\text{Pr}[f^{(b)} < f_{\text{obs}}])$, where Φ^{-1} is the standard normal quantile function and f_{obs} is the observed metric on the full test set. The acceleration constant is set to $\hat{a} = 0$ (reducing BCa to bias-corrected percentile), and the 95% confidence limits are:

$$[f_{\alpha_1}, f_{\alpha_2}], \quad \alpha_{1,2} = \Phi\left(\hat{z}_0 + \frac{\hat{z}_0 \pm z_{0.025}}{1 - \hat{a}(\hat{z}_0 \pm z_{0.025})}\right), \quad (30)$$

where $z_{0.025} = 1.96$.

Metrics. The bootstrap procedure is applied to global R^2 , MSE, RMSE, MAE, MAPE, RRMSE, and the mean off-diagonal symmetry error $\varepsilon_{\text{sym}} = \mathbb{E}[|\hat{K}_{xy} - \hat{K}_{yx}|]$. All metrics are additionally computed per tensor component (K_{xx} , K_{xy} , K_{yx} , K_{yy}), yielding 95% BCa confidence intervals at the component level. Results are reported in the bootstrap summary table and visualized as density histograms with confidence bands.

H.2 Extended Performance Metrics and Residual Diagnostics

Absolute and relative metrics. Absolute metrics (RMSE, MAE) and the scale-invariant metrics defined in Appendix G (MAPE, RRMSE, NRMSE) are reported for all tensor components, with diagonal-off-diagonal decomposition. Willmott’s index of agreement, the Kling-Gupta efficiency, and Spearman rank correlation are computed per component to provide a multifaceted assessment suitable for cross-study comparison.

Residual diagnostics. Component-wise residuals $e_i = \hat{K}_c^{(i)} - K_c^{(i)}$ are examined through: (i) signed-error histograms with kernel density estimates to assess bias and distributional shape; (ii) residuals-versus-fitted plots with LOWESS trend lines to detect heteroscedasticity; and (iii) normal quantile-quantile (Q-Q) plots accompanied by Shapiro-Wilk tests to assess the normality assumption underlying confidence interval calculations.

H.3 Uncertainty Quantification via Monte Carlo Dropout

MC-Dropout inference. At test time, all dropout layers are set to training mode while batch-normalization layers remain in evaluation mode. For each test sample, $T = 100$ stochastic forward passes are performed, yielding a distribution of predictions $\{\hat{\mathbf{y}}^{(t)}\}_{t=1}^T$. The predictive mean and epistemic standard deviation are estimated as:

$$\hat{\boldsymbol{\mu}} = \frac{1}{T} \sum_{t=1}^T \hat{\mathbf{y}}^{(t)}, \quad (31)$$

$$\hat{\boldsymbol{\sigma}} = \sqrt{\frac{1}{T} \sum_{t=1}^T (\hat{\mathbf{y}}^{(t)} - \hat{\boldsymbol{\mu}})^2}. \quad (32)$$

Symmetric prediction intervals at nominal coverage $1 - \alpha$ are obtained as $\hat{\boldsymbol{\mu}} \pm z_{\alpha/2} \hat{\boldsymbol{\sigma}}$.

Calibration assessment. Calibration is assessed via an empirical coverage curve: for each nominal level $\alpha \in [0.05, 0.99]$, the fraction of test samples whose true value lies within the corresponding prediction interval is computed and plotted against the nominal level (reliability diagram). A well-calibrated model yields a curve close to the diagonal [89]. The mean calibration error is:

$$\text{MCE} = \frac{1}{|\mathcal{A}|} \sum_{\alpha \in \mathcal{A}} |p_{\text{nom}}(\alpha) - p_{\text{emp}}(\alpha)|, \quad (33)$$

where p_{nom} and p_{emp} are the nominal and empirical coverage values, respectively.

Reliability by confidence. To verify that predicted uncertainty is informative, test samples are stratified into deciles by their mean epistemic standard deviation $\bar{\sigma}_i = \frac{1}{4} \sum_c \hat{\sigma}_{i,c}$. Within each decile, mean absolute error is computed and plotted as a function of decile-mean uncertainty. A monotonically increasing relationship confirms that high-uncertainty predictions correspond to higher errors, validating the utility of the uncertainty estimate for flagging low-confidence predictions in downstream engineering applications.

H.4 Anisotropy Gap and High-Anisotropy Error Analysis

Anisotropy measures. Three complementary anisotropy measures are computed from the ground-truth permeability tensors. The eigenvalue anisotropy ratio, $\text{AR}_{\text{eig}} = |\lambda_{\text{max}}|/|\lambda_{\text{min}}|$, where λ_{max} and λ_{min} are the eigenvalues of the 2×2 permeability tensor \mathbf{K} , is the physically meaningful anisotropy measure, approaching unity for isotropic media. The component anisotropy ratio, $\text{AR}_{\text{comp}} = \max(|K_{xx}|, |K_{yy}|) / [\max(|K_{xy}|, |K_{yx}|) + \varepsilon]$, measures the relative dominance of diagonal over off-diagonal entries. The off-diagonal dominance fraction, $\delta = \bar{K}_{\text{off}} / (\bar{K}_{\text{diag}} + \bar{K}_{\text{off}} + \varepsilon)$, where \bar{K}_{diag} and \bar{K}_{off} are mean absolute diagonal and off-diagonal magnitudes, indicates media in which off-diagonal permeability is particularly significant.

Error stratification. Test samples are divided into $n = 10$ equi-populated bins according to AR_{eig} . Within each bin, per-component R^2 , RRMSE, and MAPE are computed, together with aggregate diagonal and off-diagonal R^2 . The evolution of the diagonal-to-off-diagonal R^2 gap with anisotropy identifies the regimes in which the model struggles most.

High-anisotropy deep-dive. The 500 most anisotropic test samples (top 12.5%) are isolated and examined with dedicated parity plots (predicted versus true) for each tensor component. The eight best-predicted, eight worst-predicted, and eight most anisotropic samples are visualized alongside their input binary images, predicted and true tensor values, and per-sample MAE.

Tensor condition number and geometric image statistics. The condition number $\kappa(\mathbf{K}) = |\lambda_{\max}|/|\lambda_{\min}|$ of each ground-truth tensor is correlated with per-sample MAE via Spearman’s ρ_s to quantify how ill-conditioning amplifies prediction error. Image-level geometric proxies are also computed: (i) porosity $\phi = 1 - \bar{I}$; (ii) mean horizontal and vertical pore-chord lengths estimated from run-length encoding of binary rows and columns; (iii) a run-asymmetry index $\eta = |l_h - l_v|/(l_h + l_v + \varepsilon)$; and (iv) a gradient anisotropy index $\gamma = \langle |\partial_x I| \rangle / \langle |\partial_y I| \rangle$.

I Extended Phase 4 Results

I.1 Component-Wise Bootstrap Summary

Table 12 reports the full per-component bootstrap summary ($B = 1,000$, BCa method [88]). All confidence intervals are narrower than the between-phase performance differences ($\Delta R^2 \approx 0.002$ – 0.003 per step), confirming that progressive gains reported in Table 2 are statistically significant.

I.2 Anisotropy-Stratified Metrics

Table 13 reports R^2 and RRMSE for all four tensor components across the ten equi-populated AR bins ($n = 400$ samples each) used to produce Figure 12(b,d) in the main text. The near-isotropic bin ($\text{AR} \approx 1.11$) accounts for the largest ΔR^2 and is the primary residual challenge for off-diagonal prediction, as discussed in Section 3.2.2.

The table confirms that the ΔR^2 gap is non-monotonic in AR, peaking at the lowest anisotropy bin and reaching a minimum of 0.0098 at $\text{AR} \approx 1.89$. The secondary widening at $\text{AR} \approx 5.87$ ($\Delta R^2 = 0.0151$) is modest in absolute terms and reflects the increased difficulty of resolving extreme coupling magnitudes; it does not represent a failure mode but rather the expected increase in absolute off-diagonal RMSE as coupling strength grows.

I.3 MC-Dropout Uncertainty: Per-Component Summary

Table 14 extends the main-text uncertainty summary (Section 3.4.7) with full per-component statistics.

The uncertainty-error Spearman correlation is consistently positive across all four components ($\rho_s = 0.229$ – 0.304), confirming that MC-Dropout provides a useful—if partial—confidence signal. Off-diagonal components exhibit slightly higher ρ_s (0.304 versus 0.229–0.235 for diagonal), consistent with their higher prediction variability providing more discriminative uncertainty estimates. Diagonal components carry larger absolute uncertainty ($\bar{\sigma} \approx 1.26 \times 10^{-2}$) than off-diagonal ($\bar{\sigma} \approx 5.15 \times 10^{-3}$), but this reflects their larger dynamic range: the ratio $\bar{\sigma}/\text{RMSE} \approx 0.64$ is nearly identical across all four components, indicating well-calibrated relative uncertainty in this sense.

J Extended Phase Comparison Metrics

Table 15 consolidates the complete quantitative record of the three-phase progressive training framework, reporting eight metric categories across all training phases on the held-out test set

Table 12: Component-wise bootstrap statistics for Phase 4 ($B = 1,000$, 95% BCa CIs). RRMSE normalized by component mean absolute value (Equation 23).

Comp.	Metric	Observed	Boot. mean	CI low	CI high
K_{xx}	R^2	0.99674	0.99673	0.99626	0.99708
	RMSE	1.955×10^{-2}	1.956×10^{-2}	1.835×10^{-2}	2.120×10^{-2}
	MAE	1.272×10^{-2}	1.272×10^{-2}	1.224×10^{-2}	1.316×10^{-2}
	MAPE (%)	7.09	7.08	6.64	7.61
	RRMSE (%)	5.25	5.25	4.96	5.67
K_{xy}	R^2	0.97583	0.97579	0.97359	0.97792
	RMSE	1.026×10^{-2}	1.026×10^{-2}	9.87×10^{-3}	1.071×10^{-2}
	MAE	7.17×10^{-3}	7.17×10^{-3}	6.96×10^{-3}	7.41×10^{-3}
	MAPE (%)	132.3	132.8	97.0	188.7
	RRMSE (%)	24.43	24.43	23.46	25.56
K_{yx}	R^2	0.97583	0.97579	0.97360	0.97793
	RMSE	1.026×10^{-2}	1.026×10^{-2}	9.87×10^{-3}	1.071×10^{-2}
	MAE	7.17×10^{-3}	7.17×10^{-3}	6.96×10^{-3}	7.41×10^{-3}
	MAPE (%)	136.2	136.9	96.8	196.8
	RRMSE (%)	24.43	24.43	23.46	25.56
K_{yy}	R^2	0.99672	0.99671	0.99548	0.99729
	RMSE	1.964×10^{-2}	1.965×10^{-2}	1.769×10^{-2}	2.361×10^{-2}
	MAE	1.265×10^{-2}	1.265×10^{-2}	1.219×10^{-2}	1.311×10^{-2}
	MAPE (%)	7.62	7.60	7.08	8.33
	RRMSE (%)	5.28	5.28	4.75	6.31
Global	R^2	0.98628	0.98626	0.98516	0.98738
	RMSE	1.564×10^{-2}	1.566×10^{-2}	1.483×10^{-2}	1.704×10^{-2}
	RRMSE (%)	7.55	7.56	7.18	8.19
	ε_{sym}	3.95×10^{-7}	3.95×10^{-7}	3.82×10^{-7}	4.10×10^{-7}

Table 13: Anisotropy-stratified prediction performance for Phase 4. Ten equi-populated bins ($n = 400$ each) spanning the 2nd–98th percentile of the AR distribution. $\Delta R^2 = R_{\text{diag}}^2 - R_{\text{off}}^2$.

AR bin	R_{diag}^2	R_{off}^2	ΔR^2	RRMSE $_{K_{xx}}$ (%)	RRMSE $_{K_{xy}}$ (%)	RRMSE $_{K_{yy}}$ (%)
1.115	0.9966	0.8152	0.1814	3.68	60.44	3.85
1.233	0.9968	0.9148	0.0820	3.98	39.46	3.90
1.334	0.9966	0.9690	0.0276	4.32	24.32	3.78
1.439	0.9972	0.9756	0.0216	4.03	21.92	3.91
1.556	0.9963	0.9830	0.0133	5.40	20.71	5.03
1.699	0.9963	0.9836	0.0127	6.59	23.10	5.17
1.890	0.9964	0.9866	0.0098	6.44	18.95	5.94
2.201	0.9964	0.9855	0.0110	6.93	21.03	7.02
2.819	0.9955	0.9787	0.0168	9.90	22.27	7.92
5.870	0.9852	0.9701	0.0151	13.15	35.54	20.14

Table 14: Per-component MC-Dropout uncertainty statistics for Phase 4 ($T = 100$, $N = 4,000$). $\bar{\sigma}$: mean predictive standard deviation; $\tilde{\sigma}$: median; σ_{p95} : 95th-percentile uncertainty; $\rho_s(\sigma, |\varepsilon|)$: Spearman rank correlation between predictive uncertainty and absolute error.

Comp.	R^2	RMSE	$\bar{\sigma}$	$\tilde{\sigma}$	σ_{p95}	$\rho_s(\sigma, \varepsilon)$
K_{xx}	0.9967	1.966×10^{-2}	1.263×10^{-2}	9.07×10^{-3}	3.34×10^{-2}	0.229
K_{xy}	0.9756	1.031×10^{-2}	5.15×10^{-3}	3.71×10^{-3}	1.33×10^{-2}	0.304
K_{yx}	0.9756	1.031×10^{-2}	5.15×10^{-3}	3.71×10^{-3}	1.33×10^{-2}	0.304
K_{yy}	0.9967	1.974×10^{-2}	1.266×10^{-2}	9.08×10^{-3}	3.29×10^{-2}	0.235
Global	—	—	8.90×10^{-3}	6.65×10^{-3}	—	—

($N = 4,000$). It extends the condensed summary in Table 2 with per-component relative errors, bootstrap uncertainty decomposition, high-anisotropy stratification, per-component predictive uncertainty, uncertainty-error correlations, and model specification details. The sections below highlight the most consequential patterns.

Progressive improvement is consistent and monotonic. Every single metric in sections A–G improves from Phase 2 through Phase 3 to Phase 4 without exception, across global accuracy, rank-based agreement, per-component R^2 , relative error, physics compliance, and uncertainty calibration. This monotonicity across 35 reported rows is non-trivial: it confirms that no phase’s gains come at the expense of any other aspect of performance, and that the staged design—isolating one methodological contribution per phase—successfully avoids the trade-offs common in multi-objective optimization.

MAPE requires careful interpretation for off-diagonal components. Section D reports MAPE values of 132–146% for K_{xy} and K_{yx} across all phases. These figures are not indicative of poor performance: MAPE normalizes absolute error by the true value, and for near-isotropic samples where $K_{xy} \approx 0$, the denominator approaches zero, inflating the metric arbitrarily. The RRMSE values (24.43%–26.07%) normalized by the mean absolute component value provide the correct scale-invariant comparison, and the wide bootstrap confidence intervals for MAPE (e.g., [52, 99]% for Phase 4) reflect this instability. All downstream conclusions in the main text rely on RRMSE and R^2 for off-diagonal components, as recommended in Appendix G.

High-anisotropy performance reveals the most structured gain. Section E shows that $\Delta R^2_{\text{high-AR}}$ (top 500 most anisotropic test samples) drops sharply from 0.0209 in Phase 2 to 0.0132 in Phase 4—a 37% reduction—whereas the global ΔR^2 narrows only from 0.0230 to 0.0209. Notably, Phase 3 alone accounts for nearly the entire high-AR improvement ($\Delta R^2_{\text{high-AR}} = 0.0132$, essentially identical to Phase 4’s 0.0132), while Phase 4’s contribution is concentrated at global level through the FiLM magnitude scaling. The off-diagonal R^2 for the high-AR subset improves from 0.968 (Phase 2) to 0.974 (Phase 4), confirming that augmentation diversity in Phase 3 was the decisive intervention for the strongly anisotropic regime.

Uncertainty calibration improves jointly with accuracy. Section G reveals two patterns not visible in accuracy metrics alone. First, the uncertainty-error Spearman correlations (UE-corr ρ) improve across all four components from Phase 2 to Phase 4: diagonal components improve from $\rho \approx 0.196$ – 0.204 to 0.229 – 0.235 , and off-diagonal components from 0.271 to 0.304 . This confirms that SWA and EMA ensemble averaging not only reduce point-prediction errors but produce more reliable confidence estimates—a meaningful benefit for deployment workflows where uncertainty flags guide selective LBM verification. Second, off-diagonal components consistently achieve higher UE-corr ρ than diagonal (0.304 versus 0.229 – 0.235 in Phase 4),

indicating that MC-Dropout variance is a more discriminative signal for the harder-to-predict components—precisely where reliable uncertainty estimates are most valuable.

Section H makes the frozen-backbone logic explicit. The model specification section records that the backbone parameter count (118.64M) is identical across all three phases; the Phase 4 increment of 0.33M parameters represents the porosity encoder and FiLM layers exclusively. Phase 4 is the only phase with a frozen backbone, SWA, EMA, and FiLM conditioning simultaneously active. This section is included to facilitate reproducibility and to clarify that no additional pretraining, architectural search, or data expansion was performed between phases.

Table 15: Extended performance metrics across three consecutive training phases evaluated on the held-out test set ($N = 4,000$). 95% BCa bootstrap confidence intervals ($B = 1,000$ resamples) are shown in brackets; bootstrap standard deviations (σ) quantify estimator variability. Predictive uncertainty is estimated via Monte Carlo Dropout ($T = 100$ stochastic forward passes). **Bold** values mark the best result per row. Phase 2: supervised baseline with D4 augmentation; Phase 3: advanced augmentation and enhanced physics-aware loss; Phase 4: frozen backbone, FiLM porosity conditioning, SWA/EMA ensemble. Abbreviations — KGE: Kling–Gupta efficiency [83]; d : Willmott index of agreement [84]; MCE: mean calibration error (lower is better calibrated); UE-corr ρ : Spearman correlation between predicted standard deviation and absolute error; $\Delta R^2_{\text{high-AR}}$: diagonal–off-diagonal R^2 gap for the 500 most anisotropic test samples. MAPE for K_{xy}/K_{yx} reflects near-zero denominators in quasi-isotropic samples; RRMSE is the preferred relative metric in this regime (Appendix G).

Metric	Phase 4	Phase 3	Phase 2
<i>A. Global accuracy</i>			
R^2 (component-averaged)	0.98628	0.98476	0.98429
95% BCa CI	[0.98516, 0.98738]	[0.98333, 0.98604]	[0.98304, 0.98563]
Bootstrap σ	0.00059	0.00068	0.00070
R^2 (variance-weighted)	0.99604	0.99452	0.99403
MSE	2.446×10^{-4}	2.880×10^{-4}	3.226×10^{-4}
RMSE	1.564×10^{-2}	1.697×10^{-2}	1.796×10^{-2}
95% BCa CI	[0.01483, 0.01704]	[0.01617, 0.01794]	[0.01694, 0.01948]
MAE	9.920×10^{-3}	1.091×10^{-2}	1.100×10^{-2}
95% BCa CI	[0.00971, 0.01017]	[0.01065, 0.01119]	[0.01073, 0.01129]
RRMSE (%)	7.552	8.194	8.671
95% BCa CI	[7.178, 8.187]	[7.832, 8.686]	[8.178, 9.354]
MAPE (%)	70.791	72.384	74.917
95% BCa CI	[52.135, 99.030]	[54.271, 103.518]	[57.142, 108.249]
Bootstrap σ	11.989	12.745	13.521
<i>B. Rank-based and agreement metrics</i>			
Pearson r	0.99872	0.99851	0.99832
Spearman ρ_s	0.99595	0.99589	0.99572
Willmott d	0.99935	0.99920	0.99912
KGE	0.99420	0.98760	0.98244
<i>C. Per-component R^2 with 95% BCa CI</i>			
$R^2_{K_{xx}}$	0.99674	0.99607	0.99543
95% BCa CI	[0.99626, 0.99708]	[0.99554, 0.99655]	[0.99491, 0.99592]
$R^2_{K_{xy}}$	0.97583	0.97404	0.97246
95% BCa CI	[0.97359, 0.97792]	[0.97146, 0.97640]	[0.96999, 0.97503]

Continued on next page

Table 15 (continued)

Metric	Phase 4	Phase 3	Phase 2
$R_{K_{yx}}^2$	0.97583	0.97404	0.97247
95 % BCa CI	[0.97360, 0.97793]	[0.97146, 0.97639]	[0.97000, 0.97502]
$R_{K_{yy}}^2$	0.99672	0.99613	0.99557
95 % BCa CI	[0.99548, 0.99729]	[0.99539, 0.99680]	[0.99488, 0.99621]
R_{diagonal}^2 (avg.)	0.99673	0.99610	0.99550
$R_{\text{off-diag}}^2$ (avg.)	0.97583	0.97404	0.97246
<i>D. Per-component relative error</i>			
RRMSE $_{K_{xx}}$ (%)	5.25	5.77	6.12
RRMSE $_{K_{xy}}$ (%)	24.43	25.32	26.07
RRMSE $_{K_{yx}}$ (%)	24.43	25.32	26.07
RRMSE $_{K_{yy}}$ (%)	5.28	5.70	6.27
MAPE $_{K_{xx}}$ (%)	7.09	7.94	9.27
MAPE $_{K_{xy}}$ (%) [†]	132.28	135.64	141.73
MAPE $_{K_{yx}}$ (%) [†]	136.18	139.42	145.61
MAPE $_{K_{yy}}$ (%)	7.62	8.11	9.78
<i>E. Tensor-type decomposition and anisotropy</i>			
ΔR^2 (diag – off, global)	0.02090	0.02206	0.02304
$\Delta R^2_{\text{high-AR}}$ (top 500)	0.01319	0.01321	0.02093
$R_{K_{xx}}^2$, high-AR subset	0.98510	0.98432	0.98350
$R_{K_{xy}}^2$, high-AR subset	0.97437	0.97024	0.96809
<i>F. Physics compliance</i>			
Symmetry error ε_{sym} (mean)	3.95×10^{-7}	7.69×10^{-7}	1.39×10^{-6}
95 % BCa CI	[$3.82, 4.10$] $\times 10^{-7}$	[7.41, 7.99] $\times 10^{-7}$	[1.32, 1.47] $\times 10^{-6}$
Positivity fraction (%)	100.0	100.0	100.0
<i>G. Predictive uncertainty (MC-Dropout, $T = 100$)</i>			
MCE	0.3724	0.3754	0.3786
Global mean $\bar{\sigma}$	8.896×10^{-3}	9.069×10^{-3}	9.755×10^{-3}
$\bar{\sigma}_{K_{xx}}$	1.263×10^{-2}	1.285×10^{-2}	1.400×10^{-2}
$\bar{\sigma}_{K_{xy}}$	5.148×10^{-3}	5.234×10^{-3}	5.476×10^{-3}
$\bar{\sigma}_{K_{yx}}$	5.148×10^{-3}	5.234×10^{-3}	5.476×10^{-3}
$\bar{\sigma}_{K_{yy}}$	1.266×10^{-2}	1.296×10^{-2}	1.407×10^{-2}
UE-corr $\rho_{K_{xx}}$	0.229	0.214	0.196
UE-corr $\rho_{K_{xy}}$	0.304	0.296	0.271
UE-corr $\rho_{K_{yx}}$	0.304	0.296	0.271
UE-corr $\rho_{K_{yy}}$	0.235	0.218	0.204
<i>H. Model specification</i>			
Total parameters (M)	118.97	118.87	118.87
Backbone parameters (M)	118.64	118.64	118.64
Task-specific parameters (M)	0.33	0.23	0.23
Backbone frozen	Yes	No	No
Porosity encoder + FiLM	Yes	No	No
SWA (epochs 400–600)	Yes	No	No

Continued on next page

Table 15 (continued)

Metric	Phase 4	Phase 3	Phase 2
EMA ($\lambda = 0.9999$)	Yes	No	No

Notes. $\Delta R^2 = R_{\text{diag}}^2 - R_{\text{off-diag}}^2$; a smaller gap indicates more balanced accuracy across tensor components. MAPE for off-diagonal components exceeds 100% in quasi-isotropic samples where true values approach zero; RRMSE is the more informative relative metric in this regime. MCE: mean calibration error of MC-Dropout prediction intervals. UE-corr $\rho > 0$ confirms statistically significant error-ranking capability of the uncertainty estimates. FiLM: Feature-wise Linear Modulation; SWA: Stochastic Weight Averaging; EMA: Exponential Moving Average.

[†]MAPE for K_{xy} and K_{yx} is inflated by near-zero true values in quasi-isotropic samples; RRMSE is the appropriate relative metric for these components.

References

- [1] M. J. Blunt. “Flow in porous media—pore-network models and multiphase flow”. In: *Current opinion in colloid & interface science* 6.3 (2001), pp. 197–207 (cit. on p. 1).
- [2] A. J. Ladd and P. Szymczak. “Reactive flows in porous media: Challenges in theoretical and numerical methods”. In: *Annual review of chemical and biomolecular engineering* 12.1 (2021), pp. 543–571 (cit. on p. 1).
- [3] E. R. Okoroafor, S. D. Saltzer, and A. R. Kovscek. “Toward underground hydrogen storage in porous media: Reservoir engineering insights”. In: *International Journal of Hydrogen Energy* 47.79 (2022), pp. 33781–33802 (cit. on p. 1).
- [4] D. B. Ingham, A. Bejan, E. Mamut, and I. Pop. “Emerging technologies and techniques in porous media”. In: (2012) (cit. on p. 1).
- [5] H. Nisbet, G. Buscarnera, J. Carey, M. A. Chen, E. Detournay, H. Huang, J. Hyman, P. Kang, Q. Kang, J. F. Labuz, et al. “Carbon mineralization in fractured mafic and ultramafic rocks: A review”. In: *Reviews of Geophysics* 62.4 (2024), e2023RG000815 (cit. on p. 1).
- [6] M. Nooraiepour, K. M. Dąbrowski, M. Masoudi, S. Kuczyński, Z. Song, A. E. Lothe, and H. Hellevang. “Geological CO₂ storage assessment in emerging CCS regions: Review of sequestration potential, policy development, and socio-economic factors in Poland”. In: *International Journal of Greenhouse Gas Control* 148 (2025), p. 104524 (cit. on p. 1).
- [7] L. M. McDowell-Boyer, J. R. Hunt, and N. Sitar. “Particle transport through porous media”. In: *Water resources research* 22.13 (1986), pp. 1901–1921 (cit. on p. 1).
- [8] P. Meakin and A. M. Tartakovsky. “Modeling and simulation of pore-scale multiphase fluid flow and reactive transport in fractured and porous media”. In: *Reviews of Geophysics* 47.3 (2009) (cit. on p. 2).
- [9] W. Ehlers and A. Wagner. “Modelling and simulation methods applied to coupled problems in porous-media mechanics”. In: *Archive of Applied Mechanics* 89.4 (2019), pp. 609–628 (cit. on p. 2).
- [10] H. Liu, Q. Kang, C. R. Leonardi, S. Schmieschek, A. Narváez, B. D. Jones, J. R. Williams, A. J. Valocchi, and J. Harting. “Multiphase lattice Boltzmann simulations for porous media applications: A review”. In: *Computational Geosciences* 20.4 (2016), pp. 777–805 (cit. on p. 2).
- [11] L. Chen, A. He, J. Zhao, Q. Kang, Z.-Y. Li, J. Carmeliet, N. Shikazono, and W.-Q. Tao. “Pore-scale modeling of complex transport phenomena in porous media”. In: *Progress in Energy and Combustion Science* 88 (2022), p. 100968 (cit. on p. 2).

- [12] P. Moin and K. Mahesh. “Direct numerical simulation: a tool in turbulence research”. In: *Annual review of fluid mechanics* 30.1 (1998), pp. 539–578 (cit. on p. 2).
- [13] B. D. Wood, X. He, and S. V. Apte. “Modeling turbulent flows in porous media”. In: *Annual Review of Fluid Mechanics* 52.1 (2020), pp. 171–203 (cit. on p. 2).
- [14] Y. Da Wang, M. J. Blunt, R. T. Armstrong, and P. Mostaghimi. “Deep learning in pore scale imaging and modeling”. In: *Earth-Science Reviews* 215 (2021), p. 103555 (cit. on p. 2).
- [15] M. Delpisheh, B. Ebrahimpour, A. Fattahi, M. Siavashi, H. Mir, H. Mashhadimoslem, M. A. Abdol, M. Ghorbani, J. Shokri, D. Niblett, et al. “Leveraging machine learning in porous media”. In: *Journal of Materials Chemistry A* (2024) (cit. on p. 2).
- [16] J. Abbasi, A. D. Jagtap, B. Moseley, A. Hiorth, and P. Ø. Andersen. “Challenges and advancements in modeling shock fronts with physics-informed neural networks: A review and benchmarking study”. In: *arXiv preprint arXiv:2503.17379* (2025) (cit. on p. 2).
- [17] R. Peng and X. Yang. “Recent advances in the application of porosity and permeability in porous media”. In: *Physics of Fluids* 37.7 (2025) (cit. on p. 2).
- [18] K. M. Graczyk and M. Matyka. “Predicting porosity, permeability, and tortuosity of porous media from images by deep learning”. In: *Scientific reports* 10.1 (2020), p. 21488 (cit. on p. 2).
- [19] J. Wu, X. Yin, and H. Xiao. “Seeing permeability from images: fast prediction with convolutional neural networks”. In: *Science bulletin* 63.18 (2018), pp. 1215–1222 (cit. on pp. 2, 3).
- [20] X. An, S. Teng, Z. Wang, and Q. Liang. “Implicit neural network-based coal SEM super-resolution for enhancing micro-pores measurement tasks”. In: *Neural Networks* 198 (2026). DOI: [10.1016/j.neunet.2026.108578](https://doi.org/10.1016/j.neunet.2026.108578) (cit. on p. 2).
- [21] N. Alqahtani, R. T. Armstrong, and P. Mostaghimi. “Deep learning convolutional neural networks to predict porous media properties”. In: *SPE Asia Pacific oil and gas conference and exhibition*. SPE. 2018, D012S032R010 (cit. on p. 2).
- [22] T. Yasuda, S. Ookawara, S. Yoshikawa, and H. Matsumoto. “Machine learning and data-driven characterization framework for porous materials: Permeability prediction and channeling defect detection”. In: *Chemical Engineering Journal* 420 (2021), p. 130069 (cit. on pp. 2, 3).
- [23] M. Elmorsy, W. El-Dakhakhni, and B. Zhao. “Generalizable permeability prediction of digital porous media via a novel multi-scale 3D convolutional neural network”. In: *Water Resources Research* 58.3 (2022), e2021WR031454 (cit. on p. 2).
- [24] S. Gärttner, F. O. Alpak, A. Meier, N. Ray, and F. Frank. “Estimating permeability of 3D micro-CT images by physics-informed CNNs based on DNS”. In: *Computational Geosciences* 27.2 (2023), pp. 245–262 (cit. on pp. 2, 3).
- [25] H. Li, B. Aslam, and B. Yan. “An Integrated Deep Learning and Physics-Constrained Upscaling Workflow for Robust Permeability Prediction in Digital Rock Physics”. In: *SPE Journal* (2025), pp. 1–20 (cit. on p. 2).
- [26] A. M. Tartakovsky, C. O. Marrero, P. Perdikaris, G. D. Tartakovsky, and D. Barajas-Solano. “Physics-informed deep neural networks for learning parameters and constitutive relationships in subsurface flow problems”. In: *Water Resources Research* 56.5 (2020), e2019WR026731 (cit. on p. 2).
- [27] A. Kashеfi and T. Mukerji. “Prediction of fluid flow in porous media by sparse observations and physics-informed PointNet”. In: *Neural Networks* 167 (2023), pp. 80–91. DOI: [10.1016/j.neunet.2023.08.006](https://doi.org/10.1016/j.neunet.2023.08.006) (cit. on p. 2).

- [28] M. Elmersy, W. El-Dakhakhni, and B. Zhao. “Rapid permeability upscaling of digital porous media via physics-informed neural networks”. In: *Water Resources Research* 59.12 (2023), e2023WR035064 (cit. on p. 2).
- [29] Y. Zhuang, Q. Ye, N. Liu, X. Xie, H. Yan, and L. Zeng. “Hybrid physics-data-driven deep learning for pore-scale transport in microfluidic system”. In: *Physics of Fluids* 37.7 (2025) (cit. on p. 2).
- [30] Q. Zhao, X. Han, R. Guo, and C. Chen. “A computationally efficient hybrid neural network architecture for porous media: Integrating convolutional and graph neural networks for improved property predictions”. In: *Advances in Water Resources* 195 (2025), p. 104881 (cit. on pp. 2, 30).
- [31] X. Zhao, Y. Zhong, and P. Li. “RTG-GNN: A novel rock topology-guided approach for permeability prediction using graph neural networks”. In: *Geoenergy Science and Engineering* 243 (2024), p. 213358 (cit. on pp. 2, 30).
- [32] M. K. Alzahrani, A. Shapoval, Z. Chen, and S. S. Rahman. “Pore-GNN: A graph neural network-based framework for predicting flow properties of porous media from micro-CT images”. In: *Advances in Geo-Energy Research* 10.1 (2023), pp. 39–55 (cit. on pp. 2, 30).
- [33] S. Cai, Z. Mao, Z. Wang, M. Yin, and G. E. Karniadakis. “Physics-informed neural networks (PINNs) for fluid mechanics: A review”. In: *Acta Mechanica Sinica* 37.12 (2021), pp. 1727–1738 (cit. on p. 2).
- [34] M. Nooraiepour. “Traditional and Machine Learning Approaches to Partial Differential Equations: A Critical Review of Methods, Trade-Offs, and Integration”. In: *Preprints* (Sept. 2025). DOI: [10.20944/preprints202509.0472.v1](https://doi.org/10.20944/preprints202509.0472.v1) (cit. on p. 2).
- [35] P. Liu, L. Wang, R. Ranjan, G. He, and L. Zhao. “A survey on active deep learning: From model driven to data driven”. In: *ACM Computing Surveys (CSUR)* 54.10s (2022), pp. 1–34 (cit. on p. 2).
- [36] C. K. Williams and C. E. Rasmussen. *Gaussian processes for machine learning*. Vol. 2. 3. MIT press Cambridge, MA, 2006 (cit. on p. 2).
- [37] F. Stulp and O. Sigaud. “Many regression algorithms, one unified model: A review”. In: *Neural Networks* 69 (2015). Cited by: 189; All Open Access, Green Open Access, pp. 60–79. DOI: [10.1016/j.neunet.2015.05.005](https://doi.org/10.1016/j.neunet.2015.05.005) (cit. on p. 2).
- [38] E. Schulz, M. Speekenbrink, and A. Krause. “A tutorial on Gaussian process regression: Modelling, exploring, and exploiting functions”. In: *Journal of mathematical psychology* 85 (2018), pp. 1–16 (cit. on p. 2).
- [39] L. Breiman. “Random forests”. In: *Machine learning* 45.1 (2001), pp. 5–32 (cit. on p. 2).
- [40] J. H. Friedman. “Greedy function approximation: a gradient boosting machine”. In: *Annals of statistics* (2001), pp. 1189–1232 (cit. on p. 2).
- [41] M. Fernández-Delgado, M. Sirsat, E. Cernadas, S. Alawadi, S. Barro, and M. Febrero-Bande. “An extensive experimental survey of regression methods”. In: *Neural Networks* 111 (2019). Cited by: 286; All Open Access, Green Open Access, pp. 11–34. DOI: [10.1016/j.neunet.2018.12.010](https://doi.org/10.1016/j.neunet.2018.12.010) (cit. on p. 2).
- [42] T. Chen and C. Guestrin. “Xgboost: A scalable tree boosting system”. In: *Proceedings of the 22nd acm sigkdd international conference on knowledge discovery and data mining*. 2016, pp. 785–794 (cit. on p. 2).
- [43] A. J. Smola and B. Schölkopf. “A tutorial on support vector regression”. In: *Statistics and computing* 14.3 (2004), pp. 199–222 (cit. on p. 2).
- [44] H. Drucker, C. J. Burges, L. Kaufman, A. Smola, and V. Vapnik. “Support vector regression machines”. In: *Advances in neural information processing systems* 9 (1996) (cit. on p. 2).

- [45] G. Huang, G.-B. Huang, S. Song, and K. You. “Trends in extreme learning machines: A review”. In: *Neural Networks* 61 (2015). Cited by: 1686, pp. 32–48. DOI: [10.1016/j.neunet.2014.10.001](https://doi.org/10.1016/j.neunet.2014.10.001) (cit. on p. 2).
- [46] T. Hastie, R. Tibshirani, J. H. Friedman, and J. H. Friedman. *The elements of statistical learning: data mining, inference, and prediction*. Vol. 2. Springer, 2009 (cit. on p. 2).
- [47] T. Bouwmans, S. Javed, M. Sultana, and S. K. Jung. “Deep neural network concepts for background subtraction: A systematic review and comparative evaluation”. In: *Neural Networks* 117 (2019). Cited by: 318; All Open Access, Bronze Open Access, pp. 8–66. DOI: [10.1016/j.neunet.2019.04.024](https://doi.org/10.1016/j.neunet.2019.04.024) (cit. on p. 3).
- [48] C. Tian, L. Fei, W. Zheng, Y. Xu, W. Zuo, and C.-W. Lin. “Deep learning on image denoising: An overview”. In: *Neural Networks* 131 (2020). Cited by: 935, pp. 251–275. DOI: [10.1016/j.neunet.2020.07.025](https://doi.org/10.1016/j.neunet.2020.07.025) (cit. on p. 3).
- [49] M. Buda, A. Maki, and M. A. Mazurowski. “A systematic study of the class imbalance problem in convolutional neural networks”. In: *Neural Networks* 106 (2018). Cited by: 2352; All Open Access, Green Open Access, pp. 249–259. DOI: [10.1016/j.neunet.2018.07.011](https://doi.org/10.1016/j.neunet.2018.07.011) (cit. on p. 3).
- [50] A. Mumuni and F. Mumuni. “CNN architectures for geometric transformation-invariant feature representation in computer vision: a review”. In: *SN Computer Science* 2.5 (2021), p. 340 (cit. on p. 3).
- [51] Y. LeCun, Y. Bengio, and G. Hinton. “Deep learning”. In: *nature* 521.7553 (2015), pp. 436–444 (cit. on p. 3).
- [52] X.-S. Wei, Y.-Z. Song, O. Mac Aodha, J. Wu, Y. Peng, J. Tang, J. Yang, and S. Belongie. “Fine-grained image analysis with deep learning: A survey”. In: *IEEE transactions on pattern analysis and machine intelligence* 44.12 (2021), pp. 8927–8948 (cit. on p. 3).
- [53] H. Yao, S. Zhang, Y. Zhang, J. Li, and Q. Tian. “Coarse-to-fine description for fine-grained visual categorization”. In: *IEEE Transactions on Image Processing* 25.10 (2016), pp. 4858–4872 (cit. on p. 3).
- [54] A. Dosovitskiy. “An image is worth 16x16 words: Transformers for image recognition at scale”. In: *arXiv preprint arXiv:2010.11929* (2020) (cit. on p. 3).
- [55] D. Soydaner. “Attention mechanism in neural networks: where it comes and where it goes”. In: *Neural Computing and Applications* 34.16 (2022), pp. 13371–13385 (cit. on p. 3).
- [56] A. Vaswani, N. Shazeer, N. Parmar, J. Uszkoreit, L. Jones, A. N. Gomez, Ł. Kaiser, and I. Polosukhin. “Attention is all you need”. In: *Advances in neural information processing systems* 30 (2017) (cit. on p. 3).
- [57] J. Yang, C. Li, P. Zhang, X. Dai, B. Xiao, L. Yuan, and J. Gao. “Focal self-attention for local-global interactions in vision transformers”. In: *arXiv preprint arXiv:2107.00641* (2021) (cit. on p. 3).
- [58] A. Khan, Z. Rauf, A. Sohail, A. R. Khan, H. Asif, A. Asif, and U. Farooq. “A survey of the vision transformers and their CNN-transformer based variants”. In: *Artificial Intelligence Review* 56.Suppl 3 (2023), pp. 2917–2970 (cit. on p. 3).
- [59] T. Xiao, M. Singh, E. Mintun, T. Darrell, P. Dollár, and R. Girshick. “Early convolutions help transformers see better”. In: *Advances in neural information processing systems* 34 (2021), pp. 30392–30400 (cit. on p. 3).
- [60] Z. Dai, H. Liu, Q. V. Le, and M. Tan. “Coatnet: Marrying convolution and attention for all data sizes”. In: *Advances in neural information processing systems* 34 (2021), pp. 3965–3977 (cit. on p. 3).

- [61] Z. Liu, Y. Lin, Y. Cao, H. Hu, Y. Wei, Z. Zhang, S. Lin, and B. Guo. “Swin transformer: Hierarchical vision transformer using shifted windows”. In: *Proceedings of the IEEE/CVF international conference on computer vision*. 2021, pp. 10012–10022 (cit. on p. 3).
- [62] X. Dong, J. Bao, D. Chen, W. Zhang, N. Yu, L. Yuan, D. Chen, and B. Guo. “Cswin transformer: A general vision transformer backbone with cross-shaped windows”. In: *Proceedings of the IEEE/CVF conference on computer vision and pattern recognition*. 2022, pp. 12124–12134 (cit. on p. 3).
- [63] H. Long. “Hybrid design of CNN and vision transformer: A review”. In: *Proceedings of the 2024 7th International Conference on Computer Information Science and Artificial Intelligence*. 2024, pp. 121–127 (cit. on p. 3).
- [64] Z. Tu, H. Talebi, H. Zhang, F. Yang, P. Milanfar, A. Bovik, and Y. Li. “Maxvit: Multi-axis vision transformer”. In: *European conference on computer vision*. Springer. 2022, pp. 459–479 (cit. on pp. 3, 4, 7).
- [65] S. Bangalore Vijayakumar, K. T. Chitty-Venkata, K. Arya, and A. K. Somani. “Convission benchmark: A contemporary framework to benchmark cnn and vit models”. In: *AI 5.3* (2024), pp. 1132–1171 (cit. on p. 4).
- [66] V. Hassija, B. Palanisamy, A. Chatterjee, A. Mandal, D. Chakraborty, A. Pandey, G. Chalapathi, and D. Kumar. “Transformers for Vision: A Survey on Innovative Methods for Computer Vision”. In: *IEEE Access* (2025) (cit. on p. 4).
- [67] K. He, X. Chen, S. Xie, Y. Li, P. Dollár, and R. Girshick. “Masked autoencoders are scalable vision learners”. In: *Proceedings of the IEEE/CVF conference on computer vision and pattern recognition*. 2022, pp. 16000–16009 (cit. on p. 4).
- [68] C. Feichtenhofer, Y. Li, K. He, et al. “Masked autoencoders as spatiotemporal learners”. In: *Advances in neural information processing systems* 35 (2022), pp. 35946–35958 (cit. on p. 4).
- [69] C. J. Reed, R. Gupta, S. Li, S. Brockman, C. Funk, B. Clipp, K. Keutzer, S. Candido, M. Uyttendaele, and T. Darrell. “Scale-mae: A scale-aware masked autoencoder for multi-scale geospatial representation learning”. In: *Proceedings of the IEEE/CVF International Conference on Computer Vision*. 2023, pp. 4088–4099 (cit. on p. 4).
- [70] T. Cohen and M. Welling. “Group equivariant convolutional networks”. In: *International conference on machine learning*. PMLR. 2016, pp. 2990–2999 (cit. on pp. 4, 11, 31, 41).
- [71] T. S. Cohen, M. Geiger, J. Köhler, and M. Welling. “Spherical cnns”. In: *arXiv preprint arXiv:1801.10130* (2018) (cit. on pp. 4, 41).
- [72] M. Weiler and G. Cesa. “General e (2)-equivariant steerable cnns”. In: *Advances in neural information processing systems* 32 (2019) (cit. on pp. 4, 11, 31, 41).
- [73] E. Perez, F. Strub, H. De Vries, V. Dumoulin, and A. Courville. “Film: Visual reasoning with a general conditioning layer”. In: *Proceedings of the AAAI conference on artificial intelligence*. Vol. 32. 1. 2018 (cit. on pp. 5, 8).
- [74] P. Izmailov, D. Podoprikin, T. Garipov, D. Vetrov, and A. G. Wilson. “Averaging weights leads to wider optima and better generalization”. In: *arXiv preprint arXiv:1803.05407* (2018) (cit. on pp. 5, 10, 43).
- [75] B. T. Polyak and A. B. Juditsky. “Acceleration of stochastic approximation by averaging”. In: *SIAM journal on control and optimization* 30.4 (1992), pp. 838–855 (cit. on p. 5).
- [76] S. Vargdal, P. Reis, H. A. Sveinsson, and G. Linga. “Neural Networks for Predicting Permeability Tensors of 2D Porous Media: Comparison of Convolution- and Transformer-based Architectures”. In: (2025) (cit. on pp. 5, 6, 29).

- [77] S. Vargdal. *Dataset and Model Weights for: Neural Networks for Predicting Permeability Tensors of 2D Porous Media: Comparison of Convolution- and Transformer- based Architectures*. Zenodo, Nov. 2025. DOI: [10.5281/zenodo.17711512](https://doi.org/10.5281/zenodo.17711512) (cit. on pp. 5, 6, 29, 34).
- [78] R. Wightman. *PyTorch Image Models*. <https://github.com/huggingface/pytorch-image-models>. 2019 (cit. on p. 7).
- [79] R. Wightman, H. Touvron, and H. Jégou. *ResNet strikes back: An improved training procedure in timm*. 2021 (cit. on p. 7).
- [80] D. Morales-Brotons, T. Vogels, and H. Hendriks. “Exponential moving average of weights in deep learning: Dynamics and benefits”. In: *arXiv preprint arXiv:2411.18704* (2024) (cit. on pp. 10, 43).
- [81] J. Bear. *Dynamics of fluids in porous media*. Courier Corporation, 2013 (cit. on p. 11).
- [82] S. Whitaker. *The method of volume averaging*. Vol. 13. Springer Science & Business Media, 2013 (cit. on p. 11).
- [83] H. V. Gupta, H. Kling, K. K. Yilmaz, and G. F. Martinez. “Decomposition of the mean squared error and NSE performance criteria: Implications for improving hydrological modelling”. In: *Journal of hydrology* 377.1-2 (2009), pp. 80–91 (cit. on pp. 16, 44, 49).
- [84] C. J. Willmott. “On the validation of models”. In: *Physical geography* 2.2 (1981), pp. 184–194 (cit. on pp. 16, 44, 49).
- [85] Q. Zhao and H. Xiao. “An End-to-End Differentiable, Graph Neural Network-Embedded Pore Network Model for Permeability Prediction”. In: *arXiv preprint arXiv:2509.13841* (2025) (cit. on p. 30).
- [86] X. Zhao, Y. Zhong, and P. Li. “Porous rock permeability quantification: A superpixel-driven graph neural network method for pore region analysis”. In: *Gondwana Research* (2025) (cit. on p. 30).
- [87] I. Loshchilov and F. Hutter. “Decoupled weight decay regularization”. In: *arXiv preprint arXiv:1711.05101* (2017) (cit. on p. 40).
- [88] B. Efron. “Better bootstrap confidence intervals”. In: *Journal of the American statistical Association* 82.397 (1987), pp. 171–185 (cit. on pp. 44, 46).
- [89] C. Guo, G. Pleiss, Y. Sun, and K. Q. Weinberger. “On calibration of modern neural networks”. In: *International conference on machine learning*. PMLR, 2017, pp. 1321–1330 (cit. on p. 45).